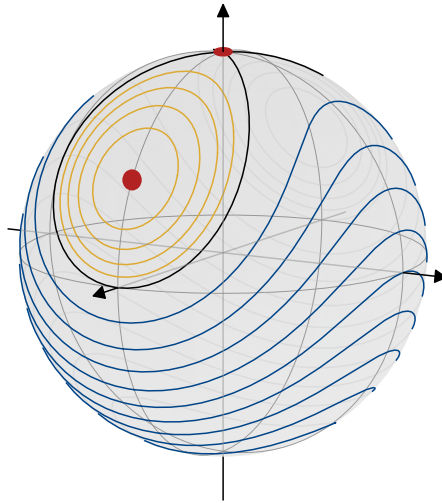


QUANTUM DYNAMICS IN A FERROMAGNETIC ATOMIC GAS



Von der QUEST Leibniz Forschungsschule der
Gottfried Wilhelm Leibniz Universität Hannover
zur Erlangung des Grades

Doktor der Naturwissenschaften
- Dr. rer. nat. -

genehmigte Dissertation von

M. Sc. M. Ed. Bernd Meyer-Hoppe

2023

REFERENT

apl. Prof. Dr. Carsten Klempt
Institut für Quantenoptik
Leibniz Universität Hannover
Deutschland

KORREFERENT

Prof. Dr. Luis Santos
Institut für Theoretische Physik
Leibniz Universität Hannover
Deutschland

KORREFERENT

Assoc. Prof. Dr. Jan Joachim Arlt
Department of Physics and Astronomy
Aarhus Universitet
Dänemark

VORSITZENDE DER PRÜFUNGSKOMMISSION

Prof. Dr. Michèle Heurs
Max-Planck-Institut für Gravitationsphysik
(Albert-Einstein-Institut)
und Institut für Gravitationsphysik
Leibniz Universität Hannover
Deutschland

TAG DER PROMOTION: 13.10.2023

Bernd Meyer-Hoppe:
Quantum Dynamics in a Ferromagnetic Atomic Gas,
PhD Thesis, Leibniz Universität Hannover © 2023

ABSTRACT

Bose-Einstein condensates (BECs) provide an extraordinary system to study many-body quantum effects with a high degree of control. Using such ultra-cold gases, microscopic quantum effects become visible on a macroscopic scale as thermal fluctuations are negligible. In particular, quantum phase transitions can be observed. These phase transitions can be indicated by an order parameter that abruptly changes at the critical value of a certain control parameter.

Throughout this work, a spin-1 BEC with ferromagnetic interactions and zero magnetization is considered. This system exhibits three ground-state quantum phases that can be controlled by an effective magnetic field. These phases have been explored both theoretically and experimentally in the last two decades.

Quantum phase transitions are by definition only applicable to the ground state of a system. However, this powerful concept can be extended to states with non-zero energy. Such excited-state quantum phase transitions (ESQPTs) can be driven by a conventional control parameter, but, interestingly, also by a variation of the excitation energy only. ESQPTs have been studied theoretically and their existence itself has been revealed, e.g., in molecular spectra. However, a thorough investigation by an order parameter and in particular the experimental mapping of the corresponding phase diagram remain an open challenge in any physical system.

In this thesis, an interferometric order parameter is employed to experimentally map out an excited-state quantum phase diagram. This order parameter is based on dynamical behavior of coherent states that resemble the mean-field phase-space trajectories of excited-state phases. While a ferromagnetic spin-1 BEC with zero magnetization serves as an exemplary platform, the findings can be applied to other quantum systems with similar Hamiltonians. Importantly, the distinction of excited-state quantum phases utilizes the excitation energy as a second control parameter, which presents a key feature of ESQPTs. Our experiments therefore extend the powerful concept of quantum phases and quantum phase transitions to the entire Hilbert space of the spin-1 BEC.

KEYWORDS: spinor Bose-Einstein condensate, spin-changing collisions, ferromagnetic interaction, phase diagrams, quantum phase transitions, excited-state quantum phase transitions

CONTENTS

1	INTRODUCTION	1
2	SPINOR BOSE-EINSTEIN CONDENSATES	5
2.1	Atomic spin-1 system	5
2.1.1	Construction of a Hamiltonian	5
2.1.2	Single-mode approximation	7
2.1.3	Spin interaction	10
2.2	Internal degrees of freedom	12
2.2.1	Collective spins	12
2.2.2	Energy level structure	15
2.2.3	Coupling to electromagnetic radiation	17
3	QUANTUM PHASES IN SPINOR BOSE-EINSTEIN CONDENSATES	23
3.1	Mean-field limit	23
3.2	Ground-state quantum phases	24
3.3	Excited-state quantum phases	29
3.3.1	Phase diagram	29
3.3.2	Dynamics of excited coherent states	31
3.3.3	Interferometric order parameter	34
4	EXPERIMENTAL PLATFORM	37
4.1	BEC generation procedure	37
4.2	Magnetic field fluctuations	41
4.3	Microwave and radio frequency coupling	43
4.4	Calibration of the quadratic Zeeman energy	45
4.5	Spin dynamics rate	49
5	VERSATILE AND LOW-NOISE INTERNAL STATE MANIPULATION	53
5.1	Overview of the experimental setup	53
5.2	Microwave synthesis chain	55
5.3	State-selective radio frequency transfer	60
5.4	Techniques for noise-robust pulses	63
5.4.1	Pulse shaping	63
5.4.2	Composite pulses	64
5.5	Discussion	66
6	AN EXCITED-STATE QUANTUM PHASE DIAGRAM	69
6.1	Preparation of excited-states	69
6.2	Population oscillations	70
6.3	Phase signal	73
6.4	Distinguishing excited-state quantum phases	75
6.4.1	Iterative measurement	75
6.4.2	Signal in the fluctuations	77
6.4.3	Separation of the symmetric contribution	79
6.5	Discussion	86

CONTENTS

7	OUTLOOK	89
7.1	Quantum dynamics utilized for metrology	90
7.2	Spatial excited-state quantum phase transitions	93
A	APPENDIX	97
A.1	Calculation of the eigenenergies	97
A.2	Derivation of the fluctuation boundaries	98
A.3	Signal in the fluctuations for a variation of $q/ \Omega $	99
	BIBLIOGRAPHY	101

LIST OF FIGURES

Figure 2.1	Energy scaling in a single-mode Bose-Einstein condensate	8
Figure 2.2	Spin-changing collisions create entanglement	11
Figure 2.3	Generalized Bloch sphere	14
Figure 2.4	Graphical representation of spin states	15
Figure 2.5	Level structure of the electronic ground state of ^{87}Rb	16
Figure 2.6	Relevant coupling of internal states	18
Figure 3.1	Ground-state energy and its derivatives	25
Figure 3.2	Energy gap between ground and first excited state . .	26
Figure 3.3	Order parameter for ground-state quantum phase transitions	27
Figure 3.4	Phase diagram of a ferromagnetic spinor Bose-Einstein condensate	28
Figure 3.5	Concept of excited-state quantum phase transitions .	30
Figure 3.6	Expected quantum phases depending on experimental control parameters	31
Figure 3.7	Energy hypersurfaces on Bloch spheres	32
Figure 3.8	Bloch sphere, phase-space diagram and time evolution	33
Figure 3.9	Schematic depiction of the interferometric order parameter	34
Figure 4.1	Experimental sequence for generation of Bose-Einstein condensates	37
Figure 4.2	Experimental apparatus	38
Figure 4.3	Schematic of a magneto-optical trap and radio frequency evaporation	39
Figure 4.4	Typical absorption detection image	40
Figure 4.5	Determination of magnetic-field compensation currents	42
Figure 4.6	Magnetic field measurement by a Ramsey sequence .	43
Figure 4.7	Radio frequency calibration	44
Figure 4.8	Microwave phase imprint	45
Figure 4.9	Energy shift due to microwave dressing	46
Figure 4.10	Calibration of the quadratic Zeeman energy	47
Figure 4.11	Fluctuations of the spin dynamics resonance frequency	48
Figure 4.12	Determination of the spin dynamics rate $ \Omega $	50
Figure 4.13	Tuning the spin dynamics rate by atom number and trapping frequencies	51
Figure 5.1	Sketch of the microwave and radio frequency generation	54
Figure 5.2	Phase noise of clocking methods and Wenzel oscillator multiplications	55
Figure 5.3	Setup for microwave frequency synthesis	57
Figure 5.4	Nonlinearity in the output power	58

LIST OF FIGURES

Figure 5.5	Spectrum of the microwave signal at 6.835 GHz for dressing and pulse path	59
Figure 5.6	Phase and amplitude noise of the microwave source	60
Figure 5.7	Schematic of state-selective radio frequency transfer	61
Figure 5.8	State-selective radio frequency transfer	62
Figure 5.9	Pulse shaping of amplitude and phase	64
Figure 5.10	Composite pulse sequences	66
Figure 6.1	Preparation of excited states	70
Figure 6.2	Population oscillations	71
Figure 6.3	Determination of half periods for a variation of $q/ \Omega $	72
Figure 6.4	Phase signal	74
Figure 6.5	Iterative procedure to measure a phase evolution	75
Figure 6.6	Extracting the order parameter by iterative measurements	76
Figure 6.7	Signal of a phase transition in the fluctuations	78
Figure 6.8	Scheme for a measurement of the interferometric order parameter with reduced fluctuations	80
Figure 6.9	Calibration of radio frequency transfer in $F = 2$	81
Figure 6.10	Measurement of the interferometric order parameter with reduced fluctuations	82
Figure 6.11	Order parameter measurement for a variation of the quadratic Zeeman energy	83
Figure 6.12	Order parameter measurement for a variation of the excitation energy	84
Figure 6.13	Conclusive excited-state quantum phase diagram	85
Figure 6.14	Sequence to extract the order parameter using state-selective radio frequency transfer	87
Figure 7.1	Generation of squeezed states	91
Figure 7.2	Tomography of a spin-squeezed state	92
Figure 7.3	Excited-state quantum phase transitions with spatial dependence	94
Figure A.1	Signal of a phase transition in the fluctuations for a variation of $q/ \Omega $	99

LIST OF ABBREVIATIONS

BA	broken-axisymmetry
BEC	Bose-Einstein condensate
DDS	direct digital synthesis
ESQPT	excited-state quantum phase transition
FPGA	field-programmable gate array
MOT	magneto-optical trap
mw	microwave
ODT	optical dipole trap
P	polar
QZE	quadratic Zeeman energy
RAM	random-access memory
rf	radio frequency
TF	twin-Fock

INTRODUCTION

A Bose-Einstein condensate (BEC) is a unique state of matter that was predicted by Albert Einstein [1, 2], following pioneering work from Satyendra Nath Bose [3]. It is produced by cooling down bosonic particles of very low density to ultra-low temperatures where the associated de-Broglie wavelength is comparable with the interparticle spacing. At a certain critical temperature that depends on the density of the cloud, the atoms collectively undergo a phase transition and can now be described by a single wave function of a macroscopic quantum state. Such a condensate was experimentally demonstrated in 1995 by the group of Eric Cornell and Carl Wiemann using ^{87}Rb atoms [4] and shortly thereafter by Wolfgang Ketterle's group with ^{23}Na [5]. Those three investigators were rewarded the 2001 Nobel Prize in Physics in return. The first BECs have been created employing magnetic forces that trap atoms with a single, low-field-seeking spin state such that the spin degree of freedom was frozen. In 1998, so-called spinor BECs were demonstrated that are trapped in optical dipole traps [6] and therefore retain an addressable spin [7, 8]. Nowadays, the field of ultracold quantum gases is well established and in the meantime, BECs have also been realized with several other atomic species [9–22] and even molecules [23–25].

A BEC is formed at temperatures close to absolute zero where thermal fluctuations cease. Due to the significant occupation of a common spatial mode, macroscopic interference effects can become observable. For instance, the coherent wave character of BECs has led to the detection of interference between two ultracold clouds [26] and the construction of an atom laser [27].

Microscopic quantum effects become visible macroscopically by the emergence of quantum phase transitions. At zero temperature, classical (or thermal) phase transitions do not exist because the responsible thermal fluctuations vanish. Quantum phase transitions, however, can also occur at zero temperature because they are driven by quantum fluctuations. When the energy scales of quantum effects become relevant at ultra-low temperatures, features like the famous transition from a superfluid to a Mott insulator can be observed [28]. This transition can be identified by a vanishing energy gap in the spectrum.

Ultra-cold quantum systems can nowadays be well isolated from the environment. This enables the preparation at non-zero energy without direct thermalization and therefore the observation of respective dynamics for long evolution times. In the last few years, different phase transitions related to dynamical systems have been explored. One example are dynamical quantum phase transitions that can be identified by a sudden change of dynamical properties like long-term averages at a critical value [29–31] or a nonanalytical behavior of an experimental parameter in time [32, 33]. Another example

is the transition to a time crystal, signaled by a broken time-translational symmetry, i.e., a change in oscillatory behavior of a system [34, 35].

Those presented systems are of dynamical nature. However, phase transitions can also be studied for stable and energetically excited eigenstates. This can be understood as an extension of quantum phase transitions, which are only applicable to ground states. For such excited-state quantum phase transitions (ESQPTs), changes in energy gaps do not only affect the ground and a few low-energy excited-states, but the whole energy spectrum [36]. In this way, the energy serves as an additional control parameter in a novel phase diagram. The existence of ESQPTs has been particularly revealed in bending spectra of molecules [37–41]. For the case of BECs, distinct regimes have been observed in experiments on external [42] and internal [43] Josephson oscillations and they are expected in spin-1 systems [44–46]. Those different dynamical regimes can be connected to ESQPTs [47]. Moreover, proposals are presented for different systems to distinguish excited-state phases by respective order parameters [47–51].

A thorough experimental investigation of ESQPTs and particularly a mapping of a quantum phase diagram, however, is still an open experimental challenge that this thesis aims to meet. In this work, a spin-1 BEC with ferromagnetic interactions and zero magnetization is utilized to distinguish different excited-state quantum phases. This is done by an interferometric order parameter that is based on dynamical behavior of coherent states. The dynamics directly reflects the mean-field phase-space trajectories of excited-state phases. In this way, the experimental mapping of an excited-state quantum phase diagram is finally achieved. Notably, the excitation energy is also employed as an additional control parameter to drive phase transitions, which is an important feature of ESQPTs. The findings can be applied to other quantum systems with similar Hamiltonians and they extend the powerful concept of quantum phases and quantum phase transitions to the entire Hilbert space of the spin-1 BEC.

This thesis is organized as follows:

- Chapter 2 presents the basic theoretical concepts of BECs with a spin degree of freedom. The Hamiltonian of the experimental quantum system is motivated and subsequently reduced to a simple Hamiltonian describing spin dynamics of internal states. Moreover, the relevant internal degrees of freedom and their coupling to electromagnetic radiation are introduced.
- Quantum phases of spin-1 BECs are described from a theoretical point of view in Chapter 3. The focus of this chapter is on quantum phases and dynamics of excited states.
- In Chapter 4, the experimental apparatus is presented. In addition to a general description, some components and techniques are discussed in more detail.
- Experimental results on a recently implemented microwave (mw) and radio frequency (rf) system are presented in Chapter 5. This includes the characterization of a low-noise mw synthesis chain, state-selective rf transfer and advanced techniques for internal state manipulation.
- Chapter 6 presents the main results on excited-state quantum phases. It first describes the preparation of distinct excited states in our atomic system and experiments concerning oscillations of the population distribution. Because the phase signal is affected by magnetic field fluctuations, three methods are presented to nevertheless observe quantum phase transitions of excited states and map a corresponding phase diagram.
- The outlook in Chapter 7 briefly describes further research ideas concerning quantum metrology and ESQPTs in spatially extended atomic clouds.

The system under study in this thesis is a ^{87}Rb BEC. For this state of matter, an ensemble of atoms is prepared in the ground state close to absolute zero temperature. We ensure that the spin of the atoms is a degree of freedom by trapping the ultra-cold gas in an optical dipole trap. In this configuration, we can experimentally address the spins by electromagnetic radiation. This chapter theoretically describes such weakly interacting spin-1 atoms and the intrinsic spin interactions in the atomic cloud. Collective spins and their visualization on a generalized Bloch sphere are introduced as a helpful representation of spin states. Finally, the resulting internal structure of ^{87}Rb BECs and its interaction with electromagnetic signals are presented.

2.1 ATOMIC SPIN-1 SYSTEM

2.1.1 Construction of a Hamiltonian

In the electronic ground state $5^2S_{1/2}$ with hyperfine spin $F = 1$, the atoms can occupy three different states labelled $|F, m\rangle$ with the magnetic quantum number $m \in \{-1, 0, 1\}$. Atoms in the $F = 1$ hyperfine manifold thus constitute a system of spin-1 bosons. Whenever F is not explicitly mentioned, a state $|m\rangle$ denotes $|F = 1, m\rangle$. In the following, the Hamiltonian describing this system is constructed step by step, following Law, Pu, and Bigelow [52], Pu et al. [53] and especially Kawaguchi and Ueda [46].

A system of spin-1 bosons with mass M can be described by field operators $\hat{\psi}_m^{(\dagger)}(\vec{r})$ that annihilate (create) a particle in mode m at position \vec{r} . Those operators obey canonical commutation relations,

$$\begin{aligned} [\hat{\psi}_m(\vec{r}), \hat{\psi}_{m'}^\dagger(\vec{r}')] &= \delta_{mm'} \delta(\vec{r} - \vec{r}'), \\ [\hat{\psi}_m(\vec{r}), \hat{\psi}_{m'}(\vec{r}')] &= [\hat{\psi}_m^\dagger(\vec{r}), \hat{\psi}_{m'}^\dagger(\vec{r}')] = 0, \end{aligned} \quad (2.1)$$

where the first δ represents a Kronecker delta and the second one a Dirac delta distribution.

The external (or non-interacting) contribution to the Hamiltonian \hat{H}_{ext} is given by the kinetic energy and the dipole trap potential $V_{\text{dip}}(\vec{r})$,

$$\hat{H}_{\text{ext}} = \int d^3r \sum_m \hat{\psi}_m^\dagger(\vec{r}) \left(-\frac{\hbar^2 \nabla^2}{2M} + V_{\text{dip}}(\vec{r}) \right) \hat{\psi}_m(\vec{r}). \quad (2.2)$$

An additional, non-interacting term is contributed by the magnetic field that lifts the degeneracy of the Zeeman states with different magnetic quantum number m ,

$$\hat{H}_B = \int d^3r \sum_m \hat{\psi}_m^\dagger(\vec{r}) (-pm + qm^2) \hat{\psi}_m(\vec{r}), \quad (2.3)$$

with p and q corresponding to the (effective) linear and quadratic Zeeman shifts, respectively. Those shifts depend on the magnetic field B by $p_B \approx -h \cdot 700 \text{ kHz/G} \cdot B$ and $q_B \approx h \cdot 72 \text{ Hz/G}^2 \cdot B^2$ (Section 2.2.2), but can also be tuned by mw dressing (Section 2.2.3).

In a next step, we include short-range interactions between the particles. A typical particle density of a Bose-Einstein condensed atomic cloud is on the order of $10^{14}/\text{cm}^3$ [4]. Compared to air at room temperature ($10^{19}/\text{cm}^3$), such a gas can be considered dilute and it is possible to assume that the interactions among particles are binary. Moreover, in the case of ultra-cold atomic clouds associated energies are low. In this low-energy regime, only s-wave scattering happens due to the centrifugal barrier [54]. The two colliding particles form a total spin \mathcal{F} that is conserved in the collision. Because the many-body wave function is symmetric under particle exchange for bosons and the contribution of the orbital angular momentum is symmetric for s-wave scattering, only symmetric states with $\mathcal{F} \in \{0, 2\}$ are possible.

An interaction Hamiltonian [55, 56], can be constructed individually for each collision channel by irreducible operators $\hat{A}_{\mathcal{F}, \mathcal{M}}^{(\dagger)}(\vec{r})$ that express the annihilation (creation) of a pair of atoms with total spin \mathcal{F} and projection \mathcal{M} . It is sufficient to look at a single position \vec{r} only, because the interaction is very short range. From now on, we will omit the explicit position \vec{r} thus for readability. The individual terms of the interaction Hamiltonian $\hat{H}_{\text{int}} = \hat{H}_{\mathcal{F}=0} + \hat{H}_{\mathcal{F}=2}$ then yield

$$\begin{aligned} \hat{H}_{\mathcal{F}=0} &= \frac{g_0}{2} \int d^3r \hat{A}_{00}^\dagger \hat{A}_{00} \\ &= \frac{g_0}{6} \int d^3r \left(\hat{\psi}_0^\dagger \hat{\psi}_0^\dagger \hat{\psi}_0 \hat{\psi}_0 - 2 \hat{\psi}_0^\dagger \hat{\psi}_0^\dagger \hat{\psi}_{-1} \hat{\psi}_1 \right. \\ &\quad \left. - 2 \hat{\psi}_{-1}^\dagger \hat{\psi}_1^\dagger \hat{\psi}_0 \hat{\psi}_0 + 4 \hat{\psi}_{-1}^\dagger \hat{\psi}_1^\dagger \hat{\psi}_{-1} \hat{\psi}_1 \right) \end{aligned} \quad (2.4)$$

and

$$\begin{aligned} \hat{H}_{\mathcal{F}=2} &= \frac{g_2}{2} \int d^3r \sum_{\mathcal{M}=-2}^2 \hat{A}_{2\mathcal{M}}^\dagger \hat{A}_{2\mathcal{M}} \\ &= \frac{g_2}{2} \int d^3r \left(6 \hat{\psi}_0^\dagger \hat{\psi}_0^\dagger \hat{\psi}_0 \hat{\psi}_0 + 2 \hat{\psi}_0^\dagger \hat{\psi}_0^\dagger \hat{\psi}_1 \hat{\psi}_{-1} \right. \\ &\quad + 2 \hat{\psi}_1^\dagger \hat{\psi}_{-1}^\dagger \hat{\psi}_0 \hat{\psi}_0 + 10 \hat{\psi}_1^\dagger \hat{\psi}_{-1}^\dagger \hat{\psi}_1 \hat{\psi}_{-1} \\ &\quad + 14 \hat{\psi}_0^\dagger \hat{\psi}_1^\dagger \hat{\psi}_0 \hat{\psi}_1 + 14 \hat{\psi}_0^\dagger \hat{\psi}_{-1}^\dagger \hat{\psi}_0 \hat{\psi}_{-1} \\ &\quad \left. + 7 \hat{\psi}_1^\dagger \hat{\psi}_1^\dagger \hat{\psi}_1 \hat{\psi}_1 + 7 \hat{\psi}_{-1}^\dagger \hat{\psi}_{-1}^\dagger \hat{\psi}_{-1} \hat{\psi}_{-1} \right). \end{aligned} \quad (2.5)$$

The $g_{\mathcal{F}}$ denote coupling constants,

$$g_{\mathcal{F}} = \frac{4\pi\hbar^2}{M} a_{\mathcal{F}}, \quad (2.6)$$

with respective scattering lengths $a_{\mathcal{F}}$, e.g. for ^{87}Rb [57]

$$a_0 = 101.8(2) a_{\text{B}}, \quad a_2 = 100.4(1) a_{\text{B}}, \quad (2.7)$$

where a_B is the Bohr radius. Combining the two interaction terms and regrouping them, one obtains

$$\begin{aligned} \hat{H}_{\text{int}} = & \frac{c_0}{2} \int d^3r \sum_{m,n} \hat{\psi}_m^\dagger \hat{\psi}_n^\dagger \hat{\psi}_m \hat{\psi}_n \\ & + \frac{c_1}{2} \int d^3r \left(\hat{\psi}_1^\dagger \hat{\psi}_1^\dagger \hat{\psi}_1 \hat{\psi}_1 + \hat{\psi}_{-1}^\dagger \hat{\psi}_{-1}^\dagger \hat{\psi}_{-1} \hat{\psi}_{-1} + 2 \hat{\psi}_1^\dagger \hat{\psi}_0^\dagger \hat{\psi}_1 \hat{\psi}_0 \right. \\ & \quad + 2 \hat{\psi}_{-1}^\dagger \hat{\psi}_0^\dagger \hat{\psi}_{-1} \hat{\psi}_0 - 2 \hat{\psi}_1^\dagger \hat{\psi}_{-1}^\dagger \hat{\psi}_1 \hat{\psi}_{-1} \\ & \quad \left. + 2 \hat{\psi}_0^\dagger \hat{\psi}_0^\dagger \hat{\psi}_1 \hat{\psi}_{-1} + 2 \hat{\psi}_1^\dagger \hat{\psi}_{-1}^\dagger \hat{\psi}_0 \hat{\psi}_0 \right) \end{aligned} \quad (2.8)$$

with interaction coefficients

$$c_0 = \frac{1}{3} (g_0 + 2g_2), \quad c_1 = \frac{1}{3} (g_2 - g_0). \quad (2.9)$$

The term proportional to c_0 is a density-dependent (or spin-independent) interaction term

$$\hat{H}_{\text{density}} = \frac{c_0}{2} \int d^3r \sum_{m,n} \hat{\psi}_m^\dagger \hat{\psi}_n^\dagger \hat{\psi}_m \hat{\psi}_n, \quad (2.10)$$

as it presents the normal-ordered square of the total density

$$\hat{n}(\vec{r}) = \sum_{m=-1}^1 \hat{\psi}_m^\dagger \hat{\psi}_m. \quad (2.11)$$

The second term in \hat{H}_{int} scaling with c_1 is considered to be the spin-dependent interaction term

$$\begin{aligned} \hat{H}_{\text{spin}} = & \frac{c_1}{2} \int d^3r \left(\hat{\psi}_1^\dagger \hat{\psi}_1^\dagger \hat{\psi}_1 \hat{\psi}_1 + \hat{\psi}_{-1}^\dagger \hat{\psi}_{-1}^\dagger \hat{\psi}_{-1} \hat{\psi}_{-1} \right. \\ & \quad + 2 \hat{\psi}_1^\dagger \hat{\psi}_0^\dagger \hat{\psi}_1 \hat{\psi}_0 + 2 \hat{\psi}_{-1}^\dagger \hat{\psi}_0^\dagger \hat{\psi}_{-1} \hat{\psi}_0 - 2 \hat{\psi}_1^\dagger \hat{\psi}_{-1}^\dagger \hat{\psi}_1 \hat{\psi}_{-1} \\ & \quad \left. + 2 \hat{\psi}_0^\dagger \hat{\psi}_0^\dagger \hat{\psi}_1 \hat{\psi}_{-1} + 2 \hat{\psi}_1^\dagger \hat{\psi}_{-1}^\dagger \hat{\psi}_0 \hat{\psi}_0 \right). \end{aligned} \quad (2.12)$$

The total Hamiltonian is finally given by

$$\hat{H} = \hat{H}_{\text{ext}} + \hat{H}_B + \hat{H}_{\text{density}} + \hat{H}_{\text{spin}}. \quad (2.13)$$

2.1.2 Single-mode approximation

We now simplify the Hamiltonian \hat{H} by looking at the scaling of the different contributions to the Hamiltonian and in this way justify the single-mode approximation. This approximation states that a common spatial mode can be assumed for all spin components. For the determination of the spatial wave function $\psi(\vec{r})$, the spin-dependent part of the Hamiltonian can be neglected because its energy contribution is comparably small. Note that, if forced, excitations of higher spatial modes can occur, e.g. by mw dressing that induces spin-changing collisions to generate spatially separated entanglement [58]. In this work, however, such processes are not intended and excluded from the treatment.

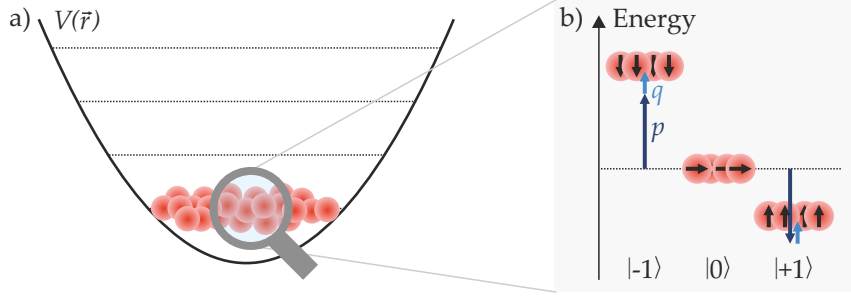


Figure 2.1: Energy scaling in a single-mode BEC. (a) The BEC is in the spatial ground state of the dipole trap potential and all spin components share the same spatial mode. (b) Spin excitations are small in comparison and lead to a state-dependent energy shift due to the linear (p , dark blue) and quadratic (q , light blue) Zeeman effect.

When the spatial wave function is independent of the spin, the field operators can be decomposed into a spatial and a spin part,

$$\hat{\psi}_m^{(+)}(\vec{r}) = \psi^{(*)}(\vec{r}) \hat{a}_m^{(+)}, \quad (2.14)$$

with the common spatial wave function $\psi(\vec{r})$ for all spin components and the bosonic annihilation (creation) operators $\hat{a}^{(+)}$ that fulfill the standard commutation relations

$$\begin{aligned} [\hat{a}_m, \hat{a}_{m'}^\dagger] &= \delta_{mm'}, \\ [\hat{a}_m, \hat{a}_{m'}] &= [\hat{a}_m^\dagger, \hat{a}_{m'}^\dagger] = 0. \end{aligned} \quad (2.15)$$

To justify the single-mode approximation, the spin-dependent terms \hat{H}_B and \hat{H}_{spin} have to be small compared to \hat{H}_{ext} and \hat{H}_{density} . For the $F = 1$ hyperfine manifold in ^{87}Rb , the interaction coefficients (Equation 2.9) are very different, $|c_0| \approx 216 |c_1|$, so the spin-dependent term \hat{H}_{spin} contributes negligible to the interaction energy. This term is furthermore small compared to the kinetic energy in \hat{H}_{ext} for sufficiently weak traps [53] and the magnetic-field contribution \hat{H}_B is insignificant for low magnetic fields on the order of 1 Gauss. Due to this very different energy scaling, spatial modes and spin modes do not thermalize. Cooling down a BEC therefore only prepares the spatial ground state while the spin modes are freely accessible in a common spatial, spin-independent wave function $\psi(\vec{r})$ (Figure 2.1).

Yi et al. [59] supports the validity of the single-mode approximation for the ^{87}Rb spin-1 system (although in the absence of magnetic fields), as the interaction coefficient of the spatial component is much larger than the interaction of the spin-dependent component and therefore the spin part can be treated as a perturbation to the common spatial wave function. However, this assumption should be treated with caution because there exist cases where it is not valid any more, e.g., for certain trapping configurations, where the spin-dependent c_1 term becomes relevant compared to the spatial excitations [53]. In particular, the single-mode approximation could in principle break down for the treatment of excited states that we will investigate in this

work. Calculations for our experimental parameters have, however, shown that the approximation is to a large extent acceptable in our case [60].

The single-mode approximation can thus be applied and we can rewrite the Hamiltonians using Equation 2.14 and $\int d^3r |\psi(\vec{r})|^2 = 1$ as

$$\hat{H}_{\text{ext}} = \int d^3r \psi^*(\vec{r}) \left(-\frac{\hbar^2 \nabla^2}{2M} + V_{\text{dip}}(\vec{r}) \right) \psi(\vec{r}) \hat{N}, \quad (2.16)$$

$$\hat{H}_B = \sum_m (-p m + q m^2) \hat{N}_m, \quad (2.17)$$

$$\hat{H}_{\text{density}} = \frac{c_0}{2} \int d^3r |\psi(\vec{r})|^4 (\hat{N} - 1) \hat{N}, \quad (2.18)$$

$$\begin{aligned} \hat{H}_{\text{spin}} = \frac{\lambda}{2} & \left(\hat{a}_1^\dagger \hat{a}_1^\dagger \hat{a}_1 \hat{a}_1 + \hat{a}_{-1}^\dagger \hat{a}_{-1}^\dagger \hat{a}_{-1} \hat{a}_{-1} + 2 \hat{a}_1^\dagger \hat{a}_0^\dagger \hat{a}_1 \hat{a}_0 \right. \\ & + 2 \hat{a}_{-1}^\dagger \hat{a}_0^\dagger \hat{a}_{-1} \hat{a}_0 - 2 \hat{a}_1^\dagger \hat{a}_{-1}^\dagger \hat{a}_1 \hat{a}_{-1} \\ & \left. + 2 \hat{a}_0^\dagger \hat{a}_0^\dagger \hat{a}_1 \hat{a}_{-1} + 2 \hat{a}_1^\dagger \hat{a}_{-1}^\dagger \hat{a}_0 \hat{a}_0 \right), \end{aligned} \quad (2.19)$$

where $\hat{N}_m = \hat{a}_m^\dagger \hat{a}_m$ gives the number of atoms in spin state m and therefore $\hat{N} = \sum_m \hat{N}_m$ corresponds to the total atom number. The coefficient c_1 has been absorbed in the interaction parameter

$$\lambda = c_1 \int d^3r |\psi(\vec{r})|^4. \quad (2.20)$$

The external and the density-dependent components do not contribute to dynamics as the atom number \hat{N} is in general fixed and therefore it is sufficient to work with the eigenvalue N . Moreover, the associated atom numbers are large, such that $N - 1 \approx N$. The resulting spatial Hamiltonian

$$\begin{aligned} \hat{H}_{\text{spatial}} &= \hat{H}_{\text{ext}} + \hat{H}_{\text{density}} \\ &= \int d^3r \psi^*(\vec{r}) \left(-\frac{\hbar^2 \nabla^2}{2M} + V_{\text{dip}}(\vec{r}) + \frac{c_0}{2} |\psi(\vec{r})|^2 N \right) \psi(\vec{r}) N, \end{aligned} \quad (2.21)$$

resembles the time-independent scalar Gross-Pitaevskii equation [61–63],

$$\left(-\frac{\hbar^2 \nabla^2}{2M} + V_{\text{dip}}(\vec{r}) + \frac{c_0}{2} |\psi(\vec{r})|^2 N \right) \psi(\vec{r}) = \mu \psi(\vec{r}), \quad (2.22)$$

with the chemical potential μ . The ground-state solution of this equation is the spatial wave function $\psi(\vec{r})$ of our condensate. For large interaction energy, i.e., negligible kinetic energy, we achieve the Thomas-Fermi limit that yields the famous inverted parabola form and the Thomas-Fermi radius for a BEC in a spherical harmonic trap.

The spin dynamics of the states is governed by the interplay of magnetic-field contribution and spin Hamiltonian [64],

$$\begin{aligned}\hat{H}_{\text{SD}} &= \hat{H}_B + \hat{H}_{\text{spin}} \\ &= -p\hat{D} + q(\hat{N}_1 + \hat{N}_{-1}) \\ &\quad + \lambda \left[\hat{a}_0^\dagger \hat{a}_0^\dagger \hat{a}_1 \hat{a}_{-1} + \hat{a}_1^\dagger \hat{a}_{-1}^\dagger \hat{a}_0 \hat{a}_0 + \left(\hat{N}_0 - \frac{1}{2} \right) (\hat{N}_1 + \hat{N}_{-1}) + \frac{\hat{D}^2}{2} \right]\end{aligned}\quad (2.23)$$

with the magnetization $\hat{D} = \hat{N}_1 - \hat{N}_{-1}$. This magnetization is conserved during the evolution and therefore the linear Zeeman shift $p\hat{D}$ contributes only trivially. This term can therefore be absorbed in a rotating frame [47]. Moreover, we experimentally prepare zero-magnetization eigenstates, so that we can neglect all terms in \hat{D} and work in the magnetization-free subspace. Note that it would be experimentally feasible to introduce a finite magnetization. However, it seems that excited-state phase transitions are more exposed at zero magnetization [45]. Moreover, it is of course experimentally and computationally easier to work in the magnetization-free subspace.

Finally, we introduce the interaction strength

$$\Omega = \lambda N \quad (2.24)$$

that is occasionally called spin dynamics rate. The resulting Hamiltonian

$$\begin{aligned}\hat{H}_{\text{SD}} &= q(\hat{N}_1 + \hat{N}_{-1}) \\ &\quad + \frac{\Omega}{N} \left[\hat{a}_0^\dagger \hat{a}_0^\dagger \hat{a}_1 \hat{a}_{-1} + \hat{a}_1^\dagger \hat{a}_{-1}^\dagger \hat{a}_0 \hat{a}_0 + \left(\hat{N}_0 - \frac{1}{2} \right) (\hat{N}_1 + \hat{N}_{-1}) \right]\end{aligned}\quad (2.25)$$

presents the spin dynamics that we now want to investigate a little further.

2.1.3 Spin interaction

The remaining terms of Hamiltonian 2.25 include a term proportional to $(\hat{a}_0^\dagger \hat{a}_0^\dagger \hat{a}_1 \hat{a}_{-1} + \hat{a}_1^\dagger \hat{a}_{-1}^\dagger \hat{a}_0 \hat{a}_0)$ that we refer to as spin-changing collisions. In this process, the combined spin during a collision is conserved by a spin change of both constituents, either by two atoms with $m = 0$ changing to $m = +1$ and $m = -1$ or vice versa (Figure 2.2). Because this happens only in pairs, entanglement is introduced in the system [64, 65], presenting an atomic analog of parametric down-conversion to create entangled photons [66]. We will now look at this dynamics, which scales with the spin dynamics rate Ω and is adjusted by q .

For the $F = 1$ manifold in ^{87}Rb , the coupling constant g_0 for interactions with $\mathcal{F} = 0$ is larger than g_2 for $\mathcal{F} = 2$ (Equations 2.6 and 2.7), resulting in $(g_2 - g_0) < 0$ and therefore $\Omega < 0$ (Equations 2.9, 2.20 and 2.24). It is thus favorable for two atoms to have their spins aligned ($\mathcal{F} = 2$) because the interaction for $\mathcal{F} = 0$ is more repulsive. The same result can be deduced from the Hamiltonian that can be rewritten using angular momentum operators, presented in Law, Pu, and Bigelow [52]. For negative Ω , the corresponding

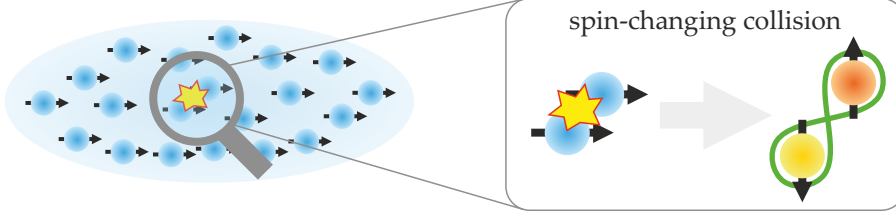


Figure 2.2: Spin-changing collisions create entanglement. A BEC is spin-polarized with $m = 0$. When two atoms collide, the combined spin of $M = 0$ has to be conserved. One possible collision channel is a change of individual spins to $m = +1$ and $m = -1$. This process generates entanglement in the system.

energy is minimized by a maximum collective spin, so the individual spins would align. For $\Omega > 0$, on the other hand, the energy would be minimized by the smallest possible spin, i.e., the single spins would be antiparallel to each other. This gives reasoning to the name *ferromagnetic* interaction for $\Omega < 0$ and *antiferromagnetic* for interactions with $\Omega > 0$. An example for antiferromagnetic interaction is the hyperfine ground state in ^{23}Na or the $F = 2$ hyperfine manifold of ^{87}Rb [67]. For our rubidium spin-1 system, we have $\Omega < 0$ and therefore ferromagnetic interactions [68].

The quadratic Zeeman energy (QZE) q is in general not fixed to zero, but effectively an adjustable parameter. While it can also be varied by the magnetic field itself [69], we employ an mw dressing field as later explained in Section 2.2.3. The total QZE is then the combination of mw and magnetic-field contribution, $q = q_B + q_{\text{mw}}$. Looking at the Hamiltonian 2.25, one can directly see the effect of different values of q . For large positive values, as it is the default case in our experiments due to an applied magnetic field, the energy is minimized when no atoms populate the states $|\pm 1\rangle$ so that the term $q(\hat{N}_1 + \hat{N}_{-1})$ vanishes. This changes when q is turned to large negative values, because a large population in $|\pm 1\rangle$ is now energetically favorable. This defines certain ground states depending on the QZE that will be further investigated in Section 3.2. Not being in the ground state for a certain value of q results in dynamics due to the spin-changing collision term.

A special adjustment is the so-called spin dynamics resonance, where the QZE is adjusted to $q = |\Omega|$ for initially all atoms in $|0\rangle$. For short evolution times, the population in $|0\rangle$ barely changes, $\hat{N}_0 \approx N$, and for large ensembles $N - \frac{1}{2} \approx N$. The collisional shift (last term in Hamiltonian 2.25) thus reduces to $\Omega(\hat{N}_1 + \hat{N}_{-1})$. Remembering that $\Omega < 0$, this shift is now entirely cancelled by the QZE term and the spin-changing collisions are dominant,

$$\hat{H}_{\text{SD,res}} \approx \Omega \left(\hat{a}_1 \hat{a}_{-1} + \hat{a}_1^\dagger \hat{a}_{-1}^\dagger \right). \quad (2.26)$$

This dynamics directly generates the so-called two-mode squeezed vacuum state [64, 70],

$$|\psi(t)\rangle = \sum_{n=0}^{\infty} \frac{(-i \tanh(\Omega t/\hbar))^n}{\cos(\Omega t/\hbar)} |n\rangle_1 \otimes |n\rangle_{-1}, \quad (2.27)$$

that is a superposition of twin-Fock states $|n\rangle_1 \otimes |n\rangle_{-1}$. The population of the twin-Fock states increases exponentially with

$$\langle N_1 + N_{-1} \rangle = 2 \sinh^2(\Omega t / \hbar), \quad (2.28)$$

which gives rise to the entitlement *spin dynamics rate* for Ω . The working point $q/|\Omega| = 1$ is called resonance, because the dynamics is quickest for this value with an initially exponential growth of population in $|\pm 1\rangle$. For a thorough overview and analysis of possible types of entangled states in different experimental systems, consult Pezzè et al. [64].

2.2 INTERNAL DEGREES OF FREEDOM

2.2.1 Collective spins

This section introduces the concept of collective spins, which is a framework to describe our internal atomic spin states, and the Bloch sphere picture that is an elegant visualization of those. It roughly follows Pezzè et al. [64].

A single two-level atom can be described in the framework of (pseudo) spin- $\frac{1}{2}$ particles. For the two modes a (spin-up) and b (spin-down), the atom is then considered to be in the superposition $c_a |a\rangle + c_b |b\rangle$. With probabilities $|c_a|^2$ and $|c_b|^2$ it will then be in the modes a and b , respectively. This single-particle state can be represented on the Bloch sphere by the parametrization

$$|\theta, \varphi\rangle = \cos\left(\frac{\theta}{2}\right) |a\rangle + e^{i\varphi} \sin\left(\frac{\theta}{2}\right) |b\rangle \quad (2.29)$$

with polar angle θ and azimuthal angle φ . The Bloch sphere is defined by the spin operators

$$\begin{aligned} \hat{s}_x &= \frac{1}{2} (|a\rangle \langle b| + |b\rangle \langle a|) \\ \hat{s}_y &= \frac{1}{2i} (|a\rangle \langle b| - |b\rangle \langle a|) \\ \hat{s}_z &= \frac{1}{2} (|a\rangle \langle a| - |b\rangle \langle b|) \end{aligned} \quad (2.30)$$

that are related to the Pauli matrices, $\hat{s}_i = \hat{\sigma}_i/2$, and fulfil $[\hat{s}_i, \hat{s}_j] = i \epsilon_{ijk} \hat{s}_k$. Note that we set $\hbar = 1$ throughout this section. The identity is given by $\hat{s}_0 = |a\rangle \langle a| + |b\rangle \langle b|$. The expectation values of the Pauli operators define the mean spin direction $\{\sin(\theta) \cos(\varphi), \sin(\theta) \sin(\varphi), \cos(\theta)\}$ of state $|\theta, \varphi\rangle$.

The single-particle operators can be easily extended to describe many-particle states of indistinguishable bosons by introducing the collective spin $\hat{J} = (\hat{J}_x, \hat{J}_y, \hat{J}_z)$ that is the sum of N individual spins,

$$\hat{J}_x = \frac{1}{2} (\hat{a}^\dagger \hat{b} + \hat{b}^\dagger \hat{a}), \quad (2.31)$$

$$\hat{J}_y = \frac{1}{2i} (\hat{a}^\dagger \hat{b} - \hat{b}^\dagger \hat{a}),$$

$$\hat{J}_z = \frac{1}{2} (\hat{a}^\dagger \hat{a} - \hat{b}^\dagger \hat{b}) \quad (2.32)$$

with the bosonic annihilation (creation) operators $\hat{a}^{(+)}$ and $\hat{b}^{(+)}$. This is known as the Schwinger boson representation [71]. The \hat{f}_z operator is of particular interest. It is our main experimental observable because it just counts the atom number difference between modes a and b . The total number of particles given by the number operator,

$$\hat{N} = \sum_{i=1}^N \hat{s}_0^{(i)} = \hat{a}^\dagger \hat{a} + \hat{b}^\dagger \hat{b}, \quad (2.33)$$

is conserved because $\langle \hat{s}_0 \rangle = 1$ and therefore $\langle \hat{N} \rangle = N$. Finally, the raising and lowering operators

$$\hat{f}_+ = \hat{a}^\dagger \hat{b}, \quad \hat{f}_- = \hat{b}^\dagger \hat{a} \quad (2.34)$$

are introduced that add or remove one atom in one mode and create one in the other.

The collective spin operators define a generalized Bloch sphere for the collective spin with maximum spin length of $N/2$ (for large N). The poles are defined by all atoms being in a , $|N\rangle_a \otimes |0\rangle_b$, and all atoms in b , $|0\rangle_a \otimes |N\rangle_b$. All other possible superpositions lie on the surface of the Bloch sphere with radius $N/2$.

An exemplary set of states are Dicke states that are the simultaneous eigenstates of \hat{f}_z and $\hat{f}^2 = (\hat{N}/2)(\hat{N}/2 + 1)$ [72],

$$|m_z\rangle = \left| \frac{N}{2} + m, \frac{N}{2} - m \right\rangle = \left| \frac{N}{2} + m \right\rangle_a \otimes \left| \frac{N}{2} - m \right\rangle_b \quad (2.35)$$

with $m \in \{-N/2, -N/2 + 1, \dots, N/2\}$. Those states have $N/2 + m$ particles in mode a and $N/2 - m$ particles in mode b . Hence, they would be represented as a ring on the Bloch sphere with a certain \hat{f}_z and undefined phase. The twin-Fock state from the previous section is a famous example of a Dicke state with equal number of atoms in both modes, such that it resembles a ring around the equator.

Another prominent example of spin states are the coherent spin states [73, 74]. Those states are the product of N indistinguishable single-particle spins pointing in the same mean direction,

$$|\theta, \varphi, N\rangle = \otimes_{i=1}^N \left(\cos\left(\frac{\theta}{2}\right) |a\rangle_i + e^{i\varphi} \sin\left(\frac{\theta}{2}\right) |b\rangle_i \right), \quad (2.36)$$

so every individual qubit is in the same superposition. Those states can also be written as binomial sum of Dicke states [75],

$$|\theta, \varphi, N\rangle = \sum_{k=0}^N e^{-ik\varphi} \sqrt{\binom{N}{k} p^k (1-p)^{N-k}} |k, N-k\rangle \quad (2.37)$$

with $k = N/2 + m$ and $p = \cos(\theta/2)^2$. The latter description can be understood in terms of a binomial probability distribution. Every single-particle state is prepared in a with probability p and in b with probability $1 - p$. A measurement of the N -particle state now results in N measurements of

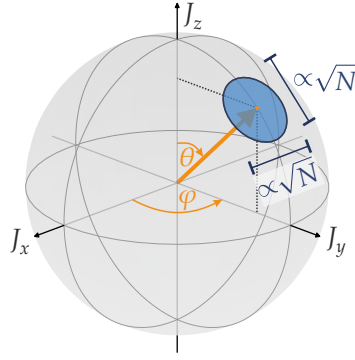


Figure 2.3: Generalized Bloch sphere. An ensemble of N indistinguishable bosons with two modes can be represented on a generalized Bloch sphere with radius $N/2$. The coherent state is displayed as a (blue) disk with radius proportional to \sqrt{N} and mean spin direction $\{\sin(\theta) \cos(\varphi), \sin(\theta) \sin(\varphi), \cos(\theta)\}$ (orange arrow).

the individual spins with corresponding probabilities. This directly gives a hint that a coherent spin state has to obey statistical fluctuations. When measuring the spin orthogonal to the spin direction (e.g. for a spin pointing toward the north pole), the uncertainty relation

$$\Delta \hat{J}_x \Delta \hat{J}_y \geq \frac{1}{2} |\langle \hat{J}_z \rangle| \quad (2.38)$$

has to be fulfilled. Because the spin length (radius of the Bloch sphere) is $\langle \hat{J}_z \rangle \approx N/2$ and the fluctuations are symmetric, uncertainties are given by

$$\Delta \hat{J}_x = \Delta \hat{J}_y = \frac{\sqrt{N}}{2}. \quad (2.39)$$

On the generalized Bloch sphere, such a state is therefore depicted as a disc with mean spin direction $\{\sin(\theta) \cos(\varphi), \sin(\theta) \sin(\varphi), \cos(\theta)\}$ and radius proportional to \sqrt{N} (Figure 2.3).

At the end of this section, some useful relations especially for the $F = 1$ hyperfine manifold are introduced. In principle, this is a spin-1 system that therefore requires collective spin-1 operators [76]

$$\begin{aligned} \hat{L}_x &= \frac{1}{\sqrt{2}} \left(\hat{a}_0^\dagger \hat{a}_1 + \hat{a}_0^\dagger \hat{a}_{-1} + \hat{a}_1^\dagger \hat{a}_0 + \hat{a}_{-1}^\dagger \hat{a}_0 \right), \\ \hat{L}_y &= \frac{1}{\sqrt{2}i} \left(\hat{a}_0^\dagger \hat{a}_1 - \hat{a}_0^\dagger \hat{a}_{-1} - \hat{a}_1^\dagger \hat{a}_0 + \hat{a}_{-1}^\dagger \hat{a}_0 \right), \\ \hat{L}_z &= \hat{a}_{-1}^\dagger \hat{a}_{-1} - \hat{a}_1^\dagger \hat{a}_1 \end{aligned} \quad (2.40)$$

and a spin-1 sphere (Figure 2.4 a). Such a representation is, e.g., described in Kunkel [77]. Unfortunately, some intuitive understanding of pulse sequences that we know from spin- $\frac{1}{2}$ descriptions is lost in this picture. Moreover, we in general restrict our experiments to states with zero magnetization, $L_z = 0$. We will therefore stick to representations on spin- $\frac{1}{2}$ Bloch spheres that also provide an intuitive picture of the dynamics that we will investigate. To this end, we look at a subset of possible states to describe the spin-1 system using spin- $\frac{1}{2}$ operators.

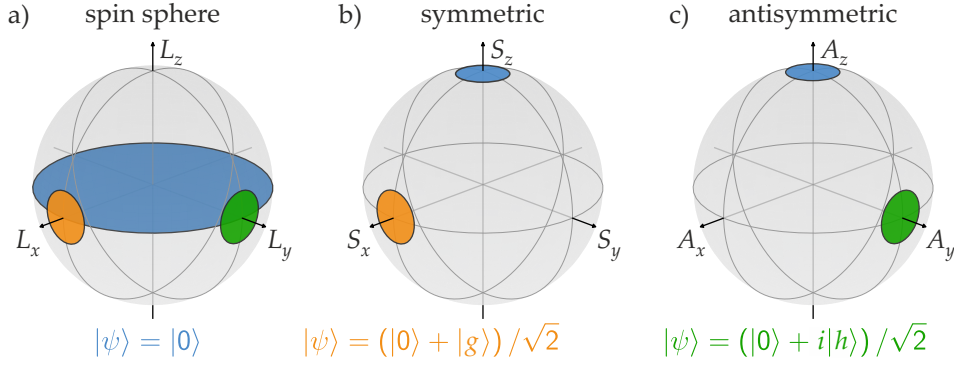


Figure 2.4: Graphical representation of spin states. (a) A spin-1 system can be visualized on a sphere defined by the collective spin-1 operators \hat{L}_x , \hat{L}_y and \hat{L}_z . In this description, a polar state is depicted as a disk in the $\hat{L}_x - \hat{L}_y$ plane, also inside the sphere, because it has vanishing expectation values for all spin operators. (b) The spin-1 system can be reduced to an effective spin- $\frac{1}{2}$ system by a restriction to the symmetric superposition of $|\pm 1\rangle$, spanned by symmetric spin operators $\hat{S}_{x,y,z}$. In this representation, dynamical behavior can be easily visualized on the surface of the sphere, e.g., state transfer or phase evolution. (c) Similar to (b), the system can be reduced using the antisymmetric superposition $|h\rangle$.

First, the symmetric and antisymmetric annihilation (creation) operators are respectively defined by

$$\hat{g}^{(+)} = \frac{1}{\sqrt{2}} (\hat{a}_1^{(+)} + \hat{a}_{-1}^{(+)}), \quad \hat{h}^{(+)} = \frac{1}{\sqrt{2}} (\hat{a}_1^{(+)} - \hat{a}_{-1}^{(+)}) \quad (2.41)$$

with $\hat{a}_{\pm 1}^{(+)}$ being the annihilation (creation) operators for states $|\pm 1\rangle$. Those operators are linked to the symmetric and antisymmetric states,

$$|g\rangle = \frac{1}{\sqrt{2}} (|+1\rangle + |-1\rangle), \quad |h\rangle = \frac{1}{\sqrt{2}} (|+1\rangle - |-1\rangle), \quad (2.42)$$

respectively. We can now introduce the symmetric spin operators $\hat{S}_{x,y,z}$ that correspond to the collective operators $\hat{J}_{x,y,z}$ with state $|g\rangle$ presenting mode b and $|0\rangle$ mode a . In the same way, we define the antisymmetric operators $\hat{A}_{x,y,z}$ with states $|h\rangle$ and $|0\rangle$. Those two operator sets define individual symmetric or antisymmetric Bloch spheres (Figure 2.4 b-c). The symmetric and antisymmetric operators are related to the spin-1 operators by

$$\hat{L}_x = 2\hat{S}_x, \quad \hat{L}_y = 2\hat{A}_y, \quad \hat{L}_z = \hat{N}_{-1} - \hat{N}_{+1}. \quad (2.43)$$

In general, we only work in the space spanned by $|0\rangle$ and the symmetric state $|g\rangle$. In this way, we can reduce the complex spin-1 system to an easier pseudo spin- $\frac{1}{2}$ system that we can well describe and visualize on the Bloch sphere.

2.2.2 Energy level structure

After we described spin states from a more fundamental point of view, we now want to look into the energy structure of the different states. We only

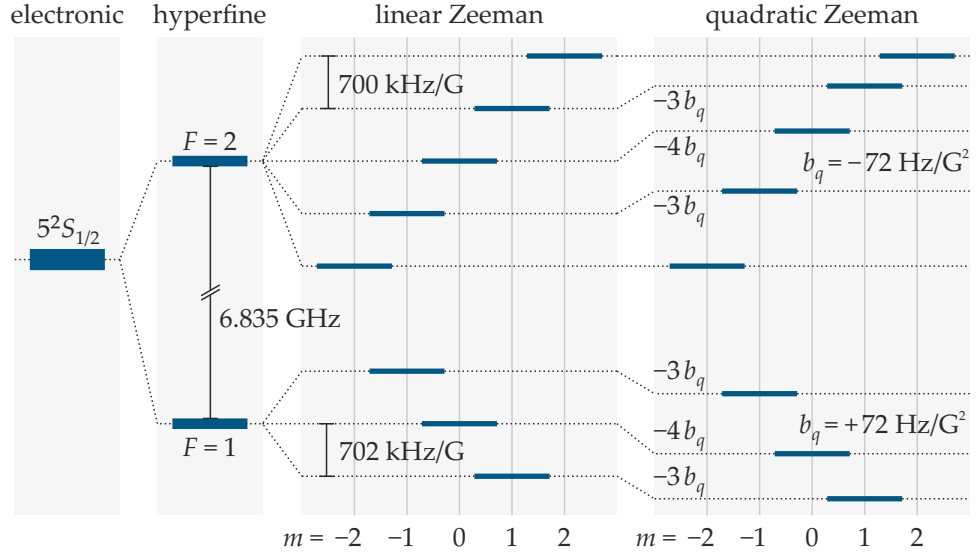


Figure 2.5: Level structure of the electronic ground state of ^{87}Rb . The electronic ground state $5^2S_{1/2}$ features two hyperfine manifolds with $F \in \{1, 2\}$ that are separated by an energy difference corresponding to mw radiation. The Zeeman splitting of the respective $2F + 1$ substates is presented in terms of the linear and quadratic splitting. Energy differences in this diagram are not to scale.

consider ^{87}Rb here and in particular look at the electronic ground state. The resulting internal states in the $5^2S_{1/2}$ ground state are presented in Figure 2.5.

The first energetic splitting of this state occurs due to hyperfine splitting. The total angular momentum \vec{F} is a combination of the total electronic angular momentum \vec{J} and the nuclear spin \vec{I} . It is therefore quantized,

$$|\vec{F}| = \hbar \sqrt{F(F+1)}, \quad |J - I| \leq F \leq J + I \quad (2.44)$$

with quantum numbers $J = 1/2$ and $I = 3/2$ for the electronic ground state of ^{87}Rb . This results in $F \in \{1, 2\}$ for the total angular momentum. Due to the coupling of the nuclear magnetic moment and the magnetic field generated by the electrons, an energy shift occurs depending on the spin orientation. This energy shift of the F -states with respect to the $5^2S_{1/2}$ state is [78]

$$\Delta E_F^{(\text{HFS})} = \frac{E_{\text{HFS}}}{4} [F(F+1) - I(I+1) - J(J+1)] = \begin{cases} -\frac{5}{8} E_{\text{HFS}} & \text{if } F = 1, \\ +\frac{3}{8} E_{\text{HFS}} & \text{if } F = 2, \end{cases} \quad (2.45)$$

with the hyperfine energy splitting [79]

$$E_{\text{HFS}} = h \cdot 6.834682610904307(3.1) \text{ GHz}. \quad (2.46)$$

A further refinement of the level structure becomes visible when an external magnetic field is applied. With such a quantization field, the degeneracy of the $2F + 1$ Zeeman states, labelled $|F, m\rangle$ with the magnetic quantum number $m \in \{-F, \dots, F\}$, is lifted. For the case of the electronic ground state

of ^{87}Rb , the energy shift of those states with respect to the electronic state can be obtained from the Breit-Rabi formula [78, 80]

$$\Delta E_{F,m}^{(\text{HFS,Zeeman})} = -\frac{E_{\text{HFS}}}{8} + m g_I \mu_B B \pm \frac{E_{\text{HFS}}}{2} (1 + m x + x^2)^{1/2} \quad (2.47)$$

with

$$x = \frac{(g_J - g_I) \mu_B B}{E_{\text{HFS}}}, \quad (2.48)$$

the magnetic field strength B , the Bohr magneton μ_B and the g -factors $g_I \approx 10^{-3}$ and $g_J \approx 2$ of the nuclear magnetic moment and the fine structure, respectively [78, 81]. The sign in front of the last term is positive for $F = 2$ and negative for $F = 1$. For weak magnetic fields (small x) the energy shift due to the magnetic field B with respect to the hyperfine energies evaluates to [75]

$$\Delta E_{F,m}^{(\text{Zeeman})} = m g_I \mu_B B \pm \frac{E_{\text{HFS}}}{2} \left(\frac{m}{2} x + \frac{4 - m^2}{8} x^2 \right). \quad (2.49)$$

Introducing the linear and quadratic contributions

$$\begin{aligned} b_p &= \left(g_I \pm \frac{g_J - g_I}{4} \right) \mu_B \approx \begin{cases} 700 \text{ kHz/G} & \text{if } F = 2, \\ -702 \text{ kHz/G} & \text{if } F = 1, \end{cases} \\ b_q &= \pm \left(\frac{g_J - g_I}{4} \right)^2 \frac{\mu_B^2}{E_{\text{HFS}}} \approx \begin{cases} -72 \text{ Hz/G}^2 & \text{if } F = 2, \\ +72 \text{ Hz/G}^2 & \text{if } F = 1, \end{cases} \end{aligned} \quad (2.50)$$

the linear and quadratic Zeeman shifts evaluate to

$$p_B = h b_p B, \quad q_B = h b_q B^2 \quad (2.51)$$

and the total Zeeman shift is given by

$$\Delta E_{F,m}^{(\text{Zeeman})} = m p_B + (m^2 - 4) q_B. \quad (2.52)$$

The Zeeman coefficients are nearly the same for $F = 1$ and $F = 2$, but have a different sign. Interestingly, the small nuclear g_I factor, which is often omitted for simplicity, is responsible for a difference in b_p .

The eight Zeeman states, three in $F = 1$ and five in $F = 2$, comprise the experimental playground of the internal states in our rubidium system. In this work, we will focus on the interaction in the $F = 1$ spin-1 system and use the Zeeman states in $F = 2$ just as assistance, e.g., for storage of atomic modes or for phase readout on the clock transition. The next section describes how the different states can be coupled by rf and mw radiation.

2.2.3 Coupling to electromagnetic radiation

Coupling of the internal states can occur between states in different hyperfine manifolds, but also between states within the same F -state. According to

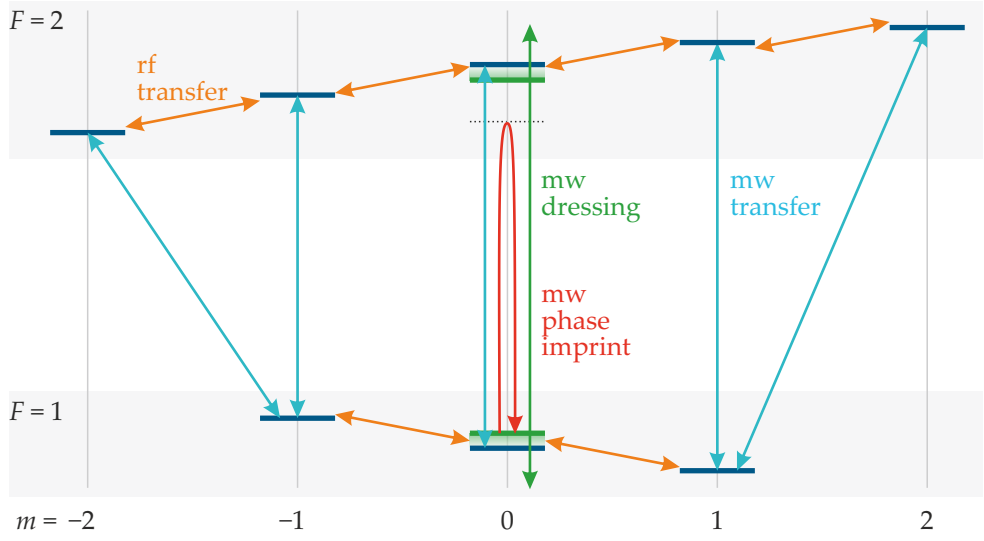


Figure 2.6: Relevant coupling of internal states. The two hyperfine manifolds can be coupled by mw radiation on the order of 6.835 GHz. Different transitions between $F = 1$ and $F = 2$ only differ on the order of the linear Zeeman shift in the MHz range. These transitions can be employed for state transfer of adjustable fraction (blue). Note that not all possible transitions are indicated for better clarity of the figure. Within the individual manifolds, states are coupled by rf signals (orange). Due to the quadratic Zeeman shift, these signals cannot be perfectly on resonance for all the transitions. The difference in resonance frequency is, however, very small with hundreds of Hz. Another use case of mw radiation is the dressing of states (green). For the case of $|1,0\rangle \leftrightarrow |2,0\rangle$, positively detuned frequencies shift the states toward each other, depicted by shifted green states. Finally, mw radiation can be employed to solely imprint a phase when a certain detuning and duration are chosen (red).

the previous section, the energy difference of two states $|F, m\rangle$ and $|F', m'\rangle$ is on the order of the hyperfine splitting E_{HFS} for $F \neq F'$, which presents mw radiation. For $F = F'$, the energy scale is given by the linear Zeeman coefficient $p_B \gg q_B$, corresponding to rf signals for magnetic fields of $B \approx 1$ G. The relevant coupling processes within the scope of this work are shown in Figure 2.6.

As the wavelengths of the signals range from the centimeter scale up to kilometers, the radiation is assumed to be homogeneous over the spatial extent of the cloud, i.e., typically tens of micrometers. Hence, the atoms experience only a temporal change in the electromagnetic field and not a spatial gradient. This dipole approximation is important to ensure the same coherent interaction for all atoms in the BEC.

Electromagnetic radiation has an electric component, inducing a Stark shift [82], and a magnetic part, giving rise to a Zeeman shift [83]. In general, the electric component of an electromagnetic field is dominating over the magnetic part, as the linear Stark effect is a factor of $1/\alpha$ larger than the Zeeman effect with the fine-structure constant $\alpha \approx 1/137$ [84]. For transitions within the $5^2S_{1/2}$ manifold with orbital angular momentum $l = 0$, however,

the dipole moment vanishes and we are left with the magnetic component coupling to the electronic spin.

Selection rules furthermore restrict transitions to $\Delta m = 0$ (π -polarized) or $\Delta m = \pm 1$ (σ^\pm -polarized) because the angular momentum of the combined atom-photon system has to be conserved [85].

For the following considerations, we assume a two-level system of modes a and b with an energy difference of $\Delta E = E_a - E_b = \hbar \omega_0$. Those two states are coupled by a monochromatic electromagnetic field of frequency ω , which is close to the atomic resonance frequency ω_0 , but relatively far detuned from all other transitions that are therefore neglected. The frequency difference between electromagnetic field and atomic transition frequency is the detuning $\delta = \omega - \omega_0$. This reduction to a two-level system is of course not true in general, but sufficient for now.

Transitions corresponding to mw frequency differences are driven between mode a in $F = 2$ and b in $F = 1$ and described by the Hamiltonian

$$\begin{aligned}\hat{H}_{\text{mw}} &= \frac{\hbar \Omega_{\text{mw}}}{2} \left(e^{-i\phi} \hat{a}^\dagger \hat{b} + e^{i\phi} \hat{b}^\dagger \hat{a} \right) - \frac{\hbar \delta}{2} (\hat{N}_a - \hat{N}_b) \\ &= \frac{\hbar \Omega_{\text{mw}}}{2} \left(e^{-i\phi} \hat{J}_+ + e^{i\phi} \hat{J}_- \right) - \hbar \delta \hat{J}_z \\ &= \hbar \Omega_{\text{mw}} (\cos(\phi) \hat{J}_x + \sin(\phi) \hat{J}_y) - \hbar \delta \hat{J}_z.\end{aligned}\tag{2.53}$$

The effect of such an mw coupling depends crucially on the resonant Rabi frequency Ω_{mw} , the phase ϕ of the mw field and the detuning δ . For the resonant case $\delta = 0$, an mw pulse results in a transfer of atoms between a and b , which can be understood as spin rotations with rotation frequency Ω_{mw} . Depending on the mw phase ϕ , a relative phase is imprinted onto the atoms. A detuning δ furthermore adds an additional phase and tilts the rotation axis.

For every atom in the ensemble, there is a probability $P_{a,b}(t)$ to find it in state a or b after employing mw radiation for a time t . As this operation acts collectively on all atoms, it can then be expected for a total of N atoms to find $N_{a,b}(t) = P_{a,b}(t) \cdot N$ atoms in the corresponding states after the mw pulse.

The probability $P_{a,b}$ is the absolute square of the corresponding oscillation amplitudes,

$$P_{a,b}(t) = |c_{a,b}(t)|^2.\tag{2.54}$$

For all atoms initially in a , those state coefficients are

$$\begin{aligned}c_b(t) &= \left[-i \frac{\Omega_{\text{mw}}}{\tilde{\Omega}_{\text{mw}}} \sin\left(\frac{1}{2} \tilde{\Omega}_{\text{mw}} t\right) \right] e^{i\phi} e^{i\delta t/2}, \\ c_a(t) &= \left[\cos\left(\frac{1}{2} \tilde{\Omega}_{\text{mw}} t\right) - i \frac{\delta}{\tilde{\Omega}_{\text{mw}}} \sin\left(\frac{1}{2} \tilde{\Omega}_{\text{mw}} t\right) \right] e^{i\delta t/2}\end{aligned}\tag{2.55}$$

with the generalized Rabi frequency $\tilde{\Omega}_{\text{mw}} = \sqrt{\Omega_{\text{mw}}^2 + \delta^2}$.

The expected number of atoms in state b after an mw pulse and initially all atoms in a is therefore

$$\frac{N_b}{N}(t) = P_b(t) = \frac{\Omega_{\text{mw}}^2}{\tilde{\Omega}_{\text{mw}}^2} \sin^2\left(\frac{1}{2} \tilde{\Omega}_{\text{mw}} t\right).\tag{2.56}$$

For the resonant case with $\delta = 0$, an mw pulse of duration $\tau_\pi = \pi/\Omega_{\text{mw}}$ results in a complete transfer of the initial population (' π pulse') and a pulse of duration $\tau_{\pi/2} = \pi/(2\Omega_{\text{mw}})$ creates an equal superposition of ground and excited state (' $\pi/2$ pulse'). When a detuning is present, the complete transfer cannot be reached and the oscillation becomes faster. These oscillations are known as Rabi oscillations [70, 86]. Note that mw sources often have mixed polarizations instead of a single one. This can cause cross transfer of the opposite circular polarization for the near-resonant transitions $|1,0\rangle \leftrightarrow |2,\pm 1\rangle$ and $|2,0\rangle \leftrightarrow |1,\pm 1\rangle$. Boguslawski [87] presents polarization-selective antenna designs that would be beneficial to solely drive the desired transition and therefore suppress cross coupling.

An mw pulse does not only change the population, but can also alter the phase, which is only visible looking at the oscillation amplitudes and not the probabilities. One option to imprint a phase is via the mw phase ϕ . A pure phase imprint without changing the population, however, requires $\tilde{\Omega}_{\text{mw}} t = 2\pi$, such that the terms including the mw phase vanish. At this time $\tau_{2\pi} = 2\pi/\tilde{\Omega}_{\text{mw}}$

$$c_a(\tau_{2\pi}) = -e^{i\delta\pi/\tilde{\Omega}_{\text{mw}}} = e^{i\pi(\delta/\tilde{\Omega}_{\text{mw}}+1)}, \quad (2.57)$$

so there is a phase of $\pi(\delta/\tilde{\Omega}_{\text{mw}} + 1)$ imprinted that can be adjusted by the detuning δ . To obtain a desired phase shift of ϕ , corresponding detuning

$$\delta(\phi) = \frac{(\phi - \pi)\Omega_{\text{mw}}}{\sqrt{1 - (\phi - \pi)^2}} \quad (2.58)$$

and duration

$$\tau(\phi) = \frac{2\pi\sqrt{1 - (\phi - \pi)^2}}{\Omega_{\text{mw}}} \quad (2.59)$$

have to be chosen for the mw pulse. It is important to mention that this phase imprint is just a global phase for the atoms being in superpositions of a and b only. The effect of the phase imprint is therefore only visible when additional states are involved. For a superposition of all states in $F = 1$, e.g., such a detuned pulse on $|1,0\rangle \leftrightarrow |2,0\rangle$ would imprint a phase between $|1,\pm 1\rangle$ and $|1,0\rangle$.

After mw transfer and mw phase imprint, the last presented coupling of mw signals to the internal states is mw dressing. Electromagnetic radiation does not only lead to coupling between the bare states a and b , but also induces energy shifts due to the AC Stark effect. This can be understood by looking at the eigenvalues and eigenstates of the coupled atom-light system that are no longer the bare states of the atoms only. From the new eigenvalues, the shift with respect to the bare states can be calculated. For each of the two participating states, the energy shift is [70, 88]

$$q_{\text{mw}} = \frac{\hbar\delta}{2} \left(\sqrt{1 + \frac{\Omega_{\text{mw}}^2}{\delta^2}} - 1 \right) \approx \hbar \frac{\Omega_{\text{mw}}^2}{4\delta}. \quad (2.60)$$

The energy shift due to off-resonant mw dressing can be adjusted by either the detuning δ or by the Rabi frequency Ω_{mw} that is related to the mw power. For red detuning ($\delta < 0$), the levels are shifted apart, while blue detuning ($\delta > 0$) brings them closer. Together with the quadratic Zeeman shift due to the magnetic field q_B , the effective QZE $q = q_B + q_{\text{mw}}$ is defined. The adjustment of this QZE can be employed to initiate spin dynamics and drive quantum phase transitions. It is therefore a crucial experimental tool for this work.

Finally, some light is shed onto rf transitions. The variation of the different transition frequencies within a single hyperfine manifold is only on the order of the quadratic Zeeman effect, which is in general not resolved by rf sources. Population therefore emerges among all states when an rf pulse is applied. Moreover, standard rf sources emit linearly polarized signals that drive σ^+ and σ^- transitions simultaneously. Together with the fact that the linear Zeeman shift is nearly equal for $F = 1$ and $F = 2$, transitions occur in general in both manifolds at the same time. In Section 5.3, we will present a setup that utilizes the different polarization response for state-selective rf transfer.

Considering $F = 1$ only, the interaction of the internal states with the rf field is given by

$$\begin{aligned} \hat{H}_{\text{rf}} = & q (\hat{N}_1 + \hat{N}_{-1}) + \hbar \delta (\hat{N}_1 - \hat{N}_{-1}) \\ & + \frac{\hbar \Omega_{\text{rf}}}{2\sqrt{2}} \left(e^{i\phi} \hat{a}_0^\dagger \hat{a}_1 + e^{-i\phi} \hat{a}_0^\dagger \hat{a}_{-1} + e^{-i\phi} \hat{a}_1^\dagger \hat{a}_0 + e^{-i\phi} \hat{a}_{-1}^\dagger \hat{a}_0 \right). \end{aligned} \quad (2.61)$$

Employing the spin operators \hat{S}_x and \hat{A}_y and neglecting the small contributions of the quadratic Zeeman shift q and the detuning δ ,

$$\hat{H}_{\text{rf}} \approx \hbar \Omega_{\text{rf}} (\cos(\phi) \hat{S}_x - \sin(\phi) \hat{A}_y). \quad (2.62)$$

Remember that \hat{S}_x only acts on the symmetric subspace and \hat{A}_y only on the antisymmetric. By definition¹, $\phi = 0$ for the first rf pulse. This pulse then sets the phase reference for all subsequent pulses. An rf pulse can therefore be understood as a spin rotation around \hat{S}_x , i.e., a transfer of atoms between $|1, 0\rangle$ and the symmetric superposition $|g\rangle$. When the first pulse, e.g., transfers all atoms to $|g\rangle$, a second pulse with an rf phase of $\phi = \pi/2$ would have no effect on the atoms.

¹ The rotation axis of the rf pulse is actually defined by the phase difference between the rf phase and the relative phase $\varphi_1 - \varphi_{-1}$ of the states $|1, \pm 1\rangle$.

QUANTUM PHASES IN SPINOR BOSE-EINSTEIN CONDENSATES

In our experimental system of a ferromagnetic spin-1 BEC in the subspace of zero magnetization, we can prepare and observe a vast number of possible quantum states. To structure this large Hilbert space, possible states can be clustered into groups with common (macroscopic) properties, i.e., into different quantum phases. This chapter briefly describes those quantum phases, beginning by a motivation of the mean-field limit. Subsequently, ground-state and excited-state quantum phases are presented with a focus on the latter.

3.1 MEAN-FIELD LIMIT

Phase transitions can be identified by a diverging density of states in the thermodynamic limit $N \rightarrow \infty$. To investigate quantum phases, large atomic ensembles are thus described by a mean-field model. This section motivates this description for our atomic system and introduces the corresponding mean-field Hamiltonian.

Interactions are an inherent feature of spinor BECs. The analysis of all those interactions of every atom with every other atom in the BEC is, however, quite challenging. When single-particle interactions and their inherent quantum fluctuations are disregarded, the interactions can be represented by a mean field caused by all surrounding particles that acts on one particle. For a coherent state, the relative fluctuations $\Delta J_{x,y}/N \propto 1/\sqrt{N}$ become smaller for increasing ensemble size. Considering large atom numbers, the quantum fluctuations are thus negligible and the coherent state can be described by the expectation values of the spin operators, i.e., by a single point on the Bloch sphere. This consideration becomes more acceptable the more atoms are in the ensemble and for $N \rightarrow \infty$ this is then the mean-field limit that can be understood as a classical description of a BEC.

This treatment does intrinsically not include any correlations. Note that quantum fluctuations are in principle absolutely relevant in our system and that the underlying Hamiltonian generates beyond-mean-field effects especially in the vicinity of phase transitions, e.g., entangled spin-squeezed states [89] as also discussed in the outlook (Chapter 7.1). In such cases, when correlations become relevant, a treatment must be chosen that goes beyond the mean field. For the characterization of ESQPTs in the context of this work, however, we do not expect deviations from the mean-field assumption, as also indicated by simulations [47].

We now want to briefly introduce the mean-field Hamiltonian. For a detailed description, please refer to the supplemental material of Feldmann et al. [47], whose notation we mainly use here. It is assumed that all atoms

occupy a single spatial mode and a single spin state, which is a superposition of Zeeman states (' N -particle coherent state') [46, 90],

$$|\vec{\alpha}, N\rangle = |\vec{\alpha}\rangle^{\otimes N} = \frac{1}{\sqrt{N!}} \left(\sum_m \alpha_m \hat{a}_m^\dagger \right)^N |\text{vac}\rangle, \quad (3.1)$$

where $|\text{vac}\rangle$ is the vacuum state and $\vec{\alpha} = (\alpha_1, \alpha_0, \alpha_{-1})$. For those states, a polar parametrization can be defined as

$$\alpha_m = \sqrt{n_m} e^{i\varphi_m}, \quad |\alpha_m|^2 = n_m, \quad \sum_m n_m = 1 \quad (3.2)$$

with relative population $n_m = N_m/N$ and phase φ_m . The individual phases can be connected by a relative phase $\varphi = \varphi_0 - (\varphi_1 + \varphi_{-1})/2$.

The annihilation operator for mode m obeys

$$\hat{a}_m |\vec{\alpha}, N\rangle = \sqrt{N} \alpha_m |\vec{\alpha}, N-1\rangle. \quad (3.3)$$

For a large system, where $N-1 \approx N$, this motivates the replacements

$$\hat{a}_m \rightarrow \sqrt{N} \alpha_m, \quad \hat{a}_m^\dagger \rightarrow \sqrt{N} \alpha_m^* \quad (3.4)$$

and therefore also the exchange of other operators by c-numbers, such as $\hat{N}_0 = \hat{a}_0^\dagger \hat{a}_0 \rightarrow N |\alpha_0|^2 = N_0$. Using such replacements for $N \rightarrow \infty$, we can identify the mean-field Hamiltonian density from the spin Hamiltonian 2.25, i.e., the energy per particle

$$h_{\text{mf}}(\vec{\alpha}) = \lim_{N \rightarrow \infty} \langle \vec{\alpha}, N | \frac{\hat{H}_{\text{SD}}}{N} | \vec{\alpha}, N \rangle. \quad (3.5)$$

This energy is furthermore expressed in units of the interaction strength $\Omega < 0$ and subsequently labelled

$$\eta := \frac{h_{\text{mf}}(\vec{\alpha})}{|\Omega|} = \frac{q}{|\Omega|} (1 - n_0) - 2(1 - n_0) n_0 \cos^2(\varphi) \quad (3.6)$$

with the relative population $n_0 = N_0/N$.

This energy (density) η is an important parameter when it comes to the analysis of ground- and excited-state quantum phases, as the next sections will show.

3.2 GROUND-STATE QUANTUM PHASES

Ground-state quantum phases have been explored theoretically and experimentally. First studies concerning ground-state quantum phases in spinor BECs focussed on a general investigation of the phase diagram [8, 46, 67]. In the following, ground-state quantum phases are described for the case of ferromagnetic interactions ($\Omega < 0$) and zero magnetization ($N_{+1} = N_{-1}$).

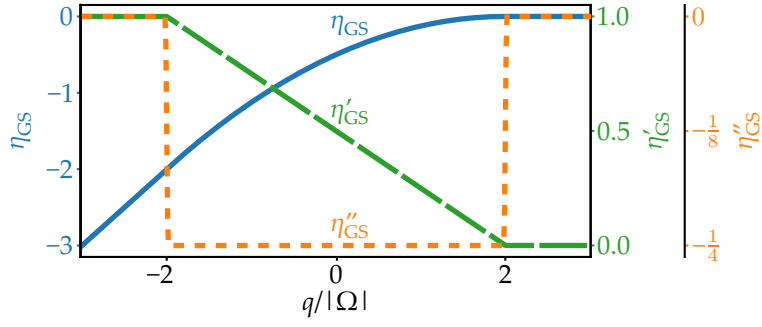


Figure 3.1: Ground-state energy and its derivatives. The ground-state energy η_{GS} (solid blue), its first derivative (dashed green) and the second derivative (dotted orange) are shown with corresponding axes. The second derivative shows a discontinuity that indicates a phase transition.

To obtain the ground-state energies, the mean-field Hamiltonian 3.6 is minimized. As a function of $q/|\Omega|$, this yields

$$\eta_{\text{GS}} = \begin{cases} \frac{q}{|\Omega|} & \text{if } \frac{q}{|\Omega|} \leq -2, \\ -\frac{1}{8} \left(\frac{q}{|\Omega|} - 2 \right)^2 & \text{if } -2 < \frac{q}{|\Omega|} < 2, \\ 0 & \text{if } \frac{q}{|\Omega|} \geq 2. \end{cases} \quad (3.7)$$

The ground-state energy and its derivatives are depicted in Figure 3.1. It can be seen that the second derivative shows two discontinuities. This discontinuous behavior indicates a (second-order) phase transition [91] at those points. Therefore, three distinct ground-state quantum phases can be expected with phase transitions at $q/|\Omega| = \pm 2$. Interestingly, this differs from the mean-field predictions of the general Hamiltonian including magnetization because a phase transition at $q/|\Omega| = 0$ is postponed to $q/|\Omega| = -2$ [92].

A different indication of a phase transition is a closing energy gap between ground and first excited state that corresponds to a large ground-state degeneracy at this point [93]. In the thermodynamic limit, the energy gap can be analytically calculated to be [46, 69, 94]

$$\frac{\Delta E}{|\Omega|} = \begin{cases} 2 \sqrt{\left(\frac{q}{|\Omega|} \right)^2 + 2 \frac{q}{|\Omega|}} & \text{if } \frac{q}{|\Omega|} \leq -2, \\ 2 \sqrt{1 - \frac{1}{4} \left(\frac{q}{|\Omega|} \right)^2} & \text{if } -2 < \frac{q}{|\Omega|} < 2, \\ 2 \sqrt{\left(\frac{q}{|\Omega|} \right)^2 - 2 \frac{q}{|\Omega|}} & \text{if } \frac{q}{|\Omega|} \geq 2. \end{cases} \quad (3.8)$$

This also predicts vanishing energy gaps and thus ground-state quantum phase transitions at $q/|\Omega| = \pm 2$. Experimentally, a non-zero energy gap of $\Delta E/|\Omega| = 0.15(1)$ has been measured at the phase transition point $q/|\Omega| = 2$ for a finite atom number of $N = 40\,000$ [69]. This can be explained by

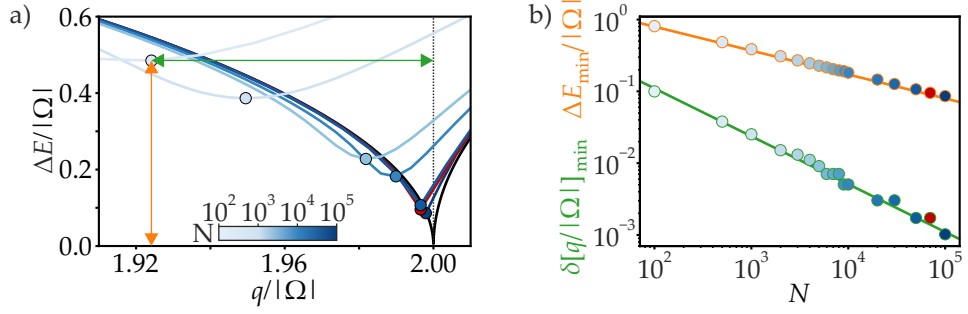


Figure 3.2: Energy gap between ground and first excited state. (a) The energy gap $\Delta E/|\Omega|$ depends on the atom number N that is indicated by a color scaling from light ($N = 10^2$) to dark blue ($N = 10^5$). Red color corresponds to the atom number $N = 70\,000$ employed for the main results in this work and black to the mean-field prediction. Lines present numerical simulations of the energy gap and dots the corresponding minima. For large N , the energy gap becomes increasingly smaller and the position gets closer to the expected mean-field prediction. (b) For increasing atom number N , the minimum energy gap (orange) decreases and the position of this minimum (green) gets closer to the mean-field prediction. The values for the dots are extracted from simulations as in (a) and the solid lines present fits to those values.

effects beyond the mean-field description. Exact diagonalization of the spin Hamiltonian 2.25 (Appendix A.1) yields eigenenergies that indeed have a minimal, but non-zero energy gap at $q/|\Omega| = \pm 2$ (Figure 3.2). It can be seen that there is a strong dependency of the energy gap size on the number of employed atoms in the numerical simulations. The minimum gap size follows the predicted scaling of $\Delta E_{\min}/|\Omega| = 7.4 N^{-1/3}/2$ [92] and actually vanishes in the thermodynamical limit. The same effect can be expected for the phase transition at $q/|\Omega| = -2$, but for all other values of $q/|\Omega|$, the energy gap is large and finite even in the limit $N \rightarrow \infty$. Notably, also the relative position of the energy gap minimum changes with $\delta[q/|\Omega|]_{\min} = (2 - [q/|\Omega|]_{\min})/2 = 4.7 N^{-2/3}/2$ according to our fit. Due to the large ensemble of $N = 70\,000$ atoms that we employ in our investigations (highlighted in Figure 3.2 in red), the deviations from the mean-field limit are expected to be negligible.

Experimentally, neither the second derivative of the energy with respect to the QZE, nor the vanishing energy gap are easily accessible to experimentally distinguish quantum phases. However, the atom number distribution between $|0\rangle$ and the symmetric superposition $|g\rangle$ presents an appropriate order parameter [46, 67, 92]. The ground-state energy η_{GS} is reached for a relative phase $\varphi \in \{0, \pi\}$ and relative population

$$n_0 = \begin{cases} 0 & \text{if } \frac{q}{|\Omega|} \leq -2, \\ \frac{1}{4} \left(\frac{q}{|\Omega|} + 2 \right) & \text{if } -2 < \frac{q}{|\Omega|} < 2, \\ 1 & \text{if } \frac{q}{|\Omega|} \geq 2 \end{cases} \quad (3.9)$$

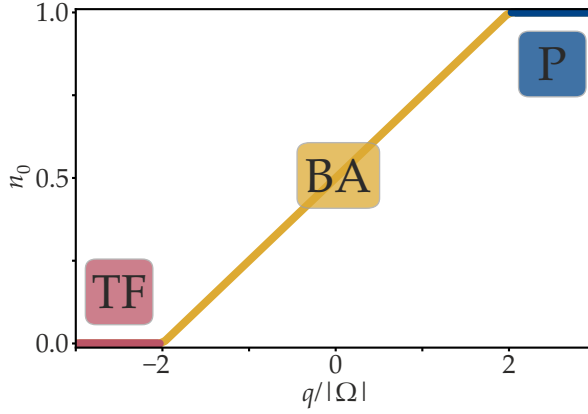


Figure 3.3: Order parameter for ground-state quantum phase transitions. Depending on the QZE $q/|\Omega|$, the ground state of a spinor condensate differs. For large positive or negative values, $|q/|\Omega| \gg 2$, the ground state is a polar state $|0, N, 0\rangle$ with $n_0 = 1$ or a twin-Fock state $|N/2, 0, N/2\rangle$ with $n_0 = 0$, respectively. Between the polar and the twin-Fock phase, the atom number distribution of the ground state depends linearly on $q/|\Omega|$.

as shown in Figure 3.3. This presents a suitable order parameter to distinguish ground-state quantum phases.

An intuitive understanding for this dependency of n_0 on $q/|\Omega|$ can be given by the spin Hamiltonian 2.25 and the energy level picture. For large $|q/|\Omega|$, the Hamiltonian is $\hat{H}_{\text{SD}} \approx q(\hat{N}_{+1} + \hat{N}_{-1})$. The energy is thus minimized by $(N_{+1} + N_{-1}) = 0$ for large and positive q and by $(N_{+1} + N_{-1}) = N$ for large and negative q . For $q/|\Omega| \gg 2$, it is thus energetically favorable for the atoms to be in $|0\rangle$. The corresponding many-body ground state is then $|0\rangle_1 \otimes |N\rangle_0 \otimes |0\rangle_{-1} = |0, N, 0\rangle$. This state is called polar state and the quantum phase for $q/|\Omega| > 2$ is the polar (P) phase. When the $|0\rangle$ mode is now shifted upwards in energy due to mw dressing, at some point ($q/|\Omega| = 2$) the q contribution to the Hamiltonian is competing with the spin-changing collision term and some pairs of atoms are transferred to $|\pm 1\rangle$. A linear relationship between n_0 and $q/|\Omega|$ persists until $q/|\Omega| = -2$, where the $|0\rangle$ state is shifted upwards so much that it is energetically unfavorable to populate it. Instead, all the atoms are in $|+1\rangle$ and $|-1\rangle$. The many-body ground state for large and negative $q/|\Omega|$ is the twin-Fock state $|N/2, 0, N/2\rangle$, giving rise to the name twin-Fock (TF) phase for $q/|\Omega| < -2$. In the linear regime between P and TF phases, the many-body ground state has some atoms in $|\pm 1\rangle$. For example, at $q = 0$, the $|0\rangle$ state and the symmetric superposition $|g\rangle$ are energetically degenerate. It is therefore no surprise that the atoms equally populate both states, i.e., $|N/4, N/2, N/4\rangle$. This central phase is called broken-axisymmetry (BA) phase [94] and it exhibits strong nonclassical features like macroscopic superposition states that resemble NOON states [95, 96].

The ground-state quantum phase diagram is of particular interest for quantum state engineering and the generation of highly entangled states. The adiabatic theorem states that a quantum system remains in its ground state when an external control parameter is varied only gradually [97, 98]. In

the thermodynamic limit, an adiabatic crossing through the phase transition would not be possible because adiabaticity cannot be ensured with a closing energy gap. For finite atom numbers and therefore finite energy gaps, however, such crossings are possible. According to Landau-Zener theory, the excitation probability for an adiabatic passage can be approximated by [69]

$$P_{\text{LZ}} = e^{-\pi\Gamma_{\text{LZ}}/4}, \quad \Gamma_{\text{LZ}} = \frac{(\Delta E)^2}{v_q \frac{d(\Delta E)}{dq}}, \quad (3.10)$$

where a minimum value of $\Gamma_{\text{LZ}} = 10$ is reported sufficient for low excitation probabilities. The quench rate $v_q = \Delta q/\Delta t$ should be low to ensure the ground state without much excitation and large energy gaps ΔE are beneficial, too. Close to the phase transition, adiabaticity is therefore most difficult to ensure, while the rest of the phase diagram is less demanding due to larger energy gaps.

Adiabatic crossing of a phase transition has been reported to be possible in a ferromagnetic spin-1 system with negligible excitation [69]. For an initial polar ground state $|0, N, 0\rangle$, a careful variation of $q/|\Omega|$ through the phase transitions at $q/|\Omega| = \pm 2$ into the TF phase has been experimentally proven to generate highly entangled twin-Fock states [99]. Furthermore, such a crossing of phase transitions has been utilized as a technique to deterministically generate large ensembles of entangled atoms that can serve as a source for inertially sensitive atom interferometry [100]. Furthermore, the generation of massive entanglement is proposed for an adiabatic passage into the BA phase [92, 95, 96], for antiferromagnetic systems [101] and for spinor BECs with macroscopic magnetization [102].

3.3 EXCITED-STATE QUANTUM PHASES

3.3.1 Phase diagram

Ground-state quantum phase transitions can be identified by a vanishing energy gap between the ground and first excited state. Continuing this idea, one can also look at energy gaps of neighboring excited states and locate singularities in their density of states. To this end, energy eigenvalues of the spin Hamiltonian 2.25 are obtained by exact diagonalization (Appendix A.1) and presented in Figure 3.4. The diagram shows different exemplary eigenstates in color while the gray background contains all the eigenenergies computed for 70 000 atoms. In addition, the excitation energy η^* is plotted, which is the ground-state energy subtracted from the mean-field energy (Equation 3.6),

$$\eta^* = \eta - \eta_{\text{GS}}. \quad (3.11)$$

In the interesting range for phase transitions, $-2 \leq q/|\Omega| \leq 2$, this evaluates to

$$\eta^* = \frac{1}{8} \left(\frac{q}{|\Omega|} + 2 \right)^2 - n_0 \frac{q}{|\Omega|} - 2(1 - n_0)n_0 \cos^2(\varphi). \quad (3.12)$$

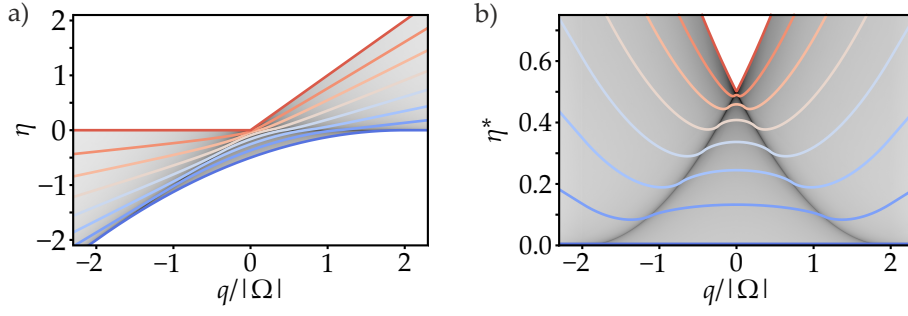


Figure 3.4: Phase diagram of a ferromagnetic spinor BEC. Both diagrams have the QZE $q/|\Omega|$ on the horizontal axis and the energy per atom on the vertical axis. While diagram (a) shows the energy directly obtained from diagonalizing the Hamiltonian, in plot (b) the ground-state energy is subtracted. Colored lines indicate every 5000th eigenstate from low (blue) to high (red) energy, while the background shows the complete set of eigenenergies for $N = 70000$ atoms. Regions of high density of states can clearly be identified in this picture.

The different eigenenergies are very close to each other along two lines in the phase diagram (Figure 3.4) at excitation energies

$$\eta_{\text{QPT}}^* = \frac{1}{8} \left(\left| \frac{q}{\Omega} \right| - 2 \right)^2 \quad (3.13)$$

and $-2 < q/|\Omega| < 2$. These vanishing energy gaps signalize quantum phase transitions of excited states. It can also be shown theoretically that the density of states diverges along η_{QPT}^* in the mean-field description [47]. Hence, three excited-state quantum phases are expected, divided by phase transitions at η_{QPT}^* . As the excited-state phases merge into the ground-state phases for $\eta^* = 0$, we name them TF', BA', P' in analogy to the ground-state phases.

In comparison to the ground-state phase diagram, the excitation energy η^* acts as a second control parameter in addition to the QZE $q/|\Omega|$ (Figure 3.5). Different values of η^* on the one hand qualitatively change the quantum phases for a variation of $q/|\Omega|$, as the BA' phase becomes drastically smaller for higher excitation. On the other hand, the excitation energy alone can cause a phase transition at a fixed QZE. Because the relative population n_0 and relative phase φ present the experimentally adjustable parameters of η^* for a fixed $q/|\Omega|$, the phase diagram is also presented with those control parameters in Figure 3.6. However, for such a representation, one of the two parameters has to be fixed. To this end, the excitation energy η^* is employed in this work as a more general parameter.

The two control parameters η^* and $q/|\Omega|$ constitute a rich phase diagram that deserves further investigation. Excited-state quantum phases have been investigated thoroughly from a theoretical perspective [36, 103, 104] and their existence has been experimentally revealed in microwave Dirac billiards [105] and molecular spectra [38–41]. For some experimental systems, there are even dedicated proposals to distinguish excited-state phases [47–51]. The experimental mapping of an excited-state phase diagram by an appropriate order parameter, however, remains up to now elusive.

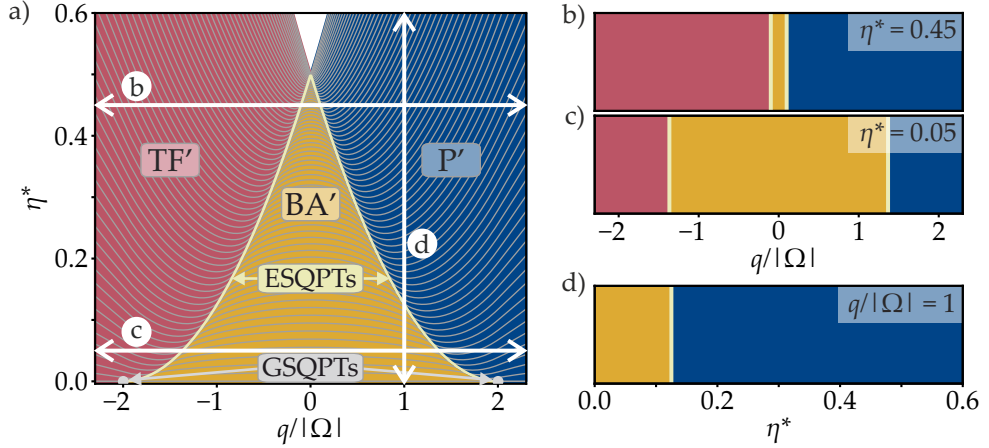


Figure 3.5: Concept of ESQPTs. (a) The excited-state quantum phase diagram is shown with QZE $q/|\Omega|$ on the horizontal and excitation energy η^* on the vertical axis. Gray lines correspond to every 500th eigenenergy for $N = 70\,000$. Ground-state quantum phase transitions (GSQPTs) are located at $q/|\Omega| = \pm 2$ and zero excitation energy (gray dots). ESQPTs are expected for regions with diverging density of states (light yellow lines). They divide the phase diagram into three phases: TF' (red), BA' (orange) and P' (blue). Three exemplary crossings are highlighted with white arrows and presented in (b-d). (b-c) For a variation of $q/|\Omega|$, the appearance of the quantum phases change for different excitation energies. (d) For a fixed QZE, ESQPTs can be driven by a variation of the excitation energy η^* .

In the following, the Bloch sphere is introduced as a helpful representation of the excitation energy. For this visualization, the QZE is fixed to a certain value of $q/|\Omega|$. Then, all pairs (n_0, φ) with equal energies η^* can be summarized as an energy hypersurface [47]. Those different energy hypersurfaces with equal QZE can be depicted together on a Bloch sphere with $|0\rangle^{\otimes N}$ on the north pole and $|g\rangle^{\otimes N}$ on the south pole. Figure 3.7 shows Bloch spheres with $q/|\Omega| = 0.75$ (a) and $q/|\Omega| = -0.25$ (b). Solid black lines represent the energy hypersurfaces and color shading indicates the excitation energy η^* . The two energy control parameters are $n_0 = S_z/N + \frac{1}{2}$ on the z axis and φ as the azimuthal phase. Note that the relative population n_0 can also be mapped to the polar angle θ by $n_0 = (\cos(\theta) + 1)/2$. For $-2 < q/|\Omega| < 2$, the ground state is in the BA' phase (yellow) and corresponds to the stationary point (red dot on the front). A separatrix (dashed lines) presents the border between adjacent phases. For a different value of the QZE, the shape and distribution of the energy hypersurfaces over the sphere changes, such that the same tuple (n_0, φ) leads to different energies for different QZE, as expected from the phase diagram and Equation 3.12.

It is visible in the Bloch sphere representation of Figure 3.7 that the energy hypersurfaces of the three excited-state quantum phases are different. While hypersurfaces in the P' and TF' phases contain all possible phase values, $\varphi \in [0, 2\pi)$, the BA' phase hypersurfaces are bounded in phase. Moreover, the BA' hypersurfaces consist of two closed-loop lines on the front and back of the sphere that are not connected. This distinction is later employed to define an appropriate order parameter.

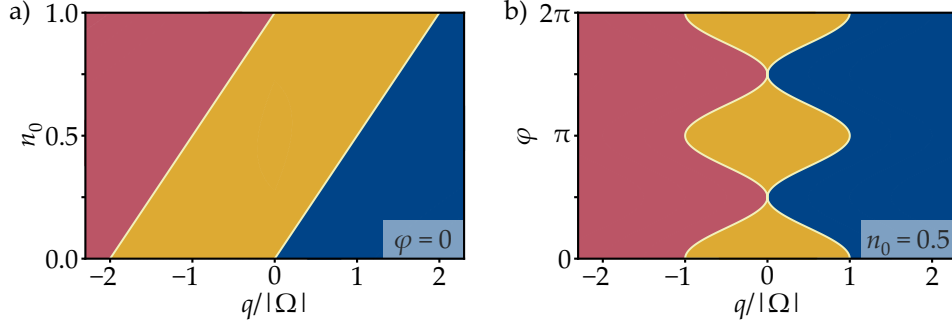


Figure 3.6: Expected quantum phases depending on experimental control parameters. Instead of η^* , the experimentally accessible parameters of relative population n_0 (a) and relative phase φ (b) are shown as the second control parameter. To this end, the phase is fixed in (a) by $\varphi = 0$ and the relative population in (b) by $n_0 = 0.5$. Quantum phases are indicated by color as TF' (red), BA' (yellow) and P' (blue). The yellow line indicates the phase transition.

Up to now, the discussion has always considered energy eigenstates. Experimentally, however, we do not prepare single eigenstates of the Hamiltonian, but coherent superpositions of eigenstates within a narrow energy window. Note that only the preparation step prevents us from investigating the phase diagram also for excited energy eigenstates. Nevertheless, this has drastic consequences, as the eigenstates are stationary, but the coherent states are not. This sounds like a drawback, but is actually beneficial because the coherent states show dynamics that energy eigenstates would not show. The following section describes this dynamics, which is later employed to distinguish different excited-state quantum phases.

3.3.2 Dynamics of excited coherent states

Experimentally, we prepare coherent states within a narrow energy window instead of energy eigenstates. The phase diagram is, however, the same. We can thus use the dynamics of coherent states to map the phase diagram of excited energy eigenstates. In the mean-field limit, the quantum-mechanical operators are replaced by expectation values and coherent states are defined by the mean spin directions. On the Bloch sphere, coherent states $|\vec{\alpha}, N\rangle$ are therefore treated as points. They are defined by (Equation 3.1)

$$\alpha_0 = \sqrt{n_0}, \quad \alpha_1 = \sqrt{\frac{1-n_0}{2}} e^{i\varphi}, \quad \alpha_{-1} = \sqrt{\frac{1-n_0}{2}} e^{i\varphi} \quad (3.14)$$

and therefore described by a pair of relative population n_0 and relative phase φ . Those points undergo dynamics that conserves the excitation energy η^* and is thus restricted to a single energy hypersurface. The time evolution of a coherent state is from now on referred to as trajectory. Classical equations

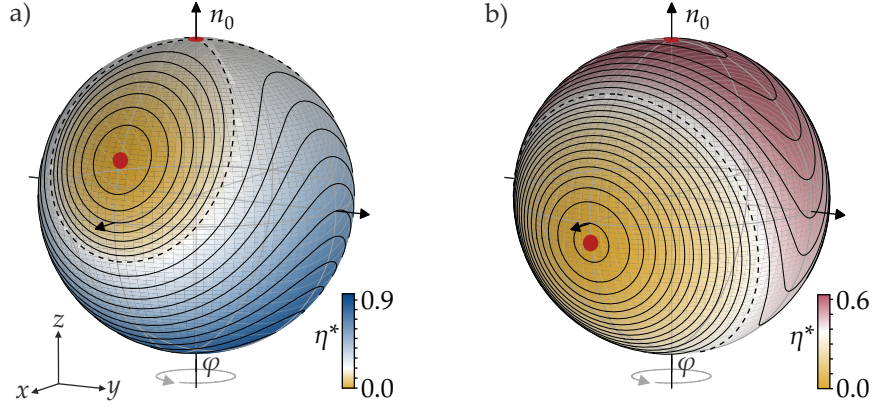


Figure 3.7: Energy hypersurfaces on Bloch spheres. Points in the phase diagram can be depicted on a Bloch sphere with the relative population n_0 on the vertical axis and the relative phase φ as the azimuthal angle. The QZE $q/|\Omega|$ defines the shape of the trajectories and in this sense the accessible energies and phases. Sphere (a) corresponds to $q/|\Omega| = 0.75$ and (b) to $q/|\Omega| = -0.25$. Different excitation energies η^* are associated with different regions on the Bloch sphere surface (color shading). The ground state is located at the stationary point (red) on the front of the sphere. Black lines exemplarily represent different points in phase space with equal energy and dashed lines correspond to the separatrix that separates different phases: The P' phase (blue), BA' (yellow) and TF' (red).

of motion can be defined for the population n_0 and phase φ by the coupled equations [47]

$$\frac{d}{d\tau} n_0 = \frac{\partial}{\partial \varphi} \eta = 4 n_0 (1 - n_0) \cos(\varphi) \sin(\varphi) \quad (3.15)$$

$$\frac{d}{d\tau} \varphi = -\frac{\partial}{\partial n_0} \eta = \frac{q}{|\Omega|} + (2 - 4 n_0) \cos^2(\varphi) \quad (3.16)$$

with $\tau = |\Omega| t / \hbar$. For $q/|\Omega| > 0$, the time-dependent solution for the population is given by [47]

$$n_0(t) = x_2 - (x_2 - x_1) \operatorname{cn}^2 \left(\sqrt{2 \left| \frac{q}{|\Omega|} \right| (x_3 - x_1)} \tau + v, \frac{x_2 - x_1}{x_3 - x_1} \right) \quad (3.17)$$

with

$$\begin{aligned} x_1 &= \frac{1}{4} \left(2 + \left| \frac{q}{|\Omega|} \right| - \sqrt{\left(\frac{q}{|\Omega|} - 2 \right)^2 + 8 \eta} \right), \\ x_2 &= \begin{cases} \frac{1}{4} \left(2 + \left| \frac{q}{|\Omega|} \right| + \sqrt{\left(\frac{q}{|\Omega|} - 2 \right)^2 + 8 \eta} \right) & \text{if } \eta^* < \eta_{\text{QPT}}^*, \\ \left(\frac{q}{|\Omega|} - \eta \right) \left| \frac{q}{|\Omega|} \right|^{-1} & \text{if } \eta^* \geq \eta_{\text{QPT}}^*, \end{cases} \\ x_3 &= \begin{cases} \left(\frac{q}{|\Omega|} - \eta \right) \left| \frac{q}{|\Omega|} \right|^{-1} & \text{if } \eta^* < \eta_{\text{QPT}}^*, \\ \frac{1}{4} \left(2 + \left| \frac{q}{|\Omega|} \right| + \sqrt{\left(\frac{q}{|\Omega|} - 2 \right)^2 + 8 \eta} \right) & \text{if } \eta^* \geq \eta_{\text{QPT}}^* \end{cases} \end{aligned} \quad (3.18)$$

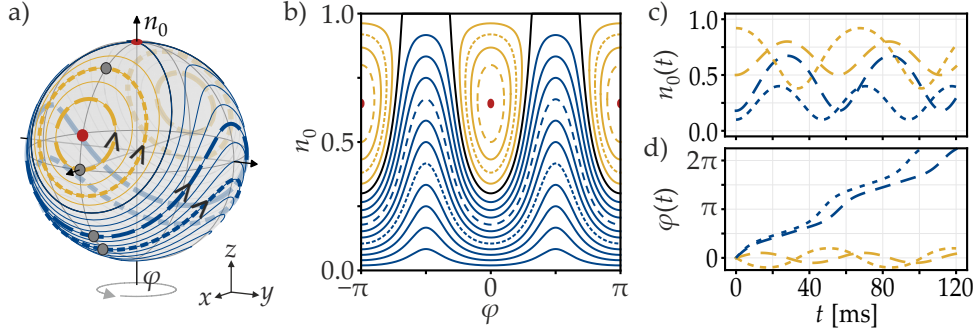


Figure 3.8: Bloch sphere, phase-space diagram and time evolution. All diagrams show energy hypersurfaces for $q/|\Omega| = 0.6$. Values for the initial $n_0(0)$ are 0.1 (blue short dashed), 0.18 (blue long dashed), 0.5 (yellow long dashed) and 0.92 (yellow short dashed). The initial phase is set to $\varphi(0) = 0$. (a) Bloch sphere representation with the four highlighted trajectories. Evolution directions are indicated by small arrows. Small gray circles indicate starting points of the oscillations. (b) Phase space diagram, i.e., a 2D mapping of the Bloch sphere. (c) Time evolution of $n_0(t)$ and $\varphi(t)$. The phase evolution is very different for states in the P' phase and in the BA' phase.

and the Jacobi elliptic cosine $\text{cn}(w, k^2)$. The factor v is extracted by matching $n_0(0)$ to the desired initial value. The corresponding phase $\varphi(t)$ can be obtained employing the relation for η^* in Equation 3.12 and the initial conditions. For $q/|\Omega| < 0$, the solutions are $\tilde{n}_0(t) = (1 - n_0(-t))$ and $\tilde{\varphi}(t) = -\varphi(t)$.

For certain combinations of the QZE $q/|\Omega|$ and the excitation energy η^* , stationary points with $\frac{d}{dt} n_0(t) = 0$ and $\frac{d}{dt} \varphi(t) = 0$ can be observed. There is one saddle point for every $|q/\Omega| \in (0, 2)$ at $n_0 = 1$ ($q/|\Omega| > 0$) or $n_0 = 0$ ($q/|\Omega| < 0$) and two additional stationary points at $\varphi \in \{0, \pi\}$ and

$$n_0 = \frac{1}{4} \left(\frac{q}{|\Omega|} + 2 \right). \quad (3.19)$$

The latter stationary points correspond to the ground-state minima with excitation energy η_{GS} that lie in the BA' phase.

A few exemplary trajectories are presented in Figure 3.8 on the Bloch sphere, the phase space diagram and over time. It can be seen that states within the BA' phase are limited in their phase evolution, while the P' phase consists of states with a running phase, i.e., spanning from 0 to 2π . The phase space of n_0 and φ for spin-1 systems has already been explored theoretically [45, 46] and experimentally to some extent [44, 106]. Interestingly, this phase space is very similar to the one of Josephson oscillations, either in an external double-well system [42, 107, 108] or in a two-component BEC [43] and ultimately to the one of a rigid pendulum [109].

Hence, it was observed before that there are different types of coherent spin dynamics, i.e., one with a bounded and one with a running phase. However, no connection to excited-state quantum phases was made and no order parameter was employed to distinguish the dynamical regimes. Nevertheless, the mentioned experiments are indeed connected to excited-state quantum phases and they could be employed for further investigations.

The previous work shows that the underlying physics is not restricted to spin-1 systems, but can also be connected to others. Therefore, the mapping of an excited-state phase diagram seems to be of general interest.

A first experimental attempt to investigate excited-state quantum phases in spin-1 BECs was made in an antiferromagnetic system of sodium [110]. In this system, there is only one ground-state quantum phase transition from the antiferromagnetic to the polar phase at $q/|\Omega| = 0$. Quenching the system to $q/|\Omega| > 2$, there is nevertheless a nonanalytical behavior of the relative mode populations observed. This is explained by the sudden quench that brings the atoms into the highest excited state where a phase transition indeed occurs at $q/|\Omega| = 2$. Although this experiment nicely signals the existence of ESQPTs, it does not characterize the phases by an appropriate order parameter and it does not employ the energy as a control parameter, but only considers the highest excited state.

3.3.3 Interferometric order parameter

The existing investigations on quantum phase transitions captured only the lowest and highest energy states with the QZE as a single control parameter. The order parameters employed for these experiments, i.e., the relative

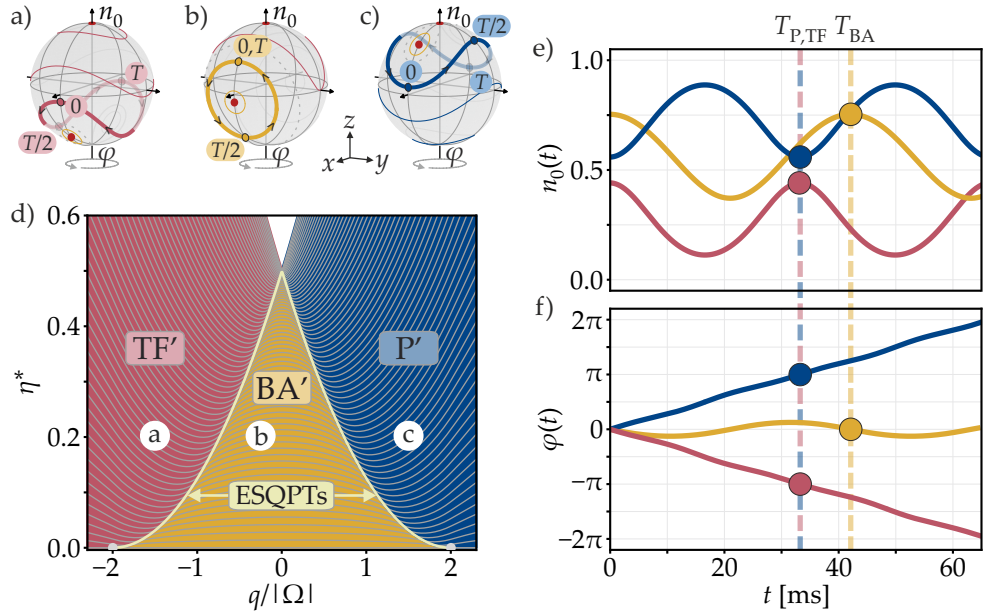


Figure 3.9: Schematic depiction of the interferometric order parameter. (a-c) Bloch sphere representation with highlighted trajectories for $q/|\Omega| = -1.5$ and $n_0(0) = 0.44$ (a), $q/|\Omega| = -0.25$ and $n_0(0) = 0.75$ (b), $q/|\Omega| = 1.5$ and $n_0(0) = 0.56$ (c). The initial phase is $\varphi = 0$. Dots on the corresponding trajectories correspond to the starting point (0), the half period ($T/2$) and the period (T). Small arrows indicate the rotation direction. (d) Phase diagram with the three trajectories marked at the corresponding positions. (e-f) Time evolution of the relative population and phase of the trajectories in (a-c). The population oscillation periods T and related phase values are marked by dots.

population of the spin modes, cannot be applied for the determination of excited-state quantum phases because in contrast to the ground-state, the excited (coherent) states are not static and the population is in general oscillating. It is therefore necessary to apply a different order parameter to distinguish the three excited-state quantum phases. This section now motivates an order parameter following Feldmann et al. [47] that is in general valid for the whole excited-state quantum phase diagram.

The Bloch sphere picture already indicates that the evolution on a trajectory belonging to the BA' phase is qualitatively different from the evolution of a state in the P' or TF' phase. The mean-field trajectories of states in the BA' phase are limited to one side of the sphere while states in P' and TF' phases have a running phase.

This leads to the idea of measuring the phase after a certain time to distinguish the different quantum phases, as proposed in Feldmann et al. [47]. The P' and TF' phases have a periodic behavior in the population oscillation with a period of $T_{P',TF'}$ (Figure 3.9). At exactly one such period, the phase has evolved by $\Delta\varphi = \pm\pi$. For the BA' phase, on the other hand, after such a period $T_{BA'}$, the phase is back at its original value, such that $\Delta\varphi = 0$. This is in general the case for every starting point on the energy hypersurface and we will employ this order parameter experimentally in Chapter 6. If one accepts the restriction to adjust η^* only by a variation of n_0 and keep the relative phase fixed at $\varphi = 0$, another order parameter can be defined. In this configuration, the states are evolving for $T/2$ only. Starting at $\varphi = 0$, states in the P' and TF' phases will evolve to $\varphi = \pm\pi/2$. States in the BA' phase, on the other hand, will be at $\varphi = 0$. This order parameter after one half period $T/2$ is also of particular interest for the experiments described later in Chapter 6. Because every hypersurface can be reached with that initial phase, this still presents a suitable order parameter.

EXPERIMENTAL PLATFORM

This section covers the experimental apparatus utilized to generate and manipulate ^{87}Rb spinor BECs. First, the experimental sequence is briefly presented. A few important parts of this procedure are discussed in more detail thereupon. A sketch of the apparatus and a timeline are shown in Figure 4.1 and a photograph is presented in Figure 4.2.

4.1 BEC GENERATION PROCEDURE

The experimental sequence starts with the preparation of ^{87}Rb atoms in a magneto-optical trap (MOT) [111]. To this end, gaseous rubidium atoms are evaporated from alkali metal dispensers that are heated up by an electric current of 5.2 A for 10 s in every experimental cycle (total duration 25 s) to ensure a constant amount of rubidium. The atoms are deposited in a glass cell (and on its walls) in which an ultra-high vacuum on the order of 10^{-9} to 10^{-10} mbar exists to reduce unwanted collisions with gas particles. To enhance the number of atoms in the center of the cell, light emitting diodes provide ultraviolet light for light-induced atom desorption that removes atoms from the glass walls [112]. A MOT [113, 114] is loaded from the background gas for 10 s when the dispensers are turned on. Six laser beams from three orthogonal directions reduce the momentum of the atoms by

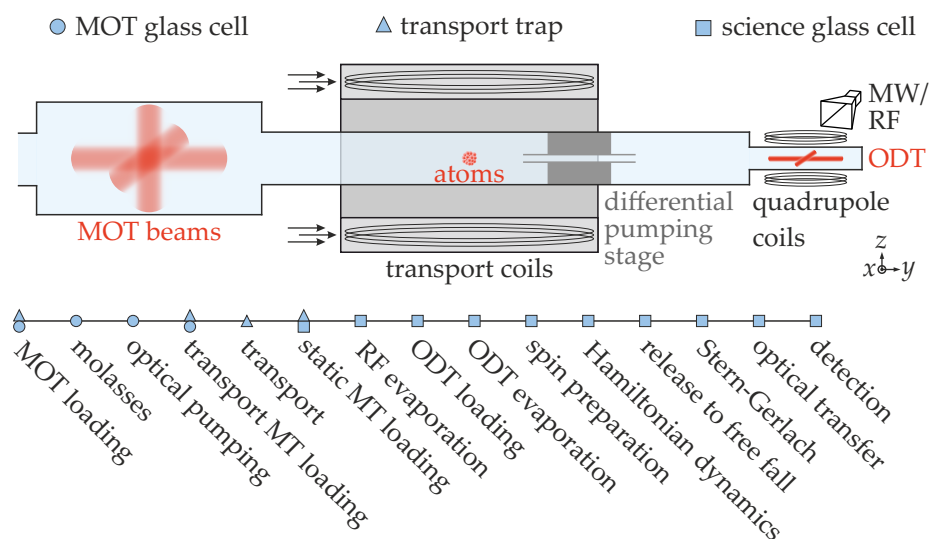


Figure 4.1: Experimental sequence for generation of BECs. The locations of different experimental stages are presented in the schematic drawing of our apparatus. The main steps are shown on a time line at the bottom. Circles, triangles and squares indicate the location of a step in the MOT glass cell, the transport trap or the science glass cell, respectively.

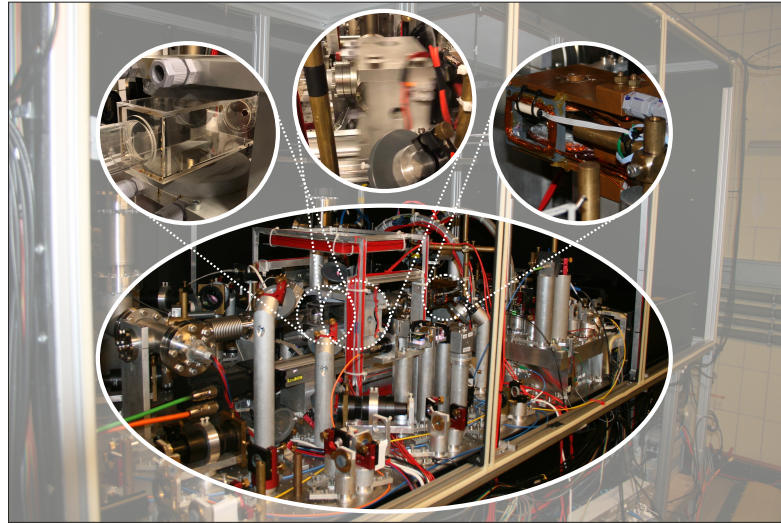


Figure 4.2: Experimental apparatus. The large figure displays the experimental apparatus. Small insets show the most important steps in the BEC generation sequence, i.e., the MOT cell, the moving transport trap and the science cell from left to right. In the picture of the science cell, the magnetic field sensor (white cylinder) is clearly visible very close to the atoms. The laser table generating the necessary frequencies for the experiments is not shown. One can only catch a glimpse of the colored fibers coming from the laser table and reaching the experimental table.

spontaneous laser force, i.e., the atoms absorb a photon from one laser beam and emit it isotropically. Because the absorption of the photon is directed and the emission is random in any direction, a net force arises that moves the atoms in the direction of the laser beam (Figure 4.3 a). The laser frequency is detuned in a way such that it only affects atoms moving toward the laser beam, i.e., red-detuned. As the spontaneous laser force only cools the atoms, but does not trap them, a magnetic field in anti-Helmholtz configuration (with zero magnetic field in the center) and clever polarization of the laser beams are necessary (Figure 4.3 b). This field changes the internal structure of the atoms in a way that the laser beams are only resonant to atoms moving away from the center and therefore a restoring force acts on the atoms. In this way, about 10^9 atoms can be loaded (Figure 4.3 c).

After a short molasses phase of 5 ms to further cool the atoms [115], a magnetic field is turned on again for 300 ms to trap the atoms. To trap as many atoms as possible, the atoms are beforehand optically pumped to the $|2, 2\rangle$ state that is magnetically trappable. The coils generating the magnetic trapping field are mounted on a translation stage that moves the trapped atoms from the MOT glass cell through a differential pumping stage into a region with even better vacuum (10^{-11} mbar) [116]. The transport takes 1.3 s and induces only negligible atoms loss.

In the science glass cell, the atoms are first reloaded from the magnetic transport trap into a static magnetic quadrupole trap where rf-induced evaporation [5, 117] takes place for 6 s to cool the atoms closer to quantum degeneracy. This technique is visualized in Figure 4.3 d). The magnetic trap causes a shift of energy levels proportional to the field strength and

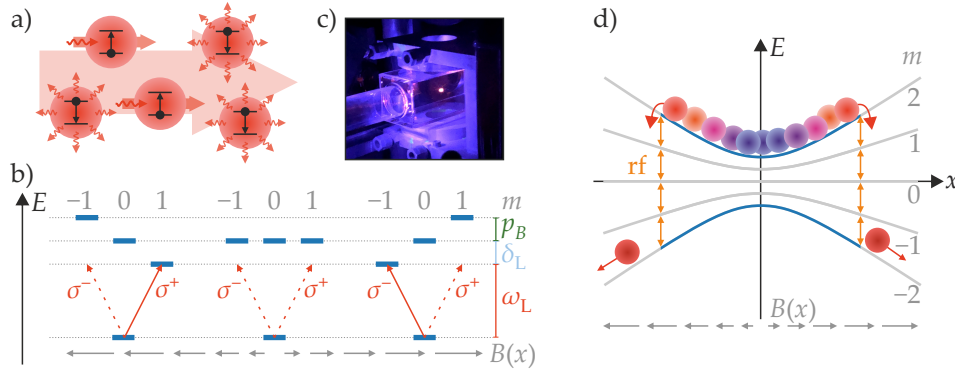


Figure 4.3: Schematic of a MOT and rf evaporation. (a) Absorption of a photon causes momentum in the direction of the laser beam (going to the right). Spontaneous emission, on the other hand, leads to momentum in a random direction. This results in a net force on the atoms to the right direction (background). Only atoms going toward the laser beam are in resonance and therefore decelerated. (b) An additional magnetic field shifts the resonances of magnetic sublevels due to the linear Zeeman shift p_B . For atoms in the trap center ($B = 0$), the lasers with frequency ω_L and detuning δ_L are out of resonance with any transition. At a certain distance from the center, however, a σ^+ polarized laser beam from the left (σ^- polarized from the right) drives a resonant transition to $m = +1$ ($m = -1$). This absorption and the following emission slow the atoms down as presented in (a). (c) Picture of a MOT (red cloud). The violet color stems from the light-induced atomic desorption. (d) Schematic of rf evaporation, where for simplicity only $m = \pm 2$ are taken into account. Atoms in the upper state are magnetically trapped. The hottest atoms (red disks) have highest probability of being far off the center. Different Zeeman states are coupled by rf signals (orange) that are resonant to atoms at certain distance to the center due to the Zeeman shift. Transferred atoms are not trapped any more and leave the trap while rethermalization reduces the temperature of the remaining atoms.

depending on the magnetic sublevel m . Hot atoms spend time in regions away from the center, where rf radiation brings them to states that are not trapped. The rf is gradually lowered to remove the hottest atoms from the trap and enable rethermalization.

The final trap is a crossed-beam optical dipole trap (ODT) where two laser beams in the horizontal directions create an attractive potential in the intensity maximum [6]. Within 1.1 s, the atoms are loaded into the ODT by ramping down the magnetic field and ramping up the power of the laser beams. The beams have approximate waists $w_x = 32 \mu\text{m}$ and $w_y = 60 \mu\text{m}$. Further evaporative cooling [118] takes place by ramping down the optical potential in this trap for 800 ms to about $P_x = 22 \text{ mW}$ and $P_y = 60 \text{ mW}$. Eventually, the ODT power is increased again to 60 mW and 250 mW, respectively, to guarantee a tight confinement that is beneficial for spin dynamics [119]. Resulting trapping frequencies are on the order of $2\pi \cdot 130$ to $2\pi \cdot 260 \text{ Hz}$. This dipole trap facilitates a spinor BEC as the spin is still an accessible degree of freedom. It contains up to $N = 130\,000$ atoms without a large thermal fraction.

A homogeneous magnetic field of about 0.95 G in the horizontal direction gives rise to a quantization axis for the atoms. Because Zeeman states arise, the atoms can have a defined and adjustable spin. The quantization field is actively stabilized with residual fluctuations of $50 \mu\text{G}$ and compensation coils in the orthogonal directions ensure low magnetic fields in directions orthogonal to the quantization axis.

The next short step employs three mw pulses to prepare the atoms from the initial $|2, 2\rangle$ state into the $|1, 0\rangle$ state that is in general the starting point of our experiments. Between the pulses, unwanted leftover atoms are removed by further mw radiation and resonant laser light.

Following, the atoms can be manipulated by electromagnetic radiation to implement various Hamiltonian evolutions. To this end, mw and rf antennas couple defined signals into free space toward the atoms. This is considered the main experimental stage where we will also investigate the phase diagram of a ferromagnetic spin-1 condensate in Chapter 6.

Finally, the atoms are released from the dipole trap into free fall and a strong magnetic-field gradient for 5 ms separates the different spin states from each other, comparable with the famous Stern-Gerlach experiment [120]. For the absorption detection, in detail described in Lücke [121], resonant light pulses are employed to take three pictures of the experimental region of interest. A background image and a beam image are used to estimate the atom numbers in the different spin states from a reduced intensity of the detection beam in an image including the atoms. Such an absorption detection method performs number counting with a detection noise of about 20 atoms.

Our absorption detection light is resonant to the $F = 2$ hyperfine manifold only. Hence, we have to transfer the $F = 1$ atoms for detection beforehand by laser radiation. Our detection captures five different masks that may contain

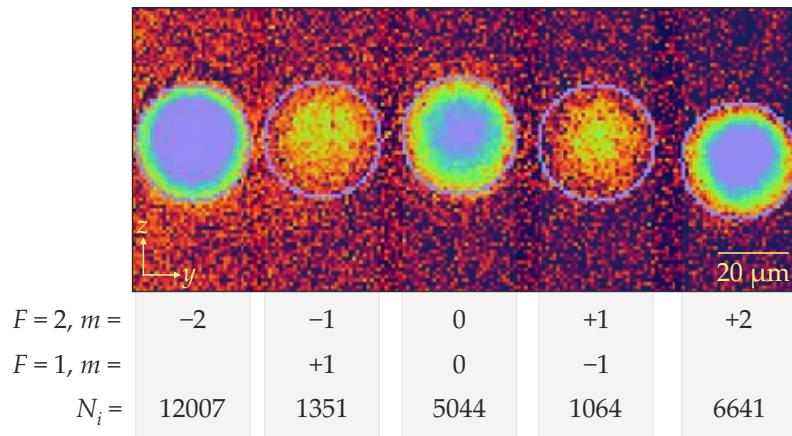


Figure 4.4: Typical absorption detection image. This image shows the atomic population distribution after an arbitrary Hamiltonian evolution. The different Zeeman states possess different atom numbers, as it can be seen in the lower part. This detection per se does not distinguish between $F = 1$ and $F = 2$. Therefore, the experimentalist has to ensure which hyperfine state is populated.

the eight different Zeeman states, i.e., the $|F = 1, m \in \{1, 0, -1\}\rangle$ and the $|F = 2, m \in \{-2, -1, 0, 1, 2\}\rangle$ states simultaneously (Figure 4.4). In principle, it would also be possible to independently detect $F = 1$ and $F = 2$ by taking an additional image before the detection transfer pulse, but this could cause additional detection noise [77]. The resulting atomic distribution presents the main data we retrieve from the experiments.

In the following sections, some important parts of the experiment are discussed in more detail.

4.2 MAGNETIC FIELD FLUCTUATIONS

Magnetic field fluctuations can be a major limitation for experiments in quantum many-body physics or entanglement-enhanced atom interferometry because it is sometimes unavoidable to utilize magnetically sensitive states. Variations in the magnetic field ΔB directly lead to a change in the energy levels by the linear and quadratic Zeeman shifts and therefore to a detuning from the adjusted frequencies.

Considering the transition between $|0\rangle$ and $|g\rangle$, the linear Zeeman effect causes an additional phase

$$\Delta\phi = b_p T_{\text{ev}} \Delta B \quad (4.1)$$

over the evolution time T_{ev} with $b_p \approx -702 \text{ kHz/G}$. In general, this is unfortunately not a constant shift, but fluctuations in the magnetic field lead to a varying phase from shot to shot. For interferometry, where a quantity is inferred from a phase measurement, this is detrimental.

The quadratic Zeeman shift, on the other hand, is smaller than the linear effect by four orders of magnitude for a magnetic field of 1 G. Nevertheless, it has consequences, because the precisely adjusted value of the QZE varies with magnetic field fluctuations. This causes imperfections in the prepared state and the intended dynamics.

The magnetic field fluctuations should thus be reduced as much as possible. In the experiment, a pair of coils in Helmholtz configuration generates the homogeneous quantization field that lifts the degeneracy in the hyperfine manifolds. The magnetic field generated by those coils is actively stabilized using a magnetic field sensor. A detailed description of this stabilization can be found in Quensen [122].

Because the sensor only measures in one axis, additional magnetic fields in other directions deteriorate the efficiency of the stabilization because the sensor is blind to these signals. To reduce this effect, two large compensation coils are implemented in the orthogonal directions. When a proper current is adjusted, the orthogonal fields vanish, which leads to a minimized total magnetic field. A measurement of the compensation currents is presented in Figure 4.5. The proper compensation currents are signaled by minimum total magnetic field and therefore minimum resonance frequency for the $|2, 2\rangle \leftrightarrow |1, 1\rangle$ transition, which is threefold sensitive to magnetic fields. Resonance frequencies for this transition are repeatedly determined for different currents and the compensation current is extracted from a fit.

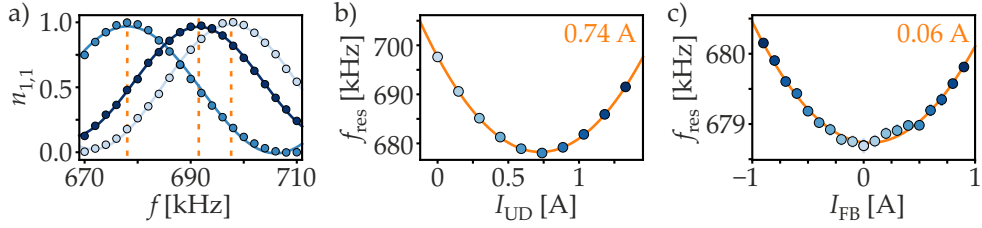


Figure 4.5: Determination of magnetic-field compensation currents. (a) Frequency spectroscopies ($f_{mw} = 6836 \text{ MHz} + f$) are performed on the $|2, 2\rangle \leftrightarrow |1, 1\rangle$ transition with different currents through the compensation coils. Presented measurements correspond to compensation currents $I_{UD} \in \{0, 0.75, 1.35\}$ A (from light to dark blue) in the up-down compensation field, corresponding to data points in (b). Orange dashed lines indicate the resonance frequencies. (b-c) From many spectroscopy measurements, where the resonance frequencies are extracted, the compensation currents of the up-down and front-back directions are determined by parabolic fits.

Using the Breit-Rabi formula (Equation 2.47), the resonance frequency of a spectroscopy measurement can be converted into an absolute magnetic field. The minimum transition frequency of the measurements presented in Figure 4.5, $f_{res} = 6836.678 \text{ MHz}$, e.g., corresponds to a detuning compared to the hyperfine energy splitting (Equation 2.46) of $\delta \approx 2\pi \cdot 2 \text{ MHz}$ and therefore $B \approx 0.95 \text{ G}$.

The fluctuations of the magnetic field can be measured using a detuned Ramsey sequence (Figure 4.6 a), where it is assumed that fluctuations of the mw frequency and intensity are negligible compared to magnetic field deviations. The detuning δ of the first $\pi/2$ pulse is adjusted in a way that the accumulated phase is $\phi = \delta T_{ev} \approx \pi/2$ and therefore a second $\pi/2$ pulse leaves the atoms in a 50/50 superposition, known as mid-fringe position (Figure 4.6 b). From the fluctuations in the transferred fraction $n_{1,-1} = N_{1,-1}/(N_{1,-1} + N_{2,2})$, we can directly infer the deviation from the expected magnetic field. To this end, the dependency of the transferred fraction n of a Ramsey sequence on the detuning δ and the evolution time T_{ev} is employed [123],

$$n(\delta, T_{ev}) = 4 \frac{\Omega_{mw}^2}{\tilde{\Omega}_{mw}^2} \sin\left(\pi \frac{\tilde{\Omega}_{mw}}{4\Omega_{mw}}\right)^2 \left[\cos\left(\pi \frac{\tilde{\Omega}_{mw}}{4\Omega_{mw}}\right) \cos\left(\frac{\delta T_{ev}}{2}\right) - \frac{\delta}{\tilde{\Omega}_{mw}} \sin\left(\pi \frac{\tilde{\Omega}_{mw}}{4\Omega_{mw}}\right) \sin\left(\frac{\delta T_{ev}}{2}\right) \right]^2 \quad (4.2)$$

with the generalized Rabi frequency $\tilde{\Omega}_{mw} = \sqrt{\Omega_{mw}^2 + \delta^2}$. The magnetic field is then obtained from the detuning using $\Delta B = \delta/(6\pi b_p)$ where a factor of 3 comes from the threefold sensitivity of the $|2, 2\rangle \leftrightarrow |1, 1\rangle$ transition. A value for the shot-to-shot magnetic field fluctuations is then given as the standard deviation of many measurement runs.

Figure 4.6 c) shows three such measurement results that also correspond to an improvement over time. Some smaller advancement was achieved by adjustment of the stabilization parameters, proper grounding of the components and cable routing far from rf components. A large contribution toward

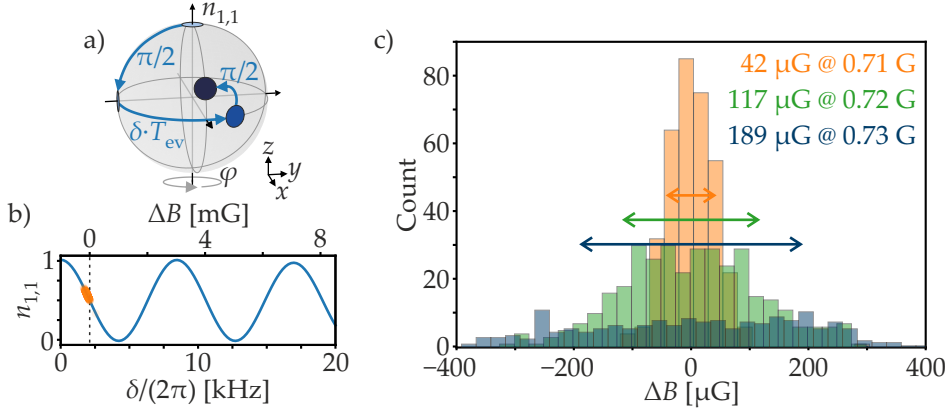


Figure 4.6: Magnetic field measurement by a Ramsey sequence. (a) Schematic illustration of a Ramsey sequence on a Bloch sphere. The evolution time T_{ev} and the detuning δ cause a phase evolution about the z axis. (b) The analytical formula of such a sequence (blue line) is shown for $T_{ev} = 100 \mu\text{s}$ and $\Omega_{mw} = 100 \text{ kHz}$. Orange dots correspond to a measurement of the transferred fraction $n_{1,1}$ with adjusted detuning of 2.1 kHz for mid-fringe position (dashed line). (c) Histograms of three different measurement runs with 350 repetitions each. The orange data corresponds to the values in (b). Absolute values of the magnetic fields are extracted from independent measurements and fluctuations are given as the standard deviation of the underlying data set.

residual magnetic field fluctuations of $80 \mu\text{G}$ was a thorough determination of the compensation currents (see above). The major improvement down to $50 \mu\text{G}$, in the end, was a replacement of the magnetic field sensor. Instead of a *Bartington Mag-03IE* with a range of $\pm 5 \text{ G}$ and 2 V/G gain, the new sensor has $\pm 1 \text{ G}$ range and 10 V/G gain. This limits the experiments to magnetic fields below 1 G , but also increases the sensitivity. Moreover, this sensor was placed even closer to the atoms than before.

4.3 MICROWAVE AND RADIO FREQUENCY COUPLING

The mw system employed for the measurement of ESQPTs is the one presented in Lücke [121] and a frequency synthesizer *Marconi 2025* provides rf signals. For this project, coherent states have to be created with defined population distribution and phase among the spin states. As the spin-1 system in $F = 1$ is considered, rf pulses will adjust the relative population between $|0\rangle$ and $|g\rangle$ and a detuned mw pulse imprints a relative phase (Section 2.2.3).

A resonant rf pulse of variable duration τ and Rabi frequency Ω_{rf} transfers a fraction of atoms from the initial state $|0\rangle$ into the symmetric superposition $|g\rangle$, such that a relative population $n_0 = \cos(\Omega_{rf} \tau/2)^2$ remains in $|0\rangle$. On the Bloch sphere, this rf pulse corresponds to a rotation about a horizontal axis by $\cos(\theta) = 2n_0 - 1$. The frequency of the rf pulse has to be adjusted very precisely, because detuning will lead to an additional, time-dependent phase during the evolution that could deteriorate our interferometric phase measurements. To this end, we employ a standard Rabi spectroscopy for a coarse estimation and a Ramsey spectroscopy to precisely determine the

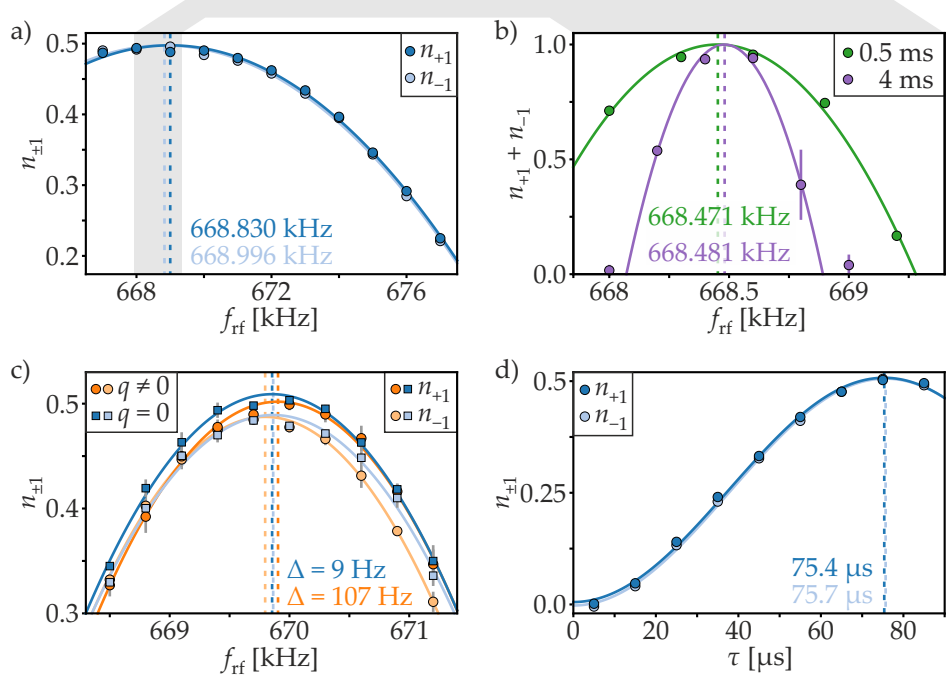


Figure 4.7: Radio frequency calibration. Dots correspond to measured data and solid lines represent fits to extract frequencies (a-c) or duration (d). (a) Standard Rabi spectroscopy. The transferred fraction is measured for a variation of the rf and initially all atoms in $|0\rangle$. Dark blue indicates the transfer to $|+1\rangle$ and light blue to $| -1\rangle$. Dashed lines and text indicate the obtained resonance frequencies that differ by more than 100 Hz. (b) Ramsey spectroscopy. The combined transfer to $|+1\rangle$ and $| -1\rangle$ is measured for a variation of the rf. In contrast to (a), the π transfer pulse is replaced by two $\pi/2$ pulses with an evolution time of 0.5 ms (green) and 4 ms (purple) in between. Note the narrow frequency range, as indicated by the gray area. The obtained resonance frequencies only differ by 10 Hz. (c) Spectroscopy depending on the QZE. With a compensated QZE (blue), the transfer to $|+1\rangle$ and $| -1\rangle$ is nearly equal, while a small shift to $q/|\Omega| = -1.9$ already causes the resonance frequencies to deviate. Dashed lines indicate the different resonance frequencies obtained from fits. (d) Rabi oscillation. A variation of the pulse duration τ transfers a variable portion of atoms to $|\pm 1\rangle$. The π pulse duration differs only slightly for the two modes (dashed lines and text).

resonance frequency. In contrast to a Rabi spectroscopy, i.e., a variation of frequency close to a π pulse, the Ramsey method employs two $\pi/2$ pulses with an evolution time in between. A large evolution time makes this method very sensitive to small detuning from resonance (Figure 4.7 a-b).

Moreover, we perform the spectroscopy at an adjusted QZE of $q/|\Omega| = 0$, because at this working point the signal is resonant to $| -1\rangle$ and $|+1\rangle$ simultaneously. In general, the energy differences from $|0\rangle$ to $| -1\rangle$ and to $|+1\rangle$ are not equal due to the quadratic Zeeman shift, leading to asymmetrical transfer (Figure 4.7 c). The dependency of the transferred fraction on the pulse duration can be obtained from a Rabi measurement (Figure 4.7 d), where the frequency is set to resonance.

Finally, the state preparation requires the implementation of a phase shift between $|0\rangle$ and $|g\rangle$. As explained in Section 2.2.3, a detuned mw

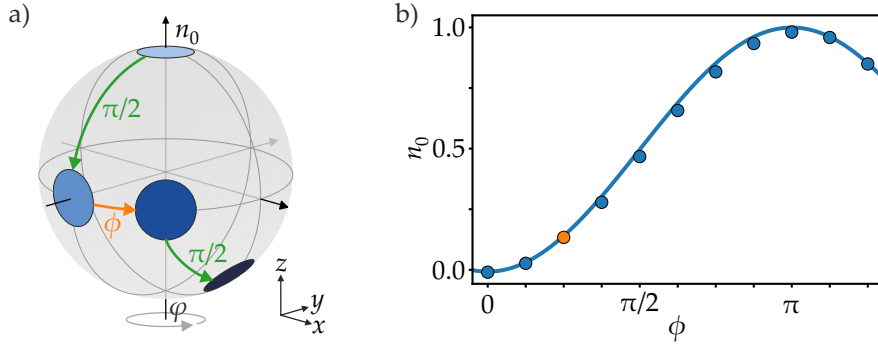


Figure 4.8: Microwave phase imprint. (a) Schematic representation of the measurement. The free evolution in a Ramsey sequence is replaced by an mw pulse (orange) that imprints a phase ϕ . On the Bloch sphere, this corresponds to a rotation of ϕ about the z axis. The $\pi/2$ pulses (green) are rf pulses that rotate about the x axis. (b) Measured fraction n_0 for different adjusted phases ϕ (dots). The solid blue line represents theory without free parameters. The orange dot indicates the phase imprint shown in (a).

pulse imprints a defined relative phase onto $|0\rangle$ and is adjusted such that no population is transferred. To experimentally prove this, we apply a resonant rf $\pi/2$ pulse onto $|0\rangle$, followed by a phase imprint ϕ , calculated from Equations 2.58 and 2.59, and a final rf $\pi/2$ pulse. For zero phase shift, we observe full transfer and in total, the experimental data follows the expected sine behavior $n_0 = \sin(\phi/2)^2$ (Figure 4.8).

4.4 CALIBRATION OF THE QUADRATIC ZEEMAN ENERGY

In addition to the relative population and phase, the QZE has to be adjusted for the preparation of excited states. This is done by mw dressing that contributes an energy q_{mw} to the total $q = q_B + q_{mw}$. The mw dressing is adjusted using a blue detuning from resonance of the transition $|1,0\rangle \leftrightarrow |2,0\rangle$ and thus shifts those energy levels closer to each other (Figure 4.9). In principle, the mw power can be employed for the dressing [100], but if only short quenches are required, the frequency can be adjusted easier from a technical perspective. In this work, the mw power is kept constant, such that only the dependency of the energy shift on the detuning has to be calibrated. Figure 4.10 presents the calibration method in detail. Note that we in general express q in terms of the spin dynamics strength $|\Omega|$. By an independent measurement of $|\Omega|$ (Section 4.5), the absolute value of q can nevertheless be determined.

The calibration of $q/|\Omega| = \pm 1$ (Figure 4.10 a-b) utilizes the fact that the dynamics for these QZEs should evolve fastest (Section 2.1.3). To extract f_1 , we initiate the atoms in $|0\rangle$ and apply a dressing field for a short amount of time. The dressing frequency causing the maximum transfer after this time then marks the point of $q/|\Omega| = 1$ which we call spin dynamics resonance. Retrieving f_{-1} is done using the same method, but starting with a symmetric superposition in $|\pm 1\rangle$.

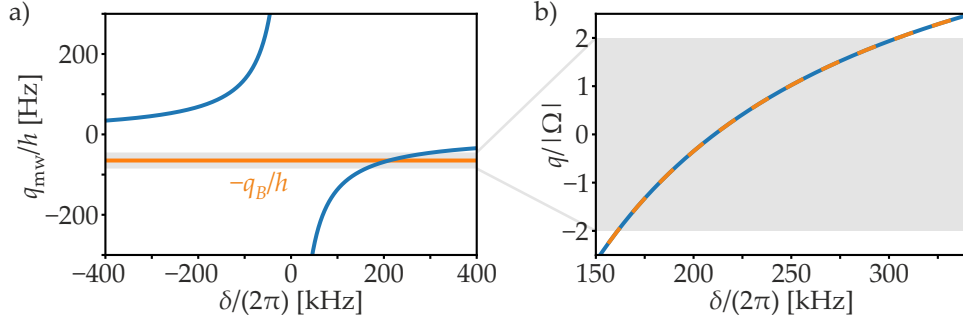


Figure 4.9: Energy shift due to mw dressing. (a) A detuned mw field shifts the energy levels of the $|1, 0\rangle \leftrightarrow |2, 0\rangle$ transition by q_{mw} . Blue detuning shifts the $|1, 0\rangle$ level upwards, which is an effectively negative Zeeman shift. Parameters of the simulation are $\Omega_{\text{mw}} = 46.5$ kHz, $|\Omega|/h = 10$ Hz and $B = 0.95$ G. For this magnetic field, the corresponding contribution to the quadratic Zeeman shift is $q_B/h = 65$ Hz. The point where the negative of this shift (orange) and q_{mw} are crossing corresponds to $q = 0$. The region around this point with $|q/\Omega| < 2$ (gray area) is employed for calibration of the QZE. (b) An adjustment of the effective QZE $q = q_{\text{mw}} + q_B$ (blue-orange dashed line) can be done by the detuning of the mw field. The QZE is given in units of the spin dynamics strength $|\Omega|$.

Another remarkable behavior that can be employed in the calibration is found at $q/|\Omega| = 0$ (Figure 4.10 c). At this point, the mw dressing field cancels the quadratic Zeeman shift due to the magnetic field completely, such that $q_{\text{mw}} = -q_B$. In this configuration, an initial state $\frac{1}{\sqrt{2}}|0\rangle + \frac{1}{\sqrt{2}}|g\rangle$ would remain stationary, as the energy levels would be degenerate. If, however, $q/|\Omega| \gtrsim 0$, the atoms would tend to populate $|g\rangle$, while for $q/|\Omega| \lesssim 0$, the state $|0\rangle$ is favorable.¹

The combination of all three pairs of values ($f_{q/|\Omega|}, q/|\Omega|$) can now be employed to obtain the dependency of $q/|\Omega|$ on the dressing frequency, as presented in Figure 4.10 d). This calibration yields

$$\frac{q}{|\Omega|}(\delta) = -\frac{1353(89)}{\delta} + 6.49(43). \quad (4.3)$$

For earlier experiments, we also calibrated $q/|\Omega| = \pm 2$ that utilizes features of the ground-state quantum phases [100]. The ground-state order parameter states that $|0\rangle$ is the ground state for $q/|\Omega| > 2$. Now all of the atoms are prepared in $|0\rangle$ and the dressing frequency is scanned. For values $q/|\Omega| > 2$, the atoms are expected to remain in $|0\rangle$, as this is the lowest-energy state. Once $q/|\Omega| = 2$ is reached, atoms should start to populate the symmetric state $|g\rangle$. The value of the dressing frequency at which this population starts to arise then defines the frequency f_2 to adjust for $q/|\Omega| = 2$.

¹ Interestingly, this is the opposite behavior as described in Luo et al. [99] (Supplemental Material), where the fraction in the side modes decreases for $q/|\Omega| \gtrsim 0$ and increases for $q/|\Omega| \lesssim 0$. This is attributed to a different relative phase φ between $|0\rangle$ and $|g\rangle$. In our case, we expect to be on the side of the Bloch sphere (P' phase, $\varphi = -\pi/2$). For an initial phase of $\varphi = 0$, i.e., in the BA' phase, one would expect to be on the stationary point with $n_0 = 0.5$ and $q/|\Omega| = 0$. This would result in the dynamics presented in Luo et al. [99]. For the determination of the frequency f_0 , there is no difference between the methods.

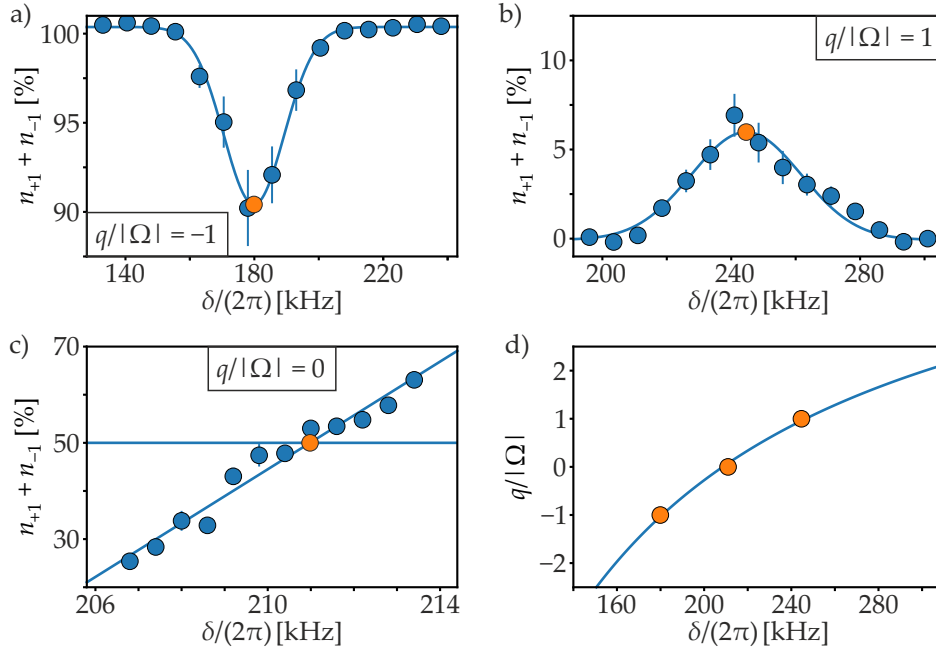


Figure 4.10: Calibration of the QZE. (a-c) The calibration methods to extract the corresponding frequencies are explained in the main text. Blue dots correspond to measurement data and orange dots to the frequencies f_i obtained from the fits (blue lines). The mean atom number is in this case $N = 60\,000$. Spin dynamics durations are 50 ms for $q/|\Omega| = \pm 1$ and 25 ms for $q/|\Omega| = 0$. The resonance frequency is measured to be 6834.683 MHz. (d) The dependency of q on the adjusted detuning is obtained by a fit (blue line) to the three calibration frequencies (orange dots).

For f_{-2} , the same method can be employed by starting with all the atoms in a superposition of $|+1\rangle$ and $|-1\rangle$ and looking for initial transfer to $|0\rangle$.

This calibration at $q/|\Omega| = \pm 2$, however, is difficult to evaluate because the start of the initial dynamics cannot be determined with high fidelity. The data set presented in Figure 4.10 also contains calibrations for $f_{\pm 2}$. Additionally using those data points for a five-point fit compared to the three-point method results in mean absolute deviations of $\Delta q = 0.07 |\Omega|$ for the relevant range of $|q/\Omega| \leq 2$. As the determination of $q/|\Omega| = 0$ and $q/|\Omega| = \pm 1$ employs clear features that can be fitted well, the calibration is done using the three-point method throughout this work. This method might be more reliable or at least saves time compared to the calibration of five points.

Finally, the stability of the QZE is tested. To this end, a calibration of f_1 is running for 14 hours and the extracted parameters are subsequently analyzed over time (Figure 4.11 a-c). The spin dynamics resonance scan at $q/|\Omega| = 1$ is chosen for this analysis because it has the most trustworthy fit. Fluctuations in the maximum transfer are on the order of 1.5% and the resonance frequency seems to drift by about 5 kHz over 12 hours. For the case of $q/|\Omega| = 1$, this corresponds to $\Delta q = 0.11 |\Omega|$.

To distinguish stability over time from stability over atom number (that fluctuates in time), the resonance frequencies and maximum transfers are

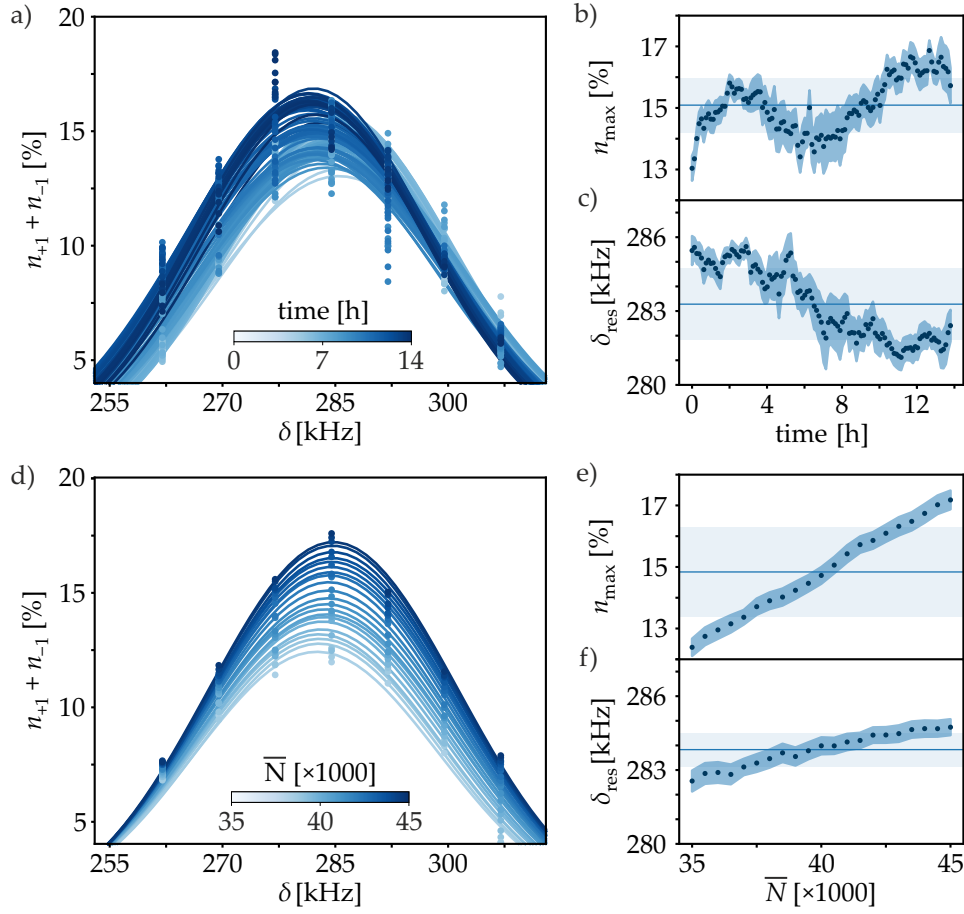


Figure 4.11: Fluctuations of the spin dynamics resonance frequency, depending on the measurement duration (a-c) and the number of employed atoms (d-f). The resonance frequency of $|1, 0\rangle \leftrightarrow |2, 0\rangle$ is $f_{\text{mw}} = 6834.683$ MHz. (a,d) The fraction of atoms being transferred to $|1, \pm 1\rangle$ (dots) is fitted by Gaussian fits. For (a-c), a rolling average over 30 cycles with each 18 experimental runs is taken. For (d-f), a post-selection on $\bar{N} \pm 5000$ atoms is taken for different values of \bar{N} . From Gaussian fits of the transferred atoms, the maximum transfer n_{max} (b,e) and the resonance frequency δ_{res} (c, f) are extracted. Uncertainties in the fit are depicted by the shaded blue areas.

also analyzed with respect to the atom number (Figure 4.11 d-f). It can be seen that there is a clear relation. This relation is to be expected because both the maximum transfer and the resonance frequency depend on Ω and Ω itself depends on the atom number. However, the analysis over time has been restricted to $N \in [38\,000, 42\,000]$ with mean values between 40 000 and 40 500, so that atom number fluctuations cannot explain the drifts in Figure 4.11 a-c). Moreover, the change in resonance frequency over time is larger than the one due to atom number variations.

The calibration of the QZE therefore indeed varies over time. Technical noise sources explaining this could be the magnetic field, the mw signals (phase/amplitude noise or varying antenna position) or fluctuations in $|\Omega|$ related to the optical dipole trap. Because we want to precisely adjust the

QZE for the preparation of excited states (Chapter 6.1), the small drift makes a frequent recalibration necessary.

4.5 SPIN DYNAMICS RATE

The spin dynamics rate Ω is a measure of the interaction strength for the spin-changing collisions. In this sense, Ω also defines the population oscillation periods T for the measurements of the interferometric order parameter later on. Because the population oscillation periods will be directly retrieved from Ω , a good estimation of this parameter is required. There exist different methods to measure this quantity that are presented in the following.

In Luo et al. [99] (Supplemental Material), the mw power is employed to create an energy shift q_{mw} . For zero mw power, the total energy shift q is defined only by the magnetic contribution q_B that can be calculated knowing the magnetic field. Next, they determine the mw dressing power $P_{q=0}$ in a similar fashion as we do it with f_0 (previous section). At this point, $q_{\text{mw}} = -q_B$. This defines a linear slope from which other total shifts q can be calculated knowing the mw power. Finally, the power for $q/|\Omega| = 2$ is measured analog to our determination of f_2 . Utilizing the determined slope, an absolute value of $q = 2|\Omega|$ is retrieved and $|\Omega|$ can be extracted. This method is not suitable for us, as we vary the mw frequency instead of the power and the energy shift is not linear in the frequency, but hyperbolic in the detuning.

Hoang et al. [69] employs also the analysis of $q/|\Omega| = 2$, but with a varying magnetic field instead of mw dressing. Hence, the absolute value of q only depends on the magnetic field, $q = q_B$. From the critical value of the magnetic field where $q = 2|\Omega|$, and therefore $|\Omega| = q_B/2$, they extract $|\Omega|$. This method is of course only possible for a variation of the magnetic field instead of the mw field which has the disadvantage of being restricted to positive values of $q/|\Omega|$.

For our earlier experiments $|\Omega|$ was routinely obtained by variation of the spin dynamics time at $q/|\Omega| = 1$ and fitting of the transferred fraction to the side modes by $N_g = 2 \sinh(\Omega t/\hbar)^2$ (Equation 2.28). The spin dynamics time has to be kept short to ensure the low-depletion limit. This method has the disadvantage of underestimating $|\Omega|$ because experimental noise and in particular atom number fluctuations would lead to a reduced spin dynamics rate, no matter if the numbers are fluctuating up or down [124]. Moreover, this method requires many experimental realizations for every data point to reliably determine mean values.

A very simple method employs just the spin dynamics resonance scan for $q/|\Omega| = 1$ to estimate $|\Omega|$ and is a reduction of the aforementioned method for a single spin dynamics duration τ_{SD} . Looking at the transfer to the side modes, the simple formula

$$|\Omega| = \operatorname{arcsinh} \left(\sqrt{\frac{1}{2} N_{g,\text{max}}} \right) \hbar / \tau_{\text{SD}} \quad (4.4)$$

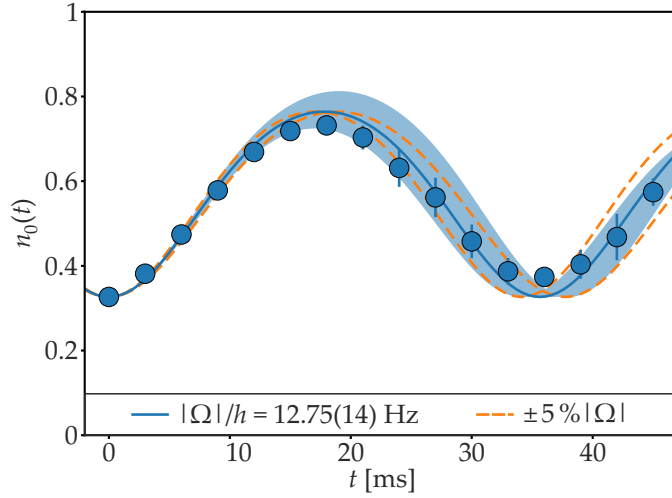


Figure 4.12: Determination of the spin dynamics rate $|\Omega|$. The measured fractional population is fitted to a theoretical model $n_0(t)$ that depends in particular on q and $|\Omega|$. The initial relative population is $n_0(0) = 0.323(4)$ and the initial phase is assumed to be $\varphi = 0$. A previous calibration of $q/|\Omega| = 1$ leaves only $|\Omega|$ as a fit parameter. The fitting of $|\Omega|$ (solid blue line) assumes a constant spin dynamics rate. For comparison, the fit $n_0(t)$ is shown with 5% deviation in Ω (orange dashed lines). The shaded area indicates fluctuations of 10% in $q/|\Omega|$.

directly gives the desired value. However, this method also underestimates the spin dynamics rate.

For this work, we utilize a method that is both quick and symmetric under technical fluctuations. This method employs the mean-field trajectories of excited states (Section 3.3.2), where the population oscillation only depends on the initial relative population n_0 , the relative phase φ and the QZE $q/|\Omega|$. We prepare an excited state, track the population oscillation and fit it by Equation 3.17, where the initial phase is experimentally set to $\varphi = 0$ and the initial relative population n_0 can be obtained by the first data point. To obtain a good fit, $q/|\Omega|$ should be known as precisely as possible. We thus perform these measurement at $q/|\Omega| = 1$ where the Gaussian fit of the spin dynamics resonance scan yields a reliable result. Figure 4.12 shows such a measurement. Only a few experimental realizations are required per data point. The initial population is chosen such that the corresponding trajectory is not in the vicinity of phase transitions or the poles because migrations to other trajectories could disturb the signal.

Finally, Ω is not a fixed parameter, but can be tuned. This can be beneficial for sensitive measurement because faster dynamics, i.e., larger $|\Omega|$ leads to less influence of magnetic field fluctuations. The rate at which the spin dynamics occurs is given by

$$\Omega = 2\lambda N = \frac{2}{3}(g_2 - g_0) N \int d^3r |\psi(\vec{r})|^4, \quad (4.5)$$

as described in Section 2.1.2. Assuming a three-dimensional harmonic trap and a Thomas-Fermi density profile, $\int d^3r |\psi(\vec{r})|^4 \propto N^{-3/5}$ [76, 109] and therefore $\Omega \propto N^{2/5}$. We can thus make the dynamics faster by utilizing

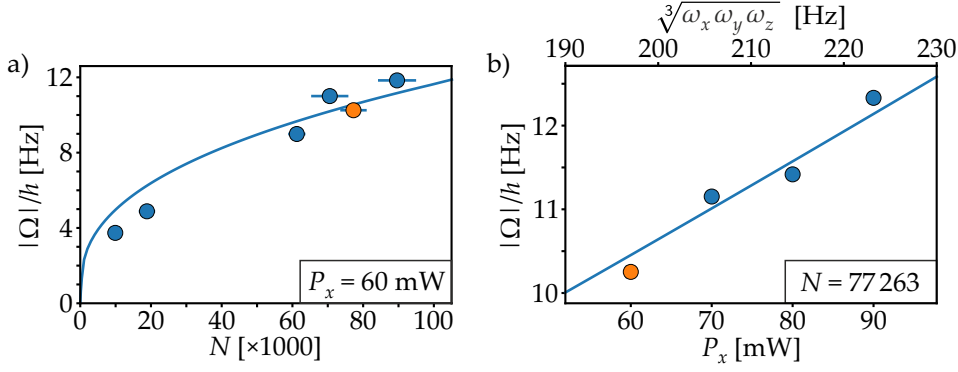


Figure 4.13: Tuning the spin dynamics rate by atom numbers and trapping frequencies. The total atom number (a) and the power of the dipole trap beam in x direction (b) are employed to vary the spin dynamics rate Ω . Dots present values of $|\Omega|$ extracted from several measurements. It should be said that these measurements used the old method of determining $|\Omega|$. Solid lines represent fits of $|\Omega| \propto N^{2/5}$ and $|\Omega| \propto \omega^{6/5}$ with $\omega = \sqrt[3]{\omega_x \omega_y \omega_z}$. Orange dots indicate the same measurement data.

more atoms for our experiments. To this end, we went from our normal working range of 10^4 atoms up to $7 \cdot 10^4$ atoms, thereby increasing $|\Omega|$ by roughly a factor of 2 (Figure 4.13 a). The increase of $|\Omega|$ by employing more atoms is, however, limited. At very high atom numbers, we observe a nonlinearity in the atom number estimation due to imperfections in the detection system [121].

Another way to increase $|\Omega|$ is the spatial wave function term $\int d^3r |\psi(\vec{r})|^4$ that depends also on the trapping frequencies of our optical dipole trap. Experimentally, we can relatively easy vary the trapping frequencies to some extent by adjusting the final power of the dipole trap laser beams. Different laser beam waists would also be possible, but present a bigger change to the experimental setup. At fixed beam waists of about $w_x = 32 \mu\text{m}$ and $w_y = 60 \mu\text{m}$, we vary the power as presented in Figure 4.13 b). For a spherical harmonic trap with trapping frequency ω , the spin dynamics strength scales with $\Omega \propto \omega^{6/5}$ [76]. We fit this relation to trapping frequencies calculated from the waists and adjusted powers. To this end, we employ the geometric mean $\sqrt[3]{\omega_x \omega_y \omega_z}$ of the trapping frequencies in three dimensions. In addition, the power in the second beam, P_y , can also be employed to increase the spin dynamics rate. Utilizing these control parameters, we achieve values $|\Omega|/h > 13$ Hz.

Note that increasing the atom number or tightening the dipole trap potential could ultimately break the single-mode approximation. Calculations for our experimental parameters, however, implied its validity [60].

VERSATILE AND LOW-NOISE INTERNAL STATE MANIPULATION

For ^{87}Rb and magnetic fields on the order of 1 G, the experimental tools for spin state manipulation are mw (\sim GHz) and rf (\sim kHz) radiation. As those electromagnetic signals compose the main interaction with the atoms, their versatility and noise characteristics are of high importance. This chapter presents a highly dynamical rf source that, in interplay with a low-noise mw synthesis chain, provides all required signals. Furthermore, advanced techniques for pulse manipulation, i.e., pulse shaping and composite pulses are presented. This setup was designed, constructed and implemented in the framework of this thesis and can be employed for future experiments, as for example discussed in Chapter 7. Parts of the results on the presented mw source are published in Meyer-Hoppe et al. [125].

5.1 OVERVIEW OF THE EXPERIMENTAL SETUP

The system for the generation of rf and mw signals is depicted in Figure 5.1. Commands are typed into a *LabView* interface on the experiment control computer, compiled and sent to a field-programmable gate array (FPGA) module *Kasli* [126] via remote procedure calls in every experimental run. In particular, this stage translates the chronologically given commands from *LabView* into a program that can be executed on the FPGA using the open-source control system *ARTIQ* [127]. A detailed description of the control software can be found in Baron [128] and the code itself is available online [129].

The direct digital synthesis (DDS) module *Urukul* [130] and a digital input/output controller *DIO_BNC* receive their commands from the FPGA. Those three components belong to the open-source hardware ecosystem *Sinara* [131] and are mounted in a single 19 inch rack. The program is structured in a way that individual command blocks are executed when a trigger from the main *LabView* program is received at an input port of the *DIO_BNC* module. In this way, the time basis of the entire experimental sequence, defined by *LabView*, is synchronized with the *ARTIQ* system.

The FPGA receives a 100 MHz clocking signal from an ultra-low-noise multiplied crystal oscillator *Wenzel MXO-PLD 501-28637* with 100 MHz and 7 GHz output. This oscillator is itself referenced to 10 MHz from a GPS-referenced and oven-controlled crystal oscillator in our institute to provide long-term stability.

The main component responsible for the versatile frequency generation is the DDS module *Urukul* that contains four *AD9910* [132] DDS chips. Every chip takes parameters for frequency, amplitude and phase offset and generates an analog signal from this input. The *Urukul* module moreover contains low-pass filters, variable attenuators, amplifiers and switches. An

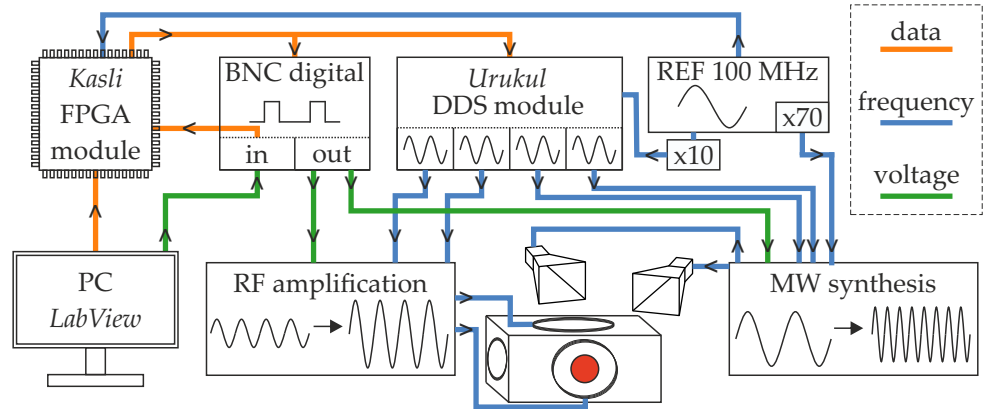


Figure 5.1: Sketch of the mw and rf generation. Data connections (orange) are employed to distribute the commands from and to the FPGA. The *DIO_BNC* module controls mw and rf switches and receives an input trigger from *LabView* (green voltage signals). Frequency signals are depicted in blue. Reference frequencies are all obtained from the 100 MHz oscillator and the *Urukul* module provides versatile frequency output for state-selective rf transfer and mw synthesis. Those signals interact in the end with the atoms, after being coupled to free space via self-built antennas.

internal clock distribution takes care of synchronizing the four DDS chips. In our case, the system clock is operated at 1 GHz. The clock reference can be obtained from an on-board oscillator, from the *Kasli* module via an internal connection or from an external source via front-panel connection. The respective clocking frequency and its source are specified in the software code.

The choice of reference for the DDS module is quite important, as Figure 5.2 a) shows. In this graph, different frequency sources are employed as a reference input for the *Urukul* and the phase noise of the DDS output is measured at an adjusted frequency of 165 MHz. Phase noise $\mathcal{L}(f)$ is connected to the one-sided spectral density $S_{\phi}(f) = 2\mathcal{L}(f)$ and measures the noise power relative to the carrier in a bandwidth of 1 Hz at offset frequencies f from the carrier [133, 134]. A very compact referencing method is to use the internal clock distribution of the *Kasli*. It generates 125 MHz from (in our case) 100 MHz input frequency using an *Si5324* clock multiplier and distributes it to MMCX output connectors within the rack. This includes a redundant multiplication to 125 MHz. The phase noise is therefore better when the *Urukul* is directly referenced to the 100 MHz that clock the *Kasli* via front-panel connection. The lowest phase noise is, however, achieved for a direct clocking method, where the 1 GHz system clock is directly obtained from a signal connected to the front panel. To this end, a tenfold multiplied signal from the 100 MHz *Wenzel* oscillator using a *Wenzel IFM-2-100-10-13-13*, a *Rohde & Schwarz SMB-B1H* and a *Mirny* mw synthesizer from the *Sinara* family are tested. The important range for our applications is 10 Hz to 100 kHz, as explained later in Section 5.2. In this range, the tenfold multiplied signal of the low-noise 100 MHz oscillator performs best. It is therefore chosen as reference for the DDS module.

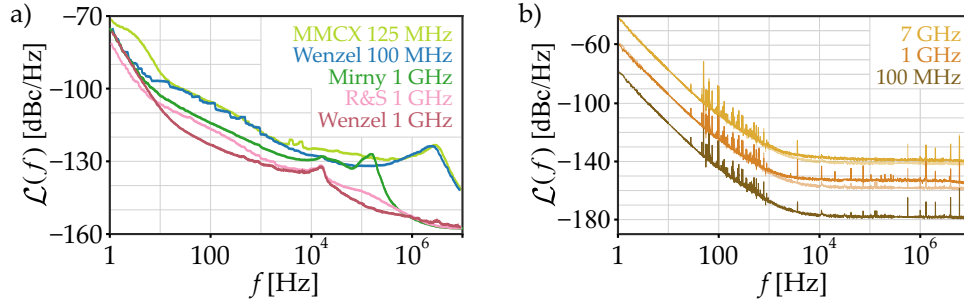


Figure 5.2: Phase noise of clocking methods and *Wenzel* oscillator multiplications. (a) Phase noise $\mathcal{L}(f)$ of the DDS output at 165 MHz is measured for different clock references of the *Urukul* module. Via internal multiplication in the *Kasli* and an MMXC connection, a 125 MHz signal is obtained (light green). The front-panel method is tested for 100 MHz from the *Wenzel* oscillator (blue) and 1 GHz from a *Mirny* mw synthesizer (green), a *Rohde & Schwarz SMB-B1H* frequency generator (pink) and multiplied 100 MHz (red). The raw data is smoothed for better visibility. (b) The 100 MHz signal of the *Wenzel* oscillator (brown) is internally multiplied to 7 GHz (yellow) and externally multiplied to 1 GHz (orange). Raw data is shown here as opaque curves. The transparent lines indicate fundamentally multiplied signals of the 100 MHz signal, i.e., a multiplication by 10 (20 dB) and 70 (36.9 dB).

Figure 5.2 b) characterizes the phase noise of the main reference frequencies obtained from the *Wenzel* oscillator. It shows the 100 MHz and 7 GHz outputs of the oscillator, the signal multiplied to 1 GHz and the theoretically achievable phase noise by fundamental multiplication of $\times 70$ and $\times 10$, respectively. The only major deviation of the measured signals from theory occurs for frequencies above 1 kHz, i.e., in the region of white noise. This seems reasonable as the multiplication steps also include amplification stages that introduce additional noise [133]. The mean deviation between theoretically achievable and measured phase noise is 2.36 dB and 4.53 dB with standard deviations of 0.80 dB and 1.38 dB for the 7 GHz and 1 GHz signal, respectively. For the integrated phase noise, these deviations are negligible.

Two of the *Urukul* outputs operate a state-selective rf transfer that is explained and analyzed in Section 5.3. The other two signals are fed into an mw synthesis that generates two independent signals for dressing and pulses. In the subsequent section, this synthesis is explained in detail.

5.2 MICROWAVE SYNTHESIS CHAIN

For the application in mw atomic clocks, sources with very low phase noise exist [135–138]. By design, however, they lack a fast dynamical adjustment. A successful technique to generate versatile frequencies in the mw range is the mixing of an mw signal close to the desired frequency with an adjustable rf signal. The mixing produces sidebands, from which one of them presents the desired signal. This process is implemented in many labs because it is very simple and the dynamic features are directly inherited from the rf source. Chen et al. [139] report on such a device using self-built filters, resulting in low phase noise and updates within 24 to 32 μs . Faster updates

of 4 μ s are stated in Morgenstern et al. [140] using an FPGA, but no phase noise characteristics is given. The device presented in this section combines ultra-low noise of the *Wenzel* oscillator with excellent dynamical features of the *Urukul* DDS module. Furthermore, the design is easy to reproduce because it does not rely on self-built components.

The setup of the constructed mw synthesis chain is presented in Figure 5.3. Two of the *Urukul* channels with frequencies of 165 ± 20 MHz are each mixed with the 7 GHz output of the *Wenzel* oscillator, resulting in two sidebands at 6835 ± 20 MHz and 7165 ± 20 MHz. This establishes two independently controllable paths for pulses and dressing. The dressing path contains a *Mini Circuits ZMX-8GLH* mixer and the pulse path a *Marki Microwave SSB-0618* single-sideband mixer. The latter causes additional suppression of the upper sideband by 17 dB. The carrier at 7 GHz and the upper sideband are subsequently filtered by a narrow bandpass filter *Wainwright WBCQV3-6585-6825-6845-7085-50TT* with a passband of 20 MHz around 6835 MHz. Particularly due to this filter and the DDS itself, the output power of the mw generation varies with the adjusted frequency by ± 0.2 dB for 6835 ± 5 MHz and ± 0.6 dB for 6835 ± 20 MHz. If necessary, this dependency can be calibrated in the *ARTIQ* software.

The final power amplifiers require an input power of 0 dB to give out the maximum possible power. Because the signal is below that threshold in front of the amplifier, pre-amplifiers *Mini Circuits ZX60-83LN-S+* increase the signals in advance. The final amplification stage is different in the two paths. While the dressing path includes a *Kuhne KU PA 640720-10 A* amplifier with maximum output of 10 W, the pulse path contains a *Microwave Amps AM43* with 40 W for very short pulse durations. The *Urukul* DDS module already incorporates a switch, such that the signal after the amplifier can be turned off. This switch, however, just attenuates the signal by 70 dB. Therefore, additional mw switches *Mini Circuits ZFSWA2-63DR+* reduce this attenuation further. Isolators prevent unwanted reflections from coupling back into components after the 7 GHz output and the pre-amplifiers (*Pasternack PE8402*) and after the power amplifiers (*MCLI CS-5*). A detailed component list is provided online [141].

Power amplifiers are nonlinear components that amplify the input linearly only in a certain power range. Frequency mixers show this characteristic as well. For an input power at the so-called 1 dB compression point, the output power after a nonlinear component is 1 dB lower than the expectation from a linear slope. Using such powers, undesired higher orders occur, while the fundamental signal is compressed. High output power is beneficial to reduce pulse durations and therefore possible coupling to noise sources, but for clean and continuous operation, it is relevant to stay in the linear regime. To determine the linear range, the input power of the synthesis chain is varied by the internal *Urukul* attenuation and the resulting output power is measured. Because for maximum power of the *Urukul* the saturated range already spans more than 15 dB, fixed attenuators of 10 dB are placed after the *Urukul* outputs, i.e., in front of the mixers. Moreover, 3 dB attenuators are employed in front of the power amplifiers to reduce the input power

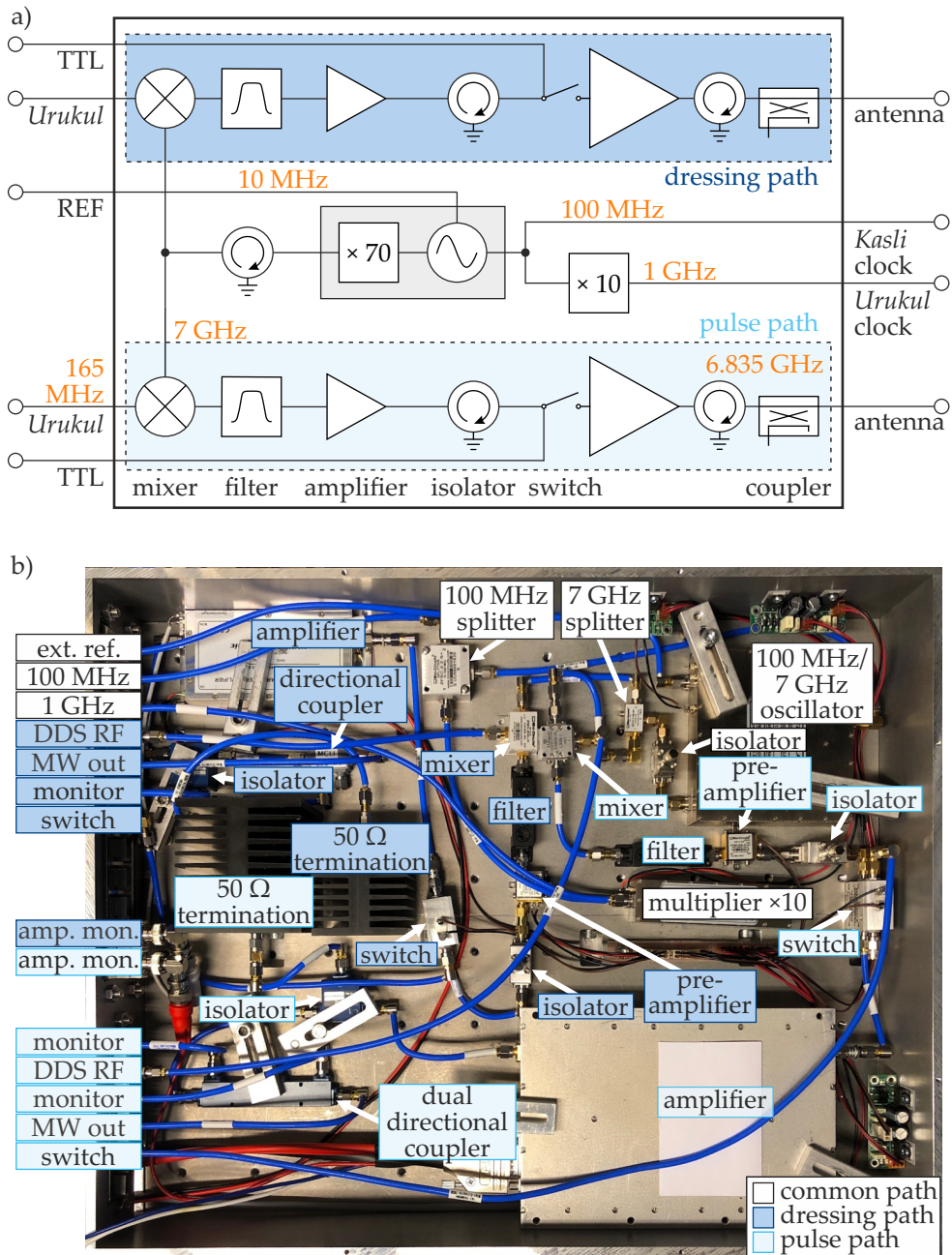


Figure 5.3: Setup for mw frequency synthesis. (a) Schematic overview of the mw generation. Everything inside the large black square is included in a water-cooled box and presented in (b). Inputs are on the left side of the square and outputs on the right. The dressing path (dark blue) and the pulse path (light blue) are equal from a schematic point of view. The Wenzel oscillator is depicted in gray and frequency values at different stages are indicated in orange. (b) Picture of the constructed device. Components are labelled with rectangles in white (common path), dark blue (dressing path) and light blue (pulse path). Inputs and outputs are indicated on the left side.

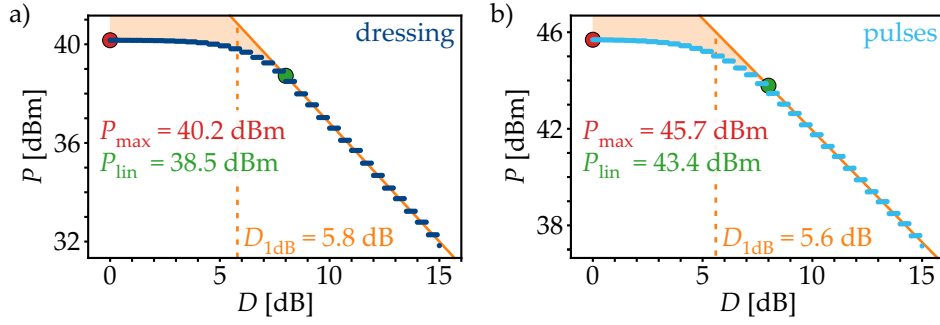


Figure 5.4: Nonlinearity in the output power. The nonlinear behavior of the synthesis chain is shown with the internal *Urukul* attenuation D as the varied parameter and the output power P after the amplifier as the measure. Graph (a) shows the behavior of the dressing path and (b) presents the results for the pulse path. Note that the *Urukul* power is already attenuated by a fixed attenuator of 10 dB in front of the mixer and another 3 dB attenuator is placed in front of the power amplifiers. The measured data (small blue dots) is fitted in the linear range (solid orange line). From this fit, the 1 dB compression values $D_{1\text{dB}}$ are extracted. Large red dots indicate maximum power values P_{max} obtained in this measurement and large green dots the power at the start of the linear range P_{lin} at $D = 8$ dB. The output power was obtained after directional couplers with -20 dB and -30 dB for the dressing and pulse path, respectively, and a measured cable insertion loss of 1.83 dB is also included in the scale.

coming from the pre-amplifiers. Figure 5.4 shows the remaining nonlinear behavior of the mw generation. A high-power regime can be obtained by no adjusted attenuation of the *Urukul* with output powers of 40.2 dBm (10.5 W) and 45.7 dBm (37.2 W) for the dressing and pulse amplifier, respectively. At an attenuation of 8 dB, the linear regime starts with powers of 38.5 dBm (7.1 W) for the dressing and 43.4 dBm (21.9 W) for the pulse amplifier.

The spectrum for the high-power case is shown in Figure 5.5, where the rf has been set to 165 MHz. In the graph with 500 MHz frequency span, the local oscillator frequency at 7 GHz and the upper sideband are clearly visible, but suppressed by 80 dB and 70 dB for the dressing path and 70 dB and 88 dB for the pulse path, respectively. The different suppression can be attributed to the different mixers in the two paths. The relevant region of $6\,835 \pm 5$ MHz (Figure 5.5 b) shows clear peaks of the desired frequency with a background suppressed by at least 80 dB. Note that the linear regime is expected to have even less background signals and that the high-power spectrum is an upper estimate of the residual signals.

In atom interferometry experiments, a quantity is estimated by a phase measurement. Therefore, phase noise of the mw signal is an important parameter to consider [142]. The phase noise should be small within the interferometric sequence, in our setup limited to durations of 100 ms. This corresponds to a lower frequency bound of 10 Hz. Moreover, phase noise faster than the duration of a single pulse (10 μ s) is averaged out, i.e., with frequencies greater than 100 kHz. These assumptions are only a rough estimate, but they define a region of interest for the phase noise. For certain interferometry configurations, a transfer function can be designed to see

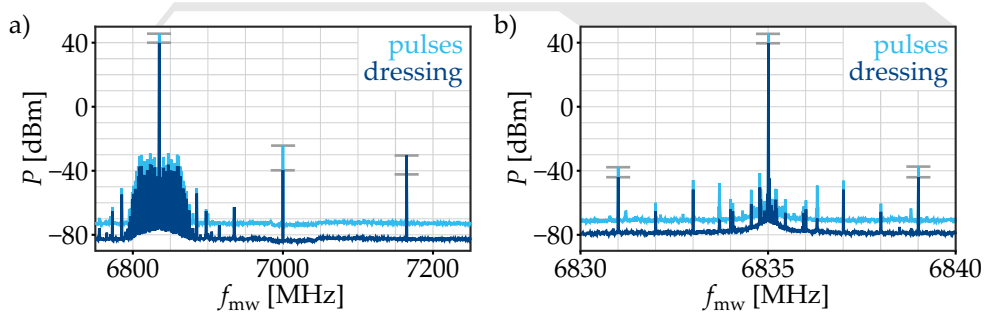


Figure 5.5: Spectrum of the mw signal at 6.835 GHz for dressing and pulse path. (a) The spectrum is measured with a center frequency of 7 GHz and 500 MHz span. Maximum powers P at $f_{mw} = 6.835$ GHz are 43.4 dBm and 38.5 dBm for the pulse (light blue) and dressing path (dark blue), respectively. Both paths show similar spectral features, in particular residual signals at 7 GHz and 7.165 GHz. Those signals are, however, suppressed by more than 70 dB compared to the main peak. (b) Detailed spectrum with a span of 10 MHz around to the carrier frequency. Background signals are more than 80 dB lower than the carrier.

the actual effect of noise at certain frequencies [143]. To achieve maximum possible phase resolution, the technical phase noise has to be below the fundamental Heisenberg limit, $\sigma_\phi < 2\pi/N$. We therefore require an integrated phase noise of $\sigma_\phi \approx 600 \mu\text{rad}$ for typical atom numbers of $N = 10^4$ in the frequency range from 10 Hz up to 100 kHz. Figure 5.6 a) shows the phase noise of the dressing path and important components. It can be directly seen that the phase noise is limited by the Wenzel oscillator's 7 GHz for all offset frequencies expect for a small region around 16 kHz, where the DDS noise dominates. The resulting integrated phase noise $\sigma_\phi = \sqrt{2 \int \mathcal{L}(f) df}$ evaluates to $\sigma_\phi = 483 \mu\text{rad}$ for the dressing path. Phase noise of the pulse path looks almost identical with an integrated phase noise of $\sigma_\phi = 498 \mu\text{rad}$. This low noise is only achievable because the DDS noise is very low due to the direct clocking method at 1 GHz (Figure 5.2). For the front-panel method with 100 MHz, e.g., the phase noise of the mw signal would be dominated by the DDS for frequencies greater than 100 Hz and cause an increase of the integrated phase noise of more than $80 \mu\text{rad}$. The achieved phase noise clearly facilitates interferometric measurements at the Heisenberg limit. In addition, the presented measurements have been performed without the 10 MHz reference attached, which would further improve the results for small offset frequencies.

Amplitude noise, on the other hand, is also relevant from shot to shot and not only during the interferometric sequence. The lower frequency limit is thus in principle only limited by the duration of the whole measurement campaign, typically on the scale of one hour ($278 \mu\text{Hz}$). The upper limit is again given by the pulse duration as 100 kHz. For $N = 10^4$ atoms, the coupling should ideally possess amplitude fluctuations $\sigma_a < 1/N = 0.01\%$ for state tomography. A stable mw dressing furthermore requires low energy fluctuations on the order of 10 mHz for typical energy shifts of 72 Hz, i.e., intensity fluctuations $\sigma_I < 10 \text{ mHz}/72 \text{ Hz} = 0.014\%$. We therefore aim at

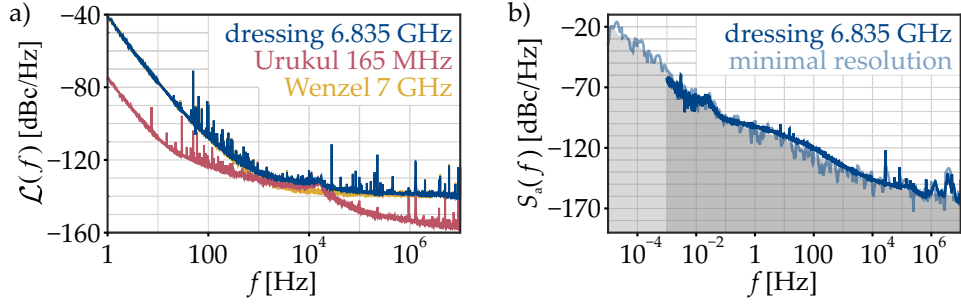


Figure 5.6: Phase and amplitude noise of the mw source. (a) Phase noise $\mathcal{L}(f)$ of the dressing path (dark blue), the *Urukul* at 165 MHz (red) and the 7 GHz *Wenzel* oscillator (yellow). The phase noise of the dressing signal is limited by the *Wenzel* oscillator for all frequencies except for a small frequency range around 16 kHz, where the *Urukul* dominates. Integrated phase noise of the signals (10 Hz to 100 kHz) is 483.1 μrad (dressing), 482.9 μrad (*Wenzel* 7 GHz) and 57.4 μrad (*Urukul*). (b) Fractional amplitude noise $S_a(f)$ of the dressing path for a setting with 1% resolution bandwidth and cross-correlation factor of 10 (dark blue) and a setting with minimum resolution setting of a single measurement per half-decade (transparent blue). The gray area indicates the corresponding sensitivity limits, coinciding with the measurement data.

fractional amplitude noise $\sigma_a = \sigma_I/2 \approx 0.01\%$ in the respective frequency range. The measurement of amplitude noise is difficult because it requires extraordinary long measurements for low offset frequencies. To this end, the amplitude noise is only properly measured down to 1 mHz and obtained as a rough estimate down to 10 μHz with low resolution settings (Figure 5.6 b). For the intended offset frequencies from 278 μHz to 100 kHz, the integrated amplitude noise evaluates to $\sigma_a = 0.017\%$. This presents only an upper limit because the measurement device is operated at its sensitivity limits. It can thus be assumed that the amplitude noise of the mw source does not hinder the manipulation and tomography of fragile quantum states for the given parameters.

5.3 STATE-SELECTIVE RADIO FREQUENCY TRANSFER

Transitions within the two hyperfine manifolds $F = 1$ and $F = 2$ are driven by different polarization because the respective linear Zeeman shifts p_B have opposite signs. While σ^+ enables transfer in $F = 2$, the $F = 1$ manifold requires σ^- polarization (Figure 5.7 a). A standard rf loop antenna, however, emits linearly polarized signals. Because this linear polarization can be decomposed into σ^+ and σ^- , it may drive transitions in both manifolds simultaneously. Moreover, a resonant frequency for one manifold is only slightly detuned for the other by the difference in $|p_B|$ of 2 kHz. Therefore, large transfer is observed in $F = 1$ and $F = 2$ at the same time. This can cause problems when atoms are stored in $|2, 0\rangle$, but an rf transfer should be driven only between $|1, 0\rangle$ and $|1, \pm 1\rangle$.

A solution for this problem is an rf source that emits only one of the two polarizations at the same time. This section presents such a source that

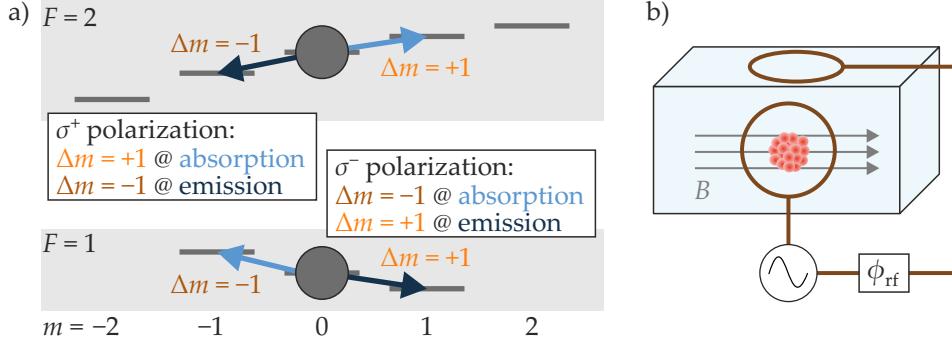


Figure 5.7: Schematic of state-selective rf transfer. (a) Schematic explanation of state-selective rf transfer. The two hyperfine manifolds have linear Zeeman shifts with opposite sign, but nearly equal absolute value. Absorption of a photon (light blue) increases the energy, while emission (dark blue) decreases it. Moreover, σ^+ polarized signals cause a change in the magnetic quantum number by $\Delta m = +1$ (light orange), while σ^- polarization results in $\Delta m = -1$ (dark orange). Therefore, σ^+ polarization causes the absorption to $\Delta m = +1$ and the emission to $\Delta m = -1$ in $F = 2$, while it ideally has no effect on $F = 1$. For σ^- photons, $F = 1$ is affected and $F = 2$ not. (b) Two antennas are mounted orthogonally as close as possible to the science glass cell. A relative phase shift ϕ_{rf} between the two signals changes the polarization of the combined signal and facilitates state-selective transfer.

combines two linearly polarized rf signals to create circularly polarized and therefore state-selective rf radiation. The general idea is that the magnetic field of rf signals can be understood to oscillate back and forth perpendicular to the loop antenna. Combining two such signals at an angle of 90° , the phase between the two linear oscillations defines the polarization direction. This relative phase between the rf signals can be set directly using the *Urukul* DDS module. The construction of rf loop antennas is quite different from mw antennas because the diameter of the loop is far away from the resonant wavelength of kilometers. Nevertheless, the antenna should be as large as possible to increase the emitted amplitude. Moreover, multiple windings can be used to further increase the signal strength. Three such antennas are placed in three orthogonal directions to match every possible magnetic field direction, as the antennas should be orthogonal to the quantization field (Figure 5.7 b).

For the operation of state-selective transfer, the amplitudes of the two signals have to be matched. This is done by individual Rabi measurements. The resulting combined Rabi frequency

$$\Omega_{2\text{rf}} = 2 \Omega_{\text{rf}} \left| \cos \left(\frac{\phi_{\text{rf}}}{2} \mp \frac{\theta}{2} \pm \frac{\pi}{4} \right) \right| \quad (5.1)$$

then only depends on the relative phase $\phi_{\text{rf}} = \phi_{\text{rf}1} - \phi_{\text{rf}2}$ between the rf signals, the resonant Rabi frequency Ω_{rf} and the deviation angle θ from 90° [77]. The upper sign corresponds to $F = 1$ and the lower to $F = 2$.

For a certain phase ϕ_{rf} between the two rf signals and ideal adjustment, one of the two transitions should be entirely suppressed while the other has its maximum transition rate. Figure 5.8 presents measurements of Rabi

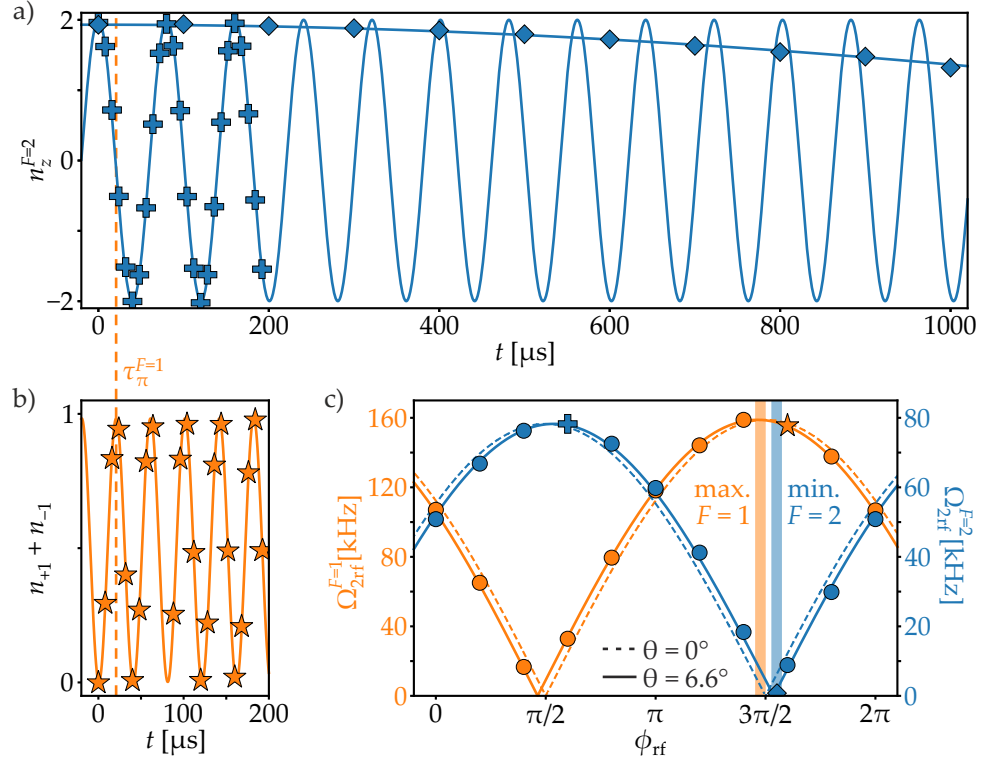


Figure 5.8: State-selective rf transfer. Rabi measurements are performed with respective resonance frequencies $f_{\text{rf}} = 632.428 \text{ kHz}$ for $F = 1$ (orange) and $f_{\text{rf}} = 629.903 \text{ kHz}$ for $F = 2$ (blue). Symbols correspond to measurement data and solid lines to fits. (a) Rabi measurements for $\phi_{\text{rf}} = 0.6 \pi$ (plus symbols) and $\phi_{\text{rf}} = 1.552 \pi$ (diamonds). The observable on the vertical axis is the z component of the spin-2 system, $n_z^{F=2} = 2n_{+2} + n_{+1} - n_{-1} - 2n_{-2}$, and initially the $|2, 2\rangle$ state is occupied by all atoms. (b) Rabi measurement in $F = 1$ with the relative side mode population $n_{+1} + n_{-1}$ plotted, starting with all atoms in $|1, 0\rangle$. The dashed line indicates the π pulse duration $\tau_{\pi}^{F=1} = 20.17 \mu\text{s}$ and is extended to (a). (c) Dependency of the Rabi frequencies in $F = 2$ (blue) and $F = 1$ (orange) on the relative rf phase ϕ_{rf} . Measurements from (a) and (b) are indicated by corresponding symbols. The transparent bars indicate the maximum in $F = 1$ and the minimum in $F = 2$ that are shifted due to a deviation angle θ (solid lines). These values are obtained by extra measurements around the turning points. Rabi frequencies in $F = 2$ are smaller by a factor of 2 because of different definitions of a π pulse.¹

frequencies in $F = 1$ and $F = 2$. For both cases, the respective resonance frequencies are employed. At a relative phase of $\phi_{\text{rf}} = 1.552 \pi$, the Rabi frequency in $F = 2$ is suppressed to only 771 Hz. In $F = 1$, this phase value is expected to still facilitate fast oscillations with $\Omega_{2\text{rf}}^{F=1} \approx 157 \text{ kHz}$. This is not the maximum Rabi frequency for $F = 1$ because this maximum is shifted with respect to the minimum of $F = 2$ due to a deviation angle that a fit estimates to $\theta = 6.6^\circ$. The state-selective rf transfer can also be set to work for $F = 2$ by adjusting the relative phase to the minimum of $F = 1$ at about $\phi_{\text{rf}} = \pi/2$.

¹ In $F = 1$, we define a π pulse to transfer all atoms from $|0\rangle$ into the symmetric superposition $|g\rangle$. For $F = 2$, a π pulse is usually defined to transfer all atoms from the maximum spin

In these measurements, both manifolds were driven with the corresponding resonance frequencies that differ by about 2 kHz. Our main use case of this technique, however, is a resonant transfer in $F = 1$ while some atoms are stored in the $F = 2$ manifold. Therefore, the signal is detuned to $F = 2$, which increases the Rabi frequency and reduces the suppression accordingly. An independent measurement thus investigated remaining transfer in $F = 2$ for a resonant state-selective transfer in $F = 1$. To this end, atoms were prepared in $|2, 0\rangle$ and in every other experimental cycle, a resonant transfer pulse was applied in $F = 1$. The detected number of atoms in any other state than $|2, 0\rangle$ could no be distinguished for both cycles and within the detection noise these numbers are compatible with zero transfer.

In summary, this technique enables a high degree of control over the coupling to individual hyperfine manifolds. In Section 7.1, it is described that this control facilitates the implementation of an mw clock on a magnetically insensitive transition with spin-squeezed states.

5.4 TECHNIQUES FOR NOISE-ROBUST PULSES

5.4.1 Pulse shaping

An electromagnetic pulse of duration τ has a certain frequency spectrum that can be obtained by Fourier transformation. The width of the frequency peak depends inversely on the pulse duration, such that long pulses yield narrow frequency signals. Moreover, the frequency response depends on the temporal shape of the pulse [144–146]. A simple box pulse, e.g., results in a $\sin(f)/f$ shape in frequency that has many small side peaks. An optimal frequency spectrum would have no side peaks at all to avoid driving off-resonant transitions. Additionally, the main peak should have a flat top to be insensitive to small experimental fluctuations of the detuning.

In the presented mw and rf system, different pulse shapes can be implemented using 1024 bit random-access memory (RAM) of the *AD9910* DDS chips in the *Urukul* module. Definitions for nearly arbitrary shapes can be predefined and retrieved from memory (Figure 5.9 a).

Theoretically, a $\sin(t)/t$ pulse in time would therefore be optimal, as it corresponds to a box in Fourier space. However, such a pulse is technically impracticable. A promising and feasible pulse shape is a Blackman shape [145] with amplitude

$$a(t) = \frac{1 - \alpha}{2} - \frac{1}{2} \cos\left(\frac{2\pi t}{\tau}\right) + \frac{\alpha}{2} \cos\left(\frac{4\pi t}{\tau}\right), \quad (5.2)$$

coefficient $\alpha = 0.16$ and pulse duration τ . The frequency response of this shape shows no visible side peaks, in contrast to a standard box-like pulse (Figure 5.9 b). It is therefore a preferred shape for our future experiments.

The pulse shaping technique could also be employed for laser pulses, when a shaped rf pulse drives an acousto-optical modulator and therefore

projection $|2, 2\rangle$ to the minimum $|2, -2\rangle$. A similar definition in $F = 1$ yields twice the π pulse duration and therefore half the Rabi frequency compared to our definition.

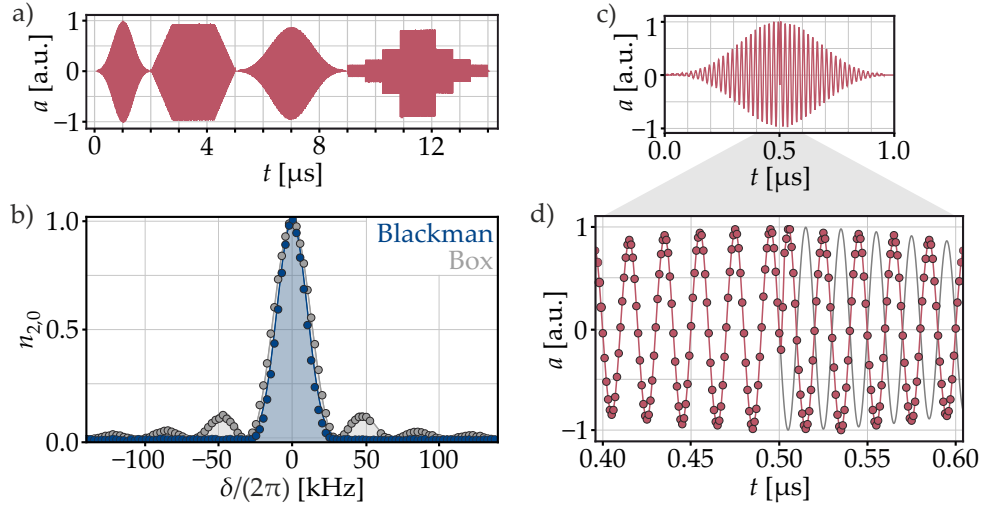


Figure 5.9: Pulse shaping of amplitude and phase. (a) Using the RAM mode of the *Urukul*, almost arbitrary amplitude-shaped pulses can be generated. This graph shows different shapes of amplitude a (Blackman, linear with plateau, Blackman and staircase), frequencies (50, 60, 70, 80 MHz) and durations (2, 3, 4, 5 μs). (b) Spectroscopy of the transition $|1, 0\rangle \leftrightarrow |2, 0\rangle$ for a box-like and a Blackman pulse shape. Plotted is the fraction of atoms in $|2, 0\rangle$ after a pulse with duration τ_π and frequency $f_{\text{mw}} = 6843.683 \text{ MHz} + \delta/(2\pi)$. The π pulse durations are 28.6 μs for the box and 69.3 μs for the Blackman pulse. The box-like shape clearly causes side peaks, while the Blackman pulse results in the main peak only. (c) Pulse at 50 MHz frequency with a polar shape, i.e., a shape in amplitude and phase. The phase of a pulse with a Blackman shape in amplitude is altered by π after 0.5 μs . (d) Zoom into (c), confirming the phase jump of π . Dots are measured data with the red line as a guide to the eye. The gray line extrapolates the pulse without a phase jump.

varies the beam intensity. In addition to the beneficial frequency response, smooth pulse shapes furthermore reduce high-frequency phase noise in atom interferometers [147].

The potential of the RAM mode is not exhausted by amplitude-shaped pulses. It enables precise sequences in amplitude, frequency, phase or amplitude and phase simultaneously. Figure 5.9 c-d) present an amplitude-shaped pulse with a phase jump in the middle of the pulse, implemented using the RAM. This exemplary shows the high degree of control with this system. Possible applications could be defined ramps for adiabatic passages through quantum phase transitions [69, 92, 99, 100] or Landau-Zener sweeps [128, 148].

5.4.2 Composite pulses

The pulse shaping technique engineers the frequency response of a single mw or rf pulse, in particular with respect to vanishing non-resonant transfer. Experimental deviations in the detuning, phase, amplitude or duration, however, still deteriorate the desired transfer. The duration and amplitude, which are connected by the Rabi frequency, are for example affected by the

exact position of the corresponding antenna. If the antenna is moving, e.g., due to thermal effects, this can change the amplitude of the radiating field and therefore the necessary pulse duration of a desired transfer. Magnetic field fluctuations, on the other hand, induce fluctuations of the energy levels and therefore change the resonance frequency of the atomic transitions.

One way to reduce these effects is to reduce the noise sources themselves, as it was pursued by improving the mw source or the magnetic field stability. Another possibility is to employ dedicated pulse sequences, so-called composite pulses, that cancel the effect of the deviations [149]. For this technique, a series of pulses has to be emitted in quick succession and with an adjustable phase. Luckily, the mw system enables fast updates on the order of μs and excellent phase control due to the *Urukul* module.

A composite pulse sequence is defined by the duration (rotation angle) and phase (rotation axis) of each individual pulse. The common notation θ_ϕ indicates a rotation of θ about an axis that is shifted by ϕ , e.g., 180°_0 for a standard π pulse. Some composite pulse schemes are better to suppress the influence of amplitude fluctuations while other are known to reduce the effect of frequency drifts. An example of a sequence that only suppresses influence of amplitude fluctuations is the *BB1* sequence [150],

$$180^\circ_0 \ 360^\circ_{208.9^\circ} \ 180^\circ_0 \ 180^\circ_{-104.5^\circ}, \quad (5.3)$$

that is presented in Figure 5.10 a-b). Instead of a single π pulse only, three additional pulses compensate an amplitude offset. In the Bloch sphere simulation, a box pulse achieves 85.4% transfer for a pulse duration of $0.75 \tau_\pi$, while the *BB1* sequence reaches 99.6%. The measurement data of a *BB1* sequence shows that transfer of more than 99% can be reached for $\tau \in [0.7, 1.3] \tau_\pi$. Transfer of the box pulse has a minimum of 75% in this range.

A so-called *Knill* sequence can be employed to reduce the effect of offsets in frequency and amplitude at the same time [151]. It is defined by

$$180^\circ_0 \ 180^\circ_{-30^\circ} \ 180^\circ_{60^\circ} \ 180^\circ_{-30^\circ} \ 180^\circ_0, \quad (5.4)$$

i.e., five pulses that are each a π pulse with different phase. The depiction on the Bloch sphere (Figure 5.10 c) directly shows that a single π pulse would deviate a lot from the desired value, but the composite sequence would not. Parameters of the Bloch sphere illustration are 90% π -pulse duration and a detuning of $0.5 \Omega_{\text{mw}}$, resulting in 78% transfer for the box and 98.8% transfer for the *Knill* pulse. In fact, the 2D simulation in Figure 5.10 d) yields large transfer for a broad range of frequency and amplitude offsets. The experimental data confirms this.

Such composite pulses that reduce detuning errors have the drawback of larger non-resonant transfer, which makes it, e.g., unusable for Raman transfer with a Doppler shift of a few kilohertz. If there are no other transitions in direct vicinity, those pulses, however, reduce the sensitivity to offsets in many experimental parameters drastically. It should be said that it is not always beneficial to employ long composite sequences instead of a single short pulse because the fluctuations to reduce have to be slower than

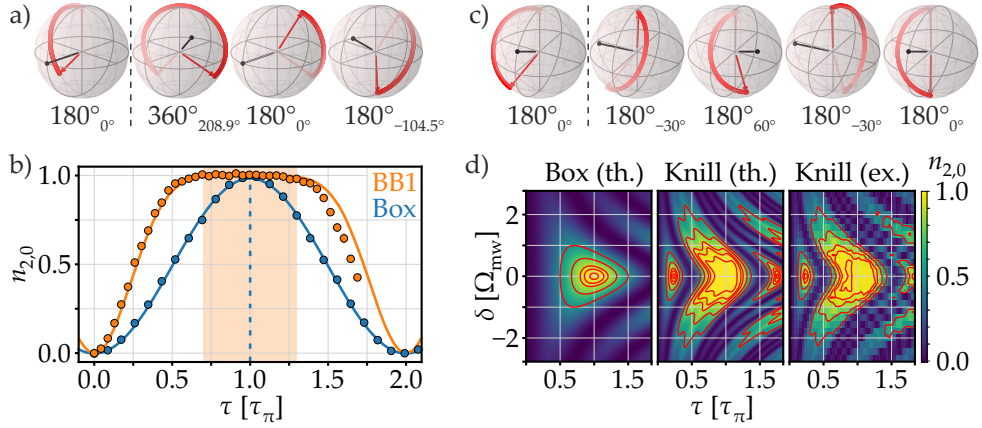


Figure 5.10: Composite pulse sequences. (a) Bloch sphere representation of a *BB1* sequence to cancel amplitude deviations. Rotation axes are indicated by black lines, initial states of a pulse by light red and final states by dark red arrows. The notation θ_ϕ corresponds to a pulse with rotation angle θ around an axis that is shifted by ϕ . The duration of the pulse is only 75% of the π pulse duration (left sphere), resulting in diminished transfer. Three subsequent pulses with different rotation axes compensate this error and achieve nearly perfect transfer. (b) Rabi measurement for a box pulse (blue) and a composite *BB1* pulse sequence (orange). The π pulse duration $\tau_\pi = 115.5 \mu\text{s}$ is extracted from a fit to the box pulse (solid blue line) and indicated by a dashed blue line. The solid orange line corresponds to the expectation from Bloch sphere rotations with the experimental π pulse duration. The shaded orange area indicates transfer larger than 99% of the *BB1* with respect to the maximum value. (c) A *Knill* pulse sequence robust to amplitude and detuning errors is depicted on Bloch spheres. The π pulse duration is only 90% and the presented detuning is half the Rabi frequency Ω_{mw} . (d) Comparison of a box pulse and a composite *Knill* sequence for a π pulse. In theory, the *Knill* sequence is much more robust against detuning and amplitude deviations than a box pulse. Experimental data confirms the features of this pulse sequence. The pulse parameters are a Rabi frequency of $\Omega_{\text{mw}} = 27 \text{ kHz}$ and a π pulse duration of $\tau_\pi = 115 \mu\text{s}$. Red lines indicate transfer of 99, 95, 90, 75 and 50%. This visualization is adapted from Baron [128].

the duration of the pulse sequence. To this end, composite pulses are not applicable to cancel high-frequency noise, they might even make it worse. For long-term drifts, on the other hand, they present a useful tool, enabled by the excellent phase control of the *Urukul*.

5.5 DISCUSSION

This chapter presented a novel mw and rf system for the manipulation of spinor BECs. Instead of many individual devices, all required signals are generated by a single system that relies in particular on an FPGA as a control instance and a DDS module for versatile frequency generation. This setup could even be extended by analog voltage signals (input and output) using further components of the *Sinara* hardware ecosystem. In this way, an entire experiment control architecture can be constructed, controlled by the open-source software *ARTIQ*.

A particular focus of the chapter was on a device for mw generation with ultra-low noise and versatile features. The integrated phase noise for an interferometrically relevant frequency range evaluates to $\sigma_\phi = 483 \mu\text{rad}$ and therefore enables preparation and manipulation with phase resolution at the Heisenberg limit. The amplitude noise of $\sigma_a = 0.017\%$ is estimated as an upper bound, but is nevertheless also close to the Heisenberg limit for respective atom numbers and therefore facilitates low-noise operation. Finally, the low amplitude noise ensures a stable mw dressing field.

The rf pulses also benefit from the low noise of the *Urukul* DDS module. Moreover, state-selective transfer enables coupling of a single hyperfine manifold. This enables transfer of spin-squeezed states to magnetically insensitive states, which is further discussed in Section 7.1.

Additional techniques for pulse engineering were presented to reduce the effect of technical issues like unwanted transfer or frequency drift. The Blackman pulse shape, e.g., now presents the commonly used one in our experiments. It is also possible to design a dedicated frequency response for special scenarios, apply Fourier transformation and then directly employ this temporal pulse shape. Composite pulses, on the other hand, might come with some drawbacks. However, some sequences like the *BB1* might be beneficial for certain applications and the precise phase control now enables this.

In summary, the novel mw and rf system possesses advantageous noise properties, enables state-selective rf transfer and facilitates techniques for technical noise suppression. It will be therefore a useful tool in future experiments on atom interferometry and quantum many-body physics.

A possible improvement of the system could be the implementation of state-selective mw transfer. For hyperfine transitions $|1, 0\rangle \leftrightarrow |2, \pm 1\rangle$, cross transfer $|2, 0\rangle \leftrightarrow |1, \pm 1\rangle$ occurs because the mw frequencies do not resolve the quadratic Zeeman shift and our antennas contain all three polarizations with relative magnitudes defined by its positioning. A possible workaround would be to work at magnetic fields where the detuning of the parasitic transition results in a 2π pulse and thus does not transfer atomic population. Experimentally, however, this is not very feasible because we want to work at magnetic fields close to 1 G for low magnetic-field noise. A different approach is to employ the polarization to discriminate the transitions, similar to the state-selective rf transfer. Signals with defined circular polarization would then only drive $\Delta m = +1$ or $\Delta m = -1$. A challenge for state-selective mw transfer is the wavelength of this radiation that is only on the order of centimetres and reflections that could contribute an undesired phase. Boguslawski [87] describes possible antenna designs for this purpose, e.g., an antenna that includes two emitters of mw radiation and therefore requires two phase-controlled mw signals or a helical antenna that directly emits circularly polarization from a single signal source. Such a tool would further improve the precise manipulation of spin states in our experiments.

AN EXCITED-STATE QUANTUM PHASE DIAGRAM

This chapter presents the main experimental results of this thesis. It illustrates the preparation of excited states in our spinor system and the resulting mapping of an excited-state quantum phase diagram. Moreover, it describes the difficulties in measuring the interferometric phase and different approaches to handle those. The main results are published in Meyer-Hoppe et al. [152].

6.1 PREPARATION OF EXCITED-STATES

The excited-state quantum phase diagram spans all possible combinations for the QZE $q/|\Omega|$ and the excitation energy η^* . This section describes how any point in the phase diagram can be experimentally reached.

The excitation energy per particle is defined as (Equation 3.12)

$$\eta^* = \frac{1}{8} \left(\frac{q}{|\Omega|} + 2 \right)^2 - n_0 \frac{q}{|\Omega|} - 2 (1 - n_0) n_0 \cos^2(\varphi) \quad (6.1)$$

in the relevant region $|q/\Omega| \leq 2$. A preparation of a defined excited state $(q/|\Omega|, \eta^*)$ in the phase diagram requires the precise adjustment of the QZE $q/|\Omega|$, the relative population n_0 and the relative phase φ (Figure 6.1). In general, we start with all atoms in $|0\rangle$, i.e., with a relative population $n_0(0) = 1$, and a relative phase $\varphi(0) = -\pi/2$. The initial QZE is the contribution by the magnetic field, q_B , that evaluates to $q_B/h \approx 65$ Hz for our magnetic fields of 0.95 G. This initial state is a ground state in the P' phase.

To prepare the horizontal position in the phase diagram, the QZE $q/|\Omega|$ is adjusted by a quench of the mw dressing frequency, as described in Section 4.4. However, because we start with all atoms in $|0\rangle$ (P' phase) and the ground state for $q/|\Omega| < 2$ is not $|0\rangle$ any more, quenching to smaller values than $q/|\Omega| = 2$ already introduces an excitation energy $\eta^* = \frac{1}{8} (q/|\Omega| - 2)^2$. The point in the phase diagram after the quench will thus be on the transition line between P' and BA' for $q/|\Omega| > 0$ (blue line in Figure 6.1) and on the highest energy line of the TF' phase for $q/|\Omega| < 0$. In the Bloch sphere picture, this quench changes the topology of the sphere, i.e., different possible trajectories depending on the excitation energy arise.

In a next step the excitation energy, i.e., the vertical axis in the phase diagram is adjusted by an interplay of rf transfer and phase imprint (Section 4.3). On the Bloch sphere, this corresponds to rotations about the y axis and the z axis for rf transfer and phase imprint, respectively. In this way, a trajectory on the Bloch sphere is chosen.

As already mentioned, we cannot experimentally prepare eigenstates of the Hamiltonian. Those states would have a precisely defined energy, therefore the phase would be undefined and the state would expand over the entire trajectory on the Bloch sphere. Instead, we prepare coherent states,

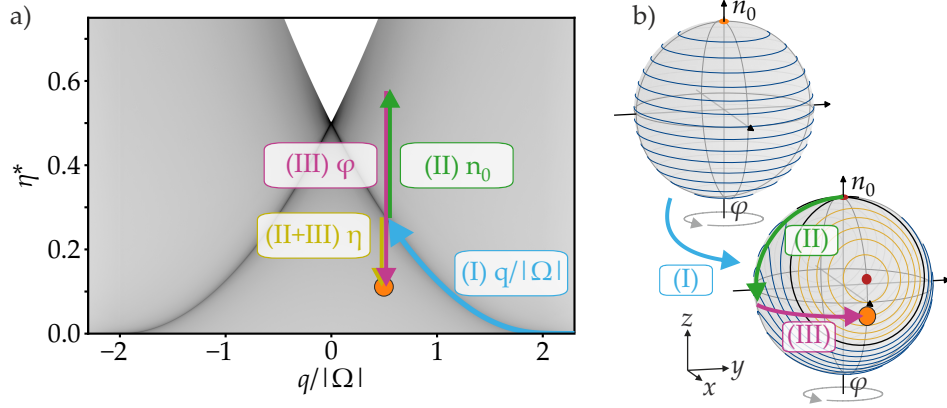


Figure 6.1: Preparation of excited states. (a) In the background, the excited-state phase diagram is shown with the QZE $q/|\Omega|$ on the horizontal and the excitation energy η^* on the vertical axis. The (not individually visible) lines correspond to eigenenergies of the respective Hamiltonian for $N = 70\,000$ atoms, where the ground-state energy has been subtracted. The regions with high density of states signalize phase transitions. Preparation of excited states is shown in the phase diagram (a) and on the Bloch sphere (b). The effect of an initial quench of the QZE $q/|\Omega|$ is shown in blue. In addition to a variation of $q/|\Omega|$ only, an excitation is introduced. On the Bloch sphere, trajectories of different phases emerge. Subsequent population transfer by rf (green) and/or phase imprint by mw (pink) adjust the excitation energy η^* (gold) to an arbitrary value of the diagram. This corresponds to rotations around the y and z axis, respectively. The final state is indicated by an orange dot.

i.e., states within a narrow energy window that correspond to a disk with a radius proportional to \sqrt{N} . This first seems like a disadvantage. However, in contrast to the eigenstates, the coherent state undergoes dynamics that we can track and with which we will distinguish the different quantum phases. For energy eigenstates, the phase diagram would nevertheless look exactly the same.

For relative population and phase uncertainties connected to fundamental fluctuations of $1/\sqrt{N}$, we expect unavoidable energy uncertainties. In the case of $q/|\Omega| = 1$, $\varphi = 0$ and $n_0 = 0.5$, e.g., the relative uncertainty in η would be 1.5% for $N = 70\,000$ atoms. This does not take into account that those parameters can possess experimental fluctuations. Nevertheless, this shows that albeit not preparing energy eigenstates the coherent states are prepared within a small energy window.

6.2 POPULATION OSCILLATIONS

A straightforward quantity to look at when investigating the dynamics of a quantum system is the oscillation and distribution between the different atomic states. This observable has already served as an order parameter for ground-state quantum phase transitions (Section 3.2). To measure the population dynamics in the spin-1 system, we prepare an excited state as explained above. After variable evolution times t , the population of the different spin

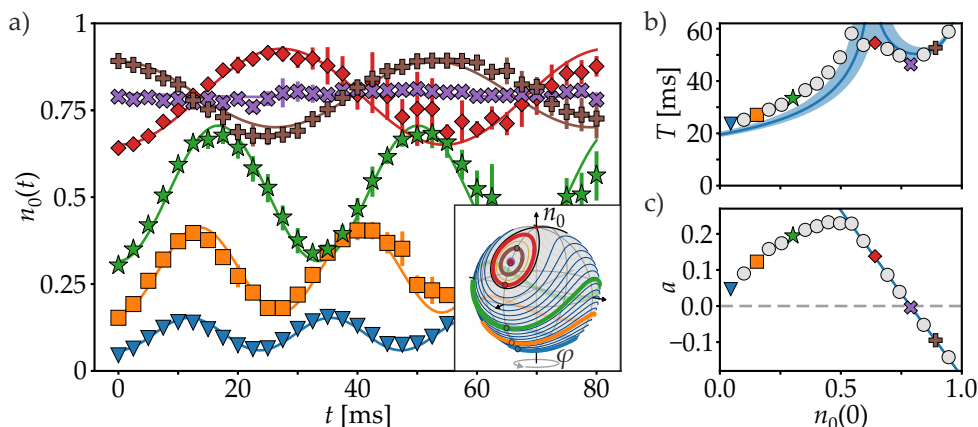


Figure 6.2: Population oscillations. At $\varphi(0) = 0$ and $q/|\Omega| = 1.25$, different initial populations $n_0(0) \in \{0.05, 0.1, \dots, 0.95\}$ are prepared and the evolving population is measured at times t . (a) Time evolution of the relative population $n_0(t)$. Colored symbols indicate different initial populations. Lines are cosine fits to extract the period T and oscillation amplitude a . The expected evolutions are depicted on the Bloch sphere in the inset. (b) Extracted periods T for the oscillations in (a) and additional measurements (gray circles). The blue line presents a theoretical simulation and shading fluctuations of $q/|\Omega|$ by ± 0.1 . (c) From the extraction of the oscillation amplitudes, the stationary point can be deduced. A hint for this point can also be seen in (b), but a linear fit close to zero amplitude (blue) yields a precise result for the relative population at the stationary point. The experimentally determined stationary point is at $n_0 = 0.788(1)$, while it is theoretically expected at 0.8125.

states is measured. For our effective two-mode system consisting of $|0\rangle$ and $|g\rangle$, we look at the fraction $n_0 = N_0/N$ of atoms in $|0\rangle$ with respect to the total atom number N .

Figure 6.2 a) presents a measurement of population oscillations with fixed QZE and initial phase, but varied initial population $n_0(0)$. In the phase diagram, the corresponding states form a vertical line at $q/|\Omega| = 1.25$. Clear oscillations are visible that resemble the trajectories on the Bloch sphere (inset of the figure). Moreover, diverging oscillation periods already indicate crossing of a phase transition [46, 106]. Deviations, especially for the red trajectory close to the separatrix, might be explained by phase space mixing [153].

Two quantities can be extracted from such an oscillation. On the one hand, the population oscillation periods T can be extracted (Figure 6.2 b). This parameter is required for the measurement of the proposed interferometric order parameter (Section 3.3.3). To obtain the periods, the data is fitted to a cosine function $n_0(t) = a \cos(2\pi t/T) + b$. In principle, the oscillations follow Equation 3.17, but a cosine fit directly gives the period and the oscillation amplitude.

This oscillation amplitude a is the second interesting quantity to extract because it indicates the stationary point. Note that these points always occur at phase $\varphi(0) = 0$. It can directly be seen that the purple crosses in Figure 6.2 a) do not oscillate and are thus close to the stationary point. For

a thorough determination, the amplitude of the presented oscillations is extracted and plotted against the initial population (Figure 6.2 c). From a linear fit around zero amplitude, the point of no oscillation at $n_0 = 0.788(1)$ can be acquired. This turning point of the oscillation amplitude marks the stationary point.

Experimental findings fit the theoretical model well. In particular, the phase transition can already be anticipated at the diverging population oscillation period. Deviations from the model can be explained by imperfect adjustment and drifts of $q/|\Omega|$, as detailed in Section 4.4. For example, the stationary point for the adjusted QZE $q/|\Omega| = 1.25$ is in theory located at $n_0 = 0.8125$. The experimental value $n_0 = 0.788(1)$, on the other hand, indicates $q/|\Omega| = 1.18$, which is in agreement with the expected deviations of the QZE.

Instead of varying the initial population for a defined $q/|\Omega|$ to obtain oscillation periods, we also keep the initial relative population fixed at $n_0(0) = 0.5$ and vary the QZE. This measurement is similar to Zhao et al. [106], where spin oscillation periods are measured for an antiferromagnetic system. The

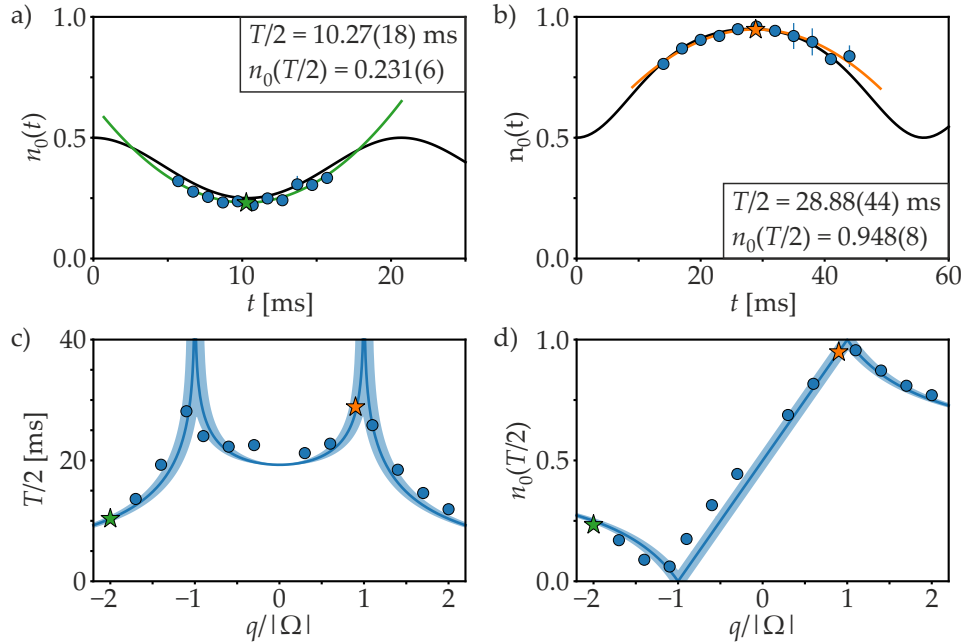


Figure 6.3: Determination of half periods for a variation of $q/|\Omega|$. At fixed $n_0(0) = 0.5$ and $\varphi(0) = 0$, different values for the QZE are adjusted to prepare excited states. (a-b) Measurements of population oscillations $n_0(t)$ at $q/|\Omega| = -2$ (a) and $q/|\Omega| = 0.9$ (b) in the vicinity of the half period $T/2$. Parabolic fits (green and orange lines) of the measurement data (blue dots) are employed to determine the half period $T/2$ and the population at this point in time (green and orange stars). Black lines correspond to the theoretically expected full evolution. (c-d) Half periods (c) and populations at the half period (d) are extracted from many oscillations as in (a-b) and plotted as dots. The highlighted stars correspond to extracted results from (a) and (b). A theoretical simulation is each depicted by a solid blue line and the shading indicates fluctuations of ± 0.1 in $q/|\Omega|$.

phase is again set to $\varphi(0) = 0$. This then corresponds to a horizontal curve in the phase diagram. As an alternative to measure full oscillations, we just measure short evolutions close to the theoretically proposed values of the half period $T/2$. We obtain the population $n_0(t)$ with small time steps and fit the turning points by parabolic fits (Figure 6.3 a-b). This experimentally determines the half periods $T/2$ which are going to be important later on. We see that theory and experiment yield compatible results and that we can in general rely on theoretical calculations for T and $T/2$ instead of measuring it every time. Note that even larger deviations in the oscillation period T would only change the measurement of the proposed interferometric order parameter quantitatively in the sense of blurred phase transitions, but not qualitatively.

6.3 PHASE SIGNAL

The measurement of the proposed interferometric order parameter requires the determination of the spinor phase after evolution times on the order of tens of milliseconds. During this evolution time, any additional phase signal deteriorates the measurement. To this end, the proposed scheme imposes the experimental challenge to reduce any disturbing phase noise source. Phase noise of mw and rf signals are not relevant, even though the improved setup presented in Chapter 5 is not used here. Instead, magnetic field fluctuations seem to be the only relevant challenge [76].

In the proposed experimental sequence, a variable rf pulse initially populates the $|\pm 1\rangle$ modes and after an evolution time, a closing rf $\pi/2$ pulse maps the phase onto the population distribution. However, magnetic field fluctuations cause a varying linear Zeeman shift from shot to shot compared to the resonant coupling of the rf signal. This, in turn, induces an additional relative phase between $|+1\rangle$ and $|-1\rangle$ that depends on the evolution time, but also on the strength of the magnetic field deviation. The superposition of $|+1\rangle$ and $|-1\rangle$ therefore oscillates between symmetric ($|g\rangle$) and antisymmetric ($|h\rangle$) from shot to shot. Finally, the closing rf pulse couples only to the symmetric state, such that the measurement outcome fluctuates depending on the detuning of the magnetic field.

A deviation in the magnetic field ΔB induces an extra phase $\Delta\phi = b_p T_{\text{ev}} \Delta B$ (Equation 4.1). To observe the phase evolution for the presented full population oscillations T , evolution times $T_{\text{ev}} \approx 70$ ms are required (Figure 6.2). For a maximum phase variation of $\pm\pi/4$ for different experimental realizations, magnetic field deviations $\Delta B < 8 \mu\text{G}$ would be required, which is not feasible in our setup. With our experimental apparatus, we achieve magnetic field fluctuations of $50 \mu\text{G}$ from shot to shot. This allows for evolution times of only $T_{\text{ev}} \approx 11$ ms. Therefore, not even the order parameter for the half period $T/2$ (Section 3.3.3) could be employed, compared with typical evolution times in Figure 6.3.

The result of a phase measurement with shot-to-shot magnetic field fluctuations of $50 \mu\text{G}$ can be seen in Figure 6.4. In this measurement, we perform a direct readout (projection along z axis, b), a readout after rf $\pi/2$ pulse

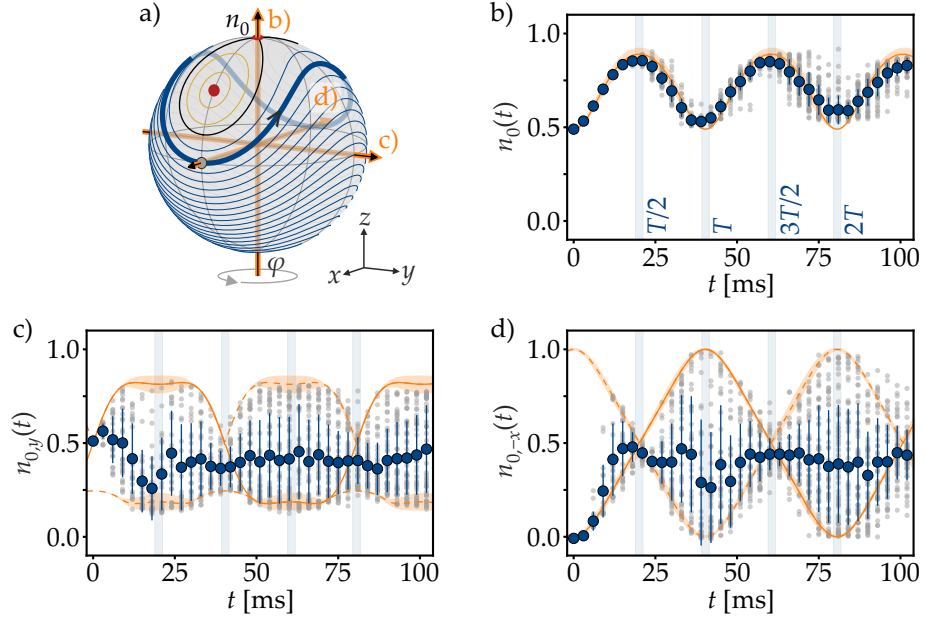


Figure 6.4: Phase signal. (a) Bloch sphere illustration of the trajectory to measure (thick blue) with $n_0(0) = 0.5$, $\varphi(0) = 0$ and $q/|\Omega| = 1.25$ and additional exemplary trajectories (thin lines). The starting point is depicted by a gray circle. Orange arrows indicate the projection axis along which the measurements in (b-d) are performed. At every time step, three individual measurements are performed for the measurement axes. (b-d) Measurements along the z axis (b), y axis (c) and $-x$ axis (d). Solid orange lines indicate the expected trajectory, dashed lines the theoretical boundary of the fluctuations and light blue bars multiples of the half oscillation period $T/2$. Shading represents deviations of ± 0.1 in $q/|\Omega|$. While the population measurement (b) is not affected by a varying magnetic field, the orthogonal measurements (c-d) show large fluctuations.

(y axis, c) and a readout after mw $\pi/2$ phase shift and subsequent rf $\pi/2$ pulse ($-x$ axis, d). While the measurement along the z axis is not affected by the magnetic field, the two phase-sensitive measurements show large fluctuations from shot to shot.

Nevertheless, the intended dynamics is visible and some interesting features can be taken from this measurement. First of all, the initial data points at evolution times up to a few milliseconds still follow the expected signal of the trajectory. The observable evolution time without too much fluctuations also fits very well to the prediction of 11 ms. This means that phase measurements are at least still feasible for short evolution times of a few milliseconds. Secondly, the fluctuations are not entirely random, they are within the boundaries from theory expectations. For larger evolution times, the individual realizations fluctuate between two extreme values, i.e., the expected signal and a mirrored version. A descriptive explanation of this mirrored signal stems from the oscillation between $|g\rangle$ and $|h\rangle$ due to magnetic field fluctuations. Whenever the atoms cycle from $|g\rangle$ to $|h\rangle$ and back, this is attributed to a phase shift of π for the symmetric superposition and therefore a measurement outcome mirrored at 0.5. Lastly, the magnetic field deviations seem to be responsible for the large fluctuations. With a technique

that selects experimental runs with low deviation, one may therefore obtain the trajectories and extract the desired order parameter. Those three features result in ideas to still observe ESQPTs. The next three sections each cover one of them.

6.4 DISTINGUISHING EXCITED-STATE QUANTUM PHASES

6.4.1 Iterative measurement

As it can be seen in Figure 6.4 c-d), the expected phase signal is still visible up to a few milliseconds. One idea to still observe the phase oscillations is therefore to look at successive small evolution steps of a few milliseconds that are not deteriorated by fluctuations instead of a long evolution. Because in every evolution step a coherent state is prepared, this method reflects the mean-field approximation only. Quantum fluctuations, for example leading to squeezing effects, are negligible in this case.

Such an iterative measurement is presented in Figure 6.5. The initial state $(n_0^{(0)}, \varphi^{(0)})$ is prepared at a certain QZE, in this case $q/|\Omega| = 0.5$. After a short

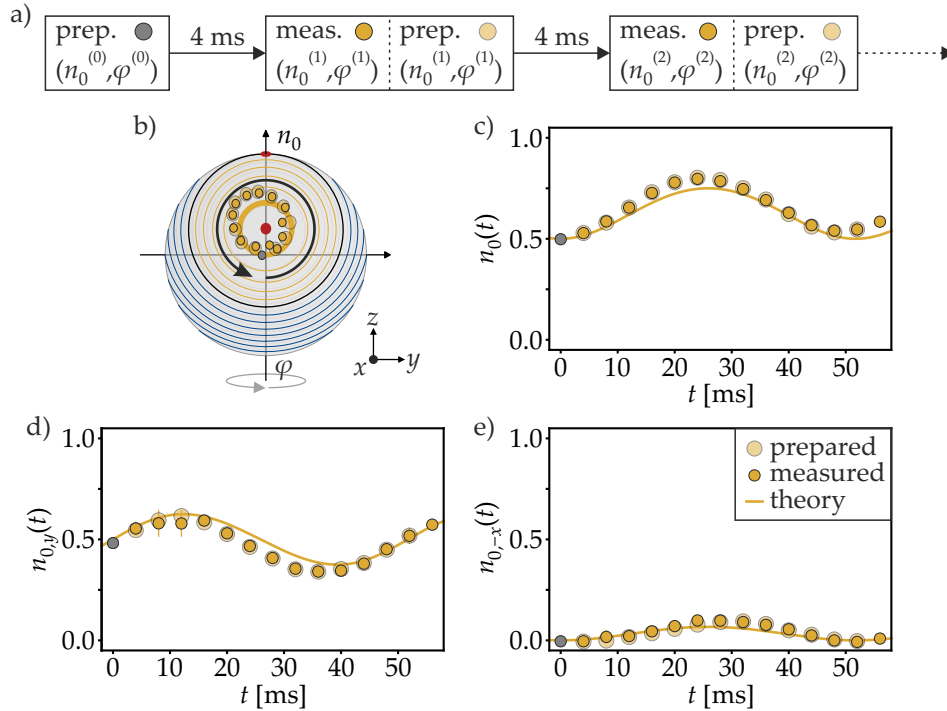


Figure 6.5: Iterative procedure to measure a phase evolution. (a) Schematic representation of the iterative measurement procedure. The superscript number in brackets indicates the iteration step. (b) Bloch sphere representation of the combined population and phase measurement results for $q/|\Omega| = 0.5$. The gray dot indicates the starting value, filled dots measured data after evolution of 4 ms and transparent dots prepared states for the subsequent initialization. (c-e) Measurements along the z axis (b), y axis (c) and $-x$ axis (d). Dots as in (b) and solid lines correspond to theoretical expectations.

evolution (4 ms), the resulting population $n_0^{(1)}$ and phase $\varphi^{(1)}$ are determined by independent measurements. In a next step, the state $(n_0^{(1)}, \varphi^{(1)})$ is then prepared, followed by another short evolution and a readout of $n_0^{(2)}$ and $\varphi^{(2)}$. This stepwise procedure can be repeated until the population oscillation period T is reached. As it can be seen in Figure 6.5, clean oscillations are visible that resemble the expected trajectory.

This method enables the extraction of the phase $\varphi(T)$ after a population oscillation period T . Depending on this phase, the trajectory and thus the corresponding excited state ($q/|\Omega|, \eta^*$) can be classified into the TF', BA' or P' phase. Figure 6.6 presents this iterative method for three different values of $q/|\Omega|$, but the same $n_0(0)$ and $\varphi(0)$. The measurements along the x and y axis are combined to retrieve $\varphi(t)$.

As expected, the population oscillations follow the theoretical model very well (Figure 6.6 d). The three trajectories reach the initial population again after different oscillation periods T close to respective theoretical turning points. At those times T , the phase $\varphi(T)$ in Figure 6.6 e) yields the assignment to the respective quantum phases. A clear phase signal is visible

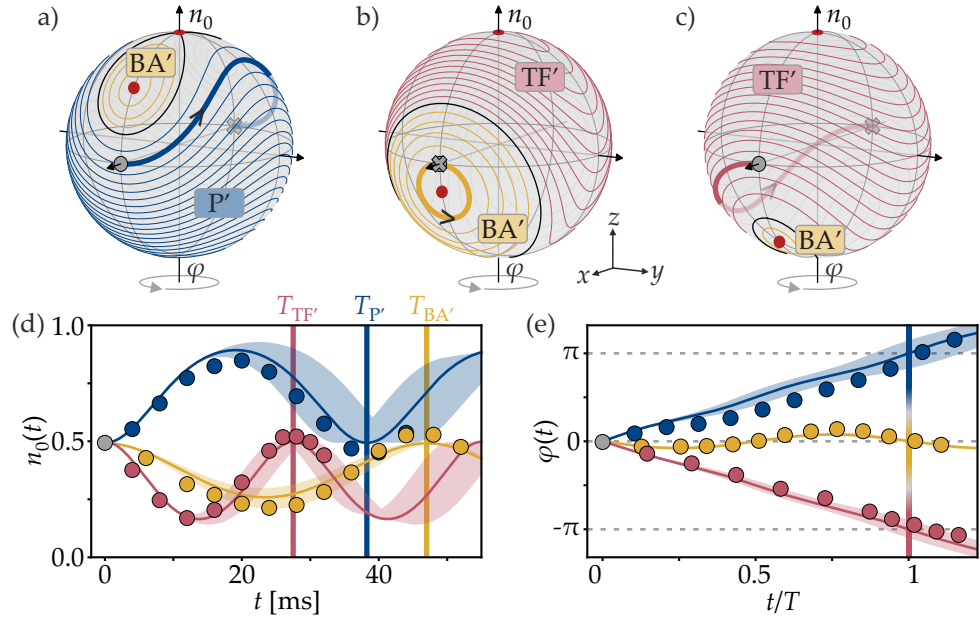


Figure 6.6: Extracting the order parameter by iterative measurements. (a-c) Bloch sphere representations for $q/|\Omega| = \{-1.5, -0.5, 1.25\}$. Investigated trajectories are highlighted as thick lines. The starting point is represented by a gray circle and the point after one population oscillation period by a gray cross. (d) Population measurement for the trajectories presented in (a-c). Colored dots correspond to iterative measurement data after the respective short evolution steps, solid thin lines to theoretical expectations and shading to fluctuations of $q/|\Omega|$ by ± 0.1 . The population oscillation periods are indicated by thick vertical lines with corresponding color. (e) Phase measurement of the trajectories. The horizontal time axis is rescaled by the population oscillation periods from (d). At time T , a color bar indicates the respective assignment to the ESQPTs. Shading is again fluctuations in $q/|\Omega|$ by ± 0.1 .

that is bounded for the BA' phase and running around the sphere for the P' and TF' trajectories. After the population oscillation period, the TF', BA' and P' trajectories have phase values of $\varphi(T) = \{-0.93, 0.03, 0.94\} \pi$, respectively. Those values are close to the theoretical values of $\varphi(T) = \{-1, 0, 1\} \pi$ and therefore clearly determine the corresponding excited-state quantum phases.

As already mentioned, this method is always preparing coherent states, which does not correspond to the real evolution as squeezing and shearing effects in principle appear. This method therefore indeed maps the mean-field trajectories, but does not follow the real evolution that the quantum state would experience. Moreover, this method is experimentally very time consuming. Despite the nice trajectory mapping and classification of phases, it is therefore not perfectly suited for the measurement of phase transitions. For such measurements, it would be desirable to only prepare an initial state and look at the phase value after the time T .

6.4.2 Signal in the fluctuations

This section investigates features in the fluctuations of the measurement data. As already seen in Figure 6.4 c-d), even the measurement data for long evolution times is bounded by defined curves that arise due to magnetic field fluctuations. The minimum and maximum values of the projection $n_{0,y}$ due to deviations in the magnetic field are (Appendix A.2)

$$n_{0,y}^{\max}(t) = \frac{1}{2} + \sqrt{n_0(t)(1-n_0(t))} |\sin(\varphi(t))|,$$

$$n_{0,y}^{\min}(t) = \begin{cases} \frac{1}{2} n_0(t) \cos^2(\varphi(t)) & \text{if } \frac{n_0(t) |\sin(\varphi(t))|}{1-n_0(t)} < 1, \\ \frac{1}{2} - \sqrt{n_0(t)(1-n_0(t))} |\sin(\varphi(t))| & \text{else.} \end{cases}$$
(6.2)

At the half period, a trajectory in the BA' phase evolves to $\varphi(T/2) = 0$. Therefore, $n_{0,y}^{\max}(T/2) - n_{0,y}^{\min}(T/2) = (1 - n_0(T/2))/2$ and the boundaries coincide at $n_0(T/2) = 1$. Similar arguments hold for the P' and TF' phases. The value of $n_0(T/2) = 1$ is approached when an initial state is prepared close to the separatrix, i.e., close to the phase transition. Vanishing fluctuations therefore indicate the vicinity of an ESQPTs.

To investigate this experimentally, we look at the projection along the y axis, i.e., the relative population $n_{0,y}$ after a $\pi/2$ rotation about the x axis (Figure 6.7). At $q/|\Omega| = 1.25$ and $\varphi(0) = 0$, we measure the population $n_{0,y}(T/2)$ after a half period for different initial populations $n_0(0)$. As expected, the mean values do not give any useful information, but the fluctuations do. The experimental realizations are indeed bounded by n_{\max} and n_{\min} . From the measurement data, we can extract the standard deviation and plot it in Figure 6.7 d). The point of minimum fluctuations signalizes a phase transition that is indeed close to the theory prediction. A similar measurement has also been performed with a variation of $q/|\Omega|$ and fixed $n_0(0)$ (Appendix A.3).

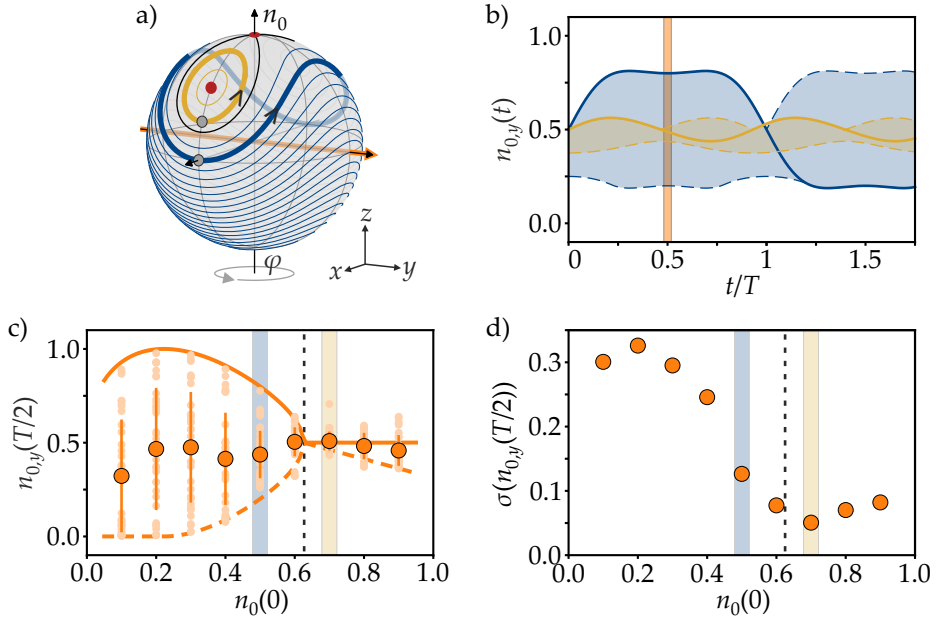


Figure 6.7: Signal of a phase transition in the fluctuations. (a) Bloch sphere for $q/|\Omega| = 1.25$. Trajectories with $n_0(0) = 0.5$ and $n_0(0) = 0.7$ are highlighted, each with $\varphi(0) = 0$. Starting points are indicated by gray circles. The measurements are performed as a projection onto the orange axis. (b) Theoretical simulation for $q/|\Omega| = 1.25$ and $|\Omega|/h = 11.5$ Hz. The blue (larger) curves belong to $n_0(0) = 0.5$ and the yellow (smaller) ones to $n_0(0) = 0.7$. Solid lines indicate the signals without magnetic field detuning, dashed lines and shading depict the boundaries including magnetic field fluctuations. At the orange shaded bar, the half period is reached. (c) At the calculated half period $T/2$, the population along the y axis is measured for different initial populations $n_0(0) \in \{0.1, 0.2, \dots, 0.9\}$. Light orange dots indicate individual measurements, dark orange dots mean values and orange error bars the standard deviations. The blue and yellow shaded bars correspond to the curves in (b) and the trajectories in (a). Orange lines indicate the boundaries $n_{0,y}^{\min}$ and $n_{0,y}^{\max}$. The dashed black line indicates the theoretically expected value for a phase transition at $n_0(0) = 0.625$. (d) Standard deviation of the measurement data in (c), depicted as orange dots, plotted against the initial population $n_0(0)$. Vertical lines as in (c). The vanishing fluctuations indicate the phase transition point.

This method in principle facilitates the observation of excited-state quantum phase transitions. It is not restricted by magnetic field deviations, but presumably works even better with larger fluctuations. To this end, it might even be advantageous to measure the signal at $3T/2$ instead of $T/2$ because of the larger fluctuations (compare Figure 6.4 c). However, it is very difficult to assign a critical value of η^* , in this case defined by $n_0(0)$, to the phase transition because there is no sharp order parameter, but a continuous transition. Moreover, we just find the transitions, but cannot distinguish the individual quantum phases by this method.

6.4.3 Separation of the symmetric contribution

The measurements in the previous section show that we can indeed observe signals of phase transitions. However, it is not easy to pinpoint the exact location of a phase transition using this method. A method presented in this section follows a different approach. It has become clear that shot-to-shot magnetic field deviations are responsible for the fluctuations of the measurement outcome. The idea is now to post-select experimental runs with negligible magnetic field deviation. In this way, the magnetic field is constant and a coupling to the symmetric superposition is possible in many experimental realizations.

Magnetic field deviations cause a relative phase between $|+1\rangle$ and $|-1\rangle$, so that the atoms are no longer in the symmetric superposition $|g\rangle$. If we, however, only detect atoms in the symmetric superposition, we can deduce that they experienced no detuning of the magnetic field. We therefore need a scheme to separate atoms in the symmetric superposition from atoms with a phase shift due to magnetic field fluctuations. Note that atoms in $|g\rangle$ cycling once to $|h\rangle$ and back experience a phase shift of π and therefore a minus sign. Those atoms cannot be excluded by this method, but occur as a mirrored signal.

Such a scheme is presented in Figure 6.8. It particularly relies on the fact that an rf pulse by default transfers only the symmetric component of $|\pm 1\rangle$ to $|0\rangle$ (Section 2.2.3). The excited state is prepared as usual using mw dressing, rf transfer and mw phase imprint. This state is then described by a product of single-particle states

$$|\psi\rangle = \sqrt{n_0} e^{-i\varphi} |1,0\rangle + \sqrt{1-n_0} (\cos(\beta) |g\rangle - i \sin(\beta) |h\rangle) \quad (6.3)$$

with the mixing angle β due to magnetic field fluctuations. After an evolution time of a half period $T/2$, the atoms in $|1,0\rangle$ are transferred to $|2,0\rangle$ by a resonant mw pulse. A subsequent rf π pulse transfers only the atoms in the symmetric superposition from $|1, \pm 1\rangle$ to $|1,0\rangle$. In this way, we separate the symmetric superposition that is now in $|1,0\rangle$ from the non-symmetric atoms in $|1, \pm 1\rangle$.

Because for this project the state-selective rf transfer (Section 5.3) was not yet in operation, the rf pulse on $F = 1$ at the same time triggers a transfer in $F = 2$ as the two hyperfine manifolds have similar linear Zeeman shifts. The effect of this rf pulse, resonant to $F = 1$, on $F = 2$ is shown in Figure 6.9. Calibration factors v_i are later employed to estimate the total atom number and the number of atoms in $|2,0\rangle$ before the rf pulse.

The remaining atoms in $|2,0\rangle$ are now coupled with $|1,0\rangle$ by an mw $\pi/2$ pulse to map the phase onto the population difference. Finally, the non-symmetric atoms in $|1, \pm 1\rangle$ are transferred to $|2, \pm 1\rangle$ by two resonant mw pulses. This step is necessary because our detection system does not distinguish between $F = 1$ and $F = 2$. Since both hyperfine manifolds are occupied in our scheme, we decide to only detect in $F = 2$. We thus have to

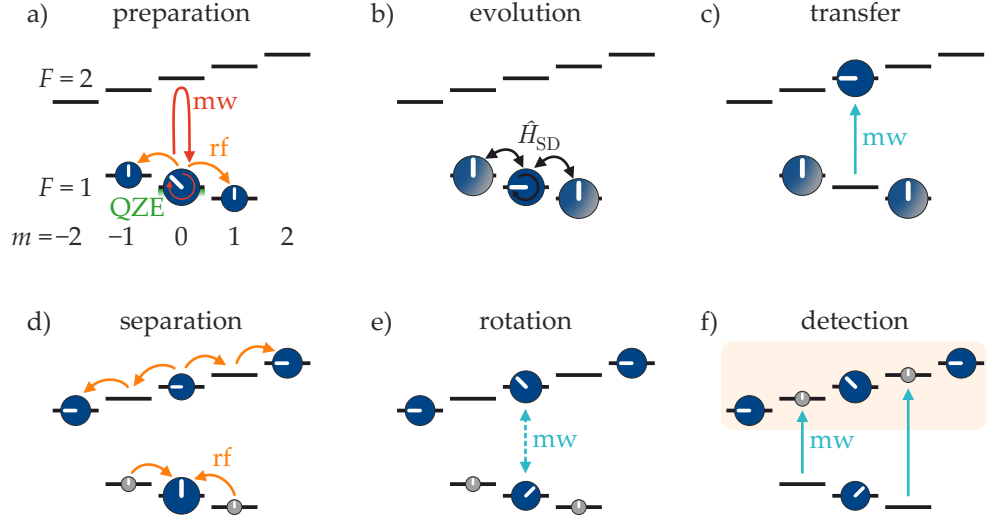


Figure 6.8: Scheme for a measurement of the interferometric order parameter with reduced fluctuations. The relative populations are indicated by the size of the spheres and the relative phase by little clock hands. Blue color depicts the symmetric and gray non-symmetric states. Solid arrows correspond to transfer, dashed arrows to a $\pi/2$ pulse. In (f), the orange area indicates that only $F = 2$ is detected.

transfer all modes that contain useful information to $F = 2$. In the end, we measure the population of five Zeeman states in $F = 2$ that are given by

$$N_{\pm 2} = n_0 v_{\pm 2} N, \quad (6.4)$$

$$N_{\pm 1} = \frac{1 - n_0}{2} \sin^2(\beta) N, \quad (6.5)$$

$$N_0 = \frac{1}{2} (v_0 n_0 + (1 - n_0) \cos^2(\beta)) N \quad (6.6)$$

$$+ \sqrt{v_0 n_0 (1 - n_0)} \cos(\beta) \sin(\varphi) N \quad (6.7)$$

with the calibration factors v_i , the mixing angle β and the relative population n_0 after phase evolution for $T/2$. The value of n_0 has to be measured by an independent measurement.

The total atom number N can be estimated using Equation 6.4 as

$$N = \frac{N_{+2} + N_{-2}}{n_0 (v_{+2} + v_{-2})}. \quad (6.8)$$

From the atoms in the non-symmetric superposition, stored in $|2, \pm 1\rangle$, and Equation 6.5 we retrieve the mixing angle β with

$$\sin^2(\beta) = \frac{N_{+1} + N_{-1}}{(1 - n_0) N}. \quad (6.9)$$

Now combining these findings with Equation 6.7, an expression including the relative phase φ can be obtained, which is

$$|\sin(\varphi)| = \frac{|(N_0 + \frac{1}{2}(N_{+1} + N_{-1})) / N + \frac{1}{2}((1 - v_0)n_0 - 1)|}{\sqrt{v_0 n_0 (1 - n_0) - (N_{+1} + N_{-1}) / N}}. \quad (6.10)$$

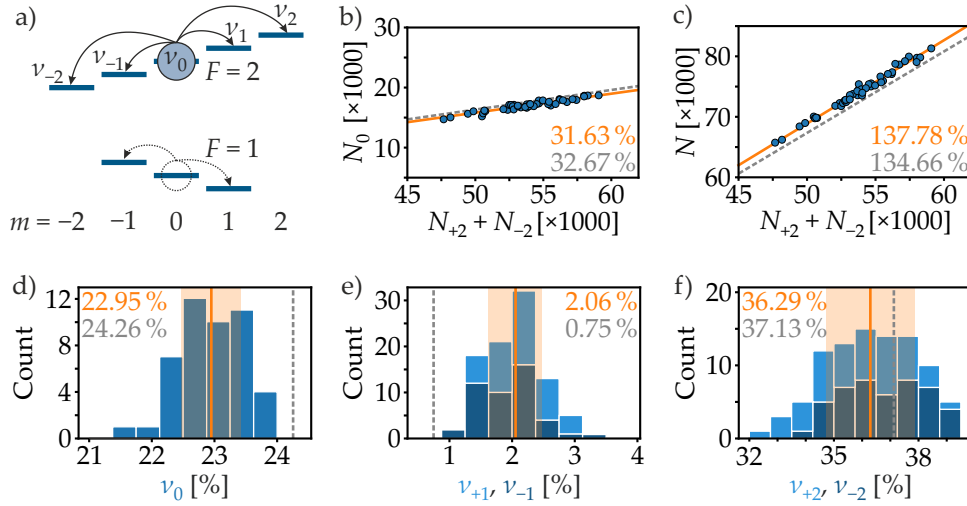


Figure 6.9: Calibration of rf transfer in $F = 2$. (a) Illustration of the procedure. With all atoms in $|2, 0\rangle$, an rf pulse resonant to $F = 1$ is applied. This results in transfer to all modes in $F = 2$, indicated by the factors $v_i = N_i/N$. (b-c) Dependency of the atoms in $|2, 0\rangle$ (b) and the total atom number (c) on the number of atoms in $|2, \pm 2\rangle$ after the rf pulse. Blue dots are measurement data, orange solid lines linear fits and gray dashed lines theory predictions. Numbers indicate the slope of a linear fit. (d-f) Histograms for the different modes after the rf pulse. Plotted is the occurrence against the relative number of atoms in the corresponding modes $|2, 0\rangle$ (d), $|2, \pm 1\rangle$ (e) and $|2, \pm 2\rangle$ (f). Vertical orange lines depict mean values, orange shading two standard deviations and gray dashed lines theory expectations. The theory values are calculated by assuming a generalized Rabi frequency with detuning $\delta = 2\pi \cdot 2\text{kHz}$ due to different linear Zeeman shifts in $F = 1$ and $F = 2$.

This equation therefore defines an order parameter to distinguish ESQPTs at a half period with $|\sin(\varphi = 0)| = 0$ in the BA' phase and $|\sin(\varphi = \pi/2)| = 1$ in the P' and TF' phases. Note that we cannot access the sign of $\sin(\varphi)$. Due to this phase ambiguity, the measurement outcome is therefore not only the atoms in the symmetric superposition $|g\rangle$ with $\beta = 0$, but also those with a phase shift of $\beta = \pi$. This is a reason why the measurements are performed at $T/2$. At the period T , we would retrieve $|\sin(\varphi)| = 0$ for all phases.

Figure 6.10 shows a measurement of $n_0(t)$, the relative population $n_{0,y}(t)$ obtained by the above measurement scheme and an evaluation of Equation 6.10. Because the fraction of atoms in the non-symmetric state is extracted by our scheme, we can post-select on experimental realizations with a certain minimum amount of atoms in the symmetric state. This collapses the data onto the theoretical predictions. Residual noise contributions can be attributed to drifts and fluctuations in the QZE and the total atom number.

The phase ambiguity results in the same order parameter of $|\sin(\varphi)| = 1$ for the P' and the TF' phases. This is, however, not a problem because those two phases are not adjacent and always have the BA' phase in between. If necessary, one can nevertheless distinguish the phases by tracking the initial evolution of the phase that goes into the positive direction for the one and the negative direction for the other phase.

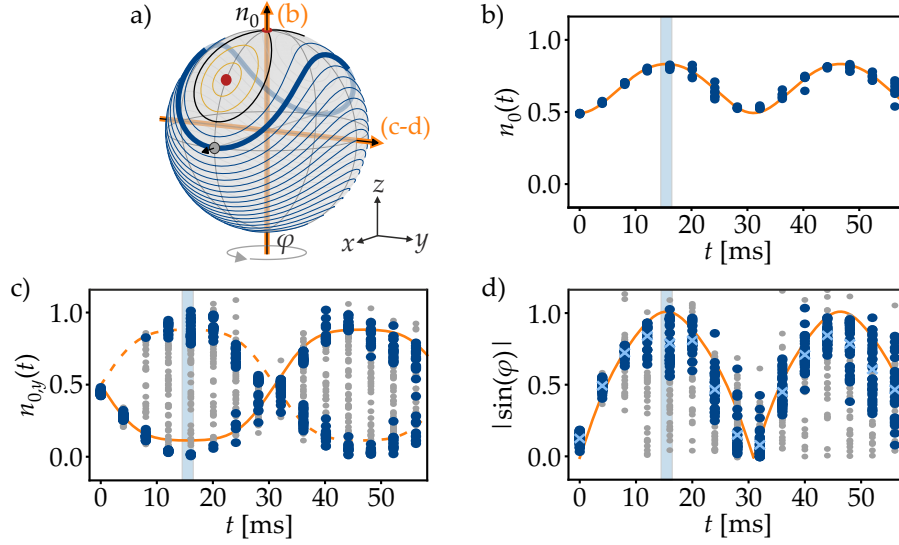


Figure 6.10: Measurement of the interferometric order parameter with reduced fluctuations. (a) Illustration of the trajectory to measure on the Bloch sphere (thick blue line). Measurement directions are indicated by orange arrows. (b-d) Measurements of the population oscillation (b), the projection along the y axis (c) and the interferometric order parameter (d). Dots correspond to measurement data, solid orange lines to expected signals and the light blue bar to the half period $T/2$. For (c-d), dark blue dots indicate realizations with minimum fraction of 65% of the $|\pm 1\rangle$ atoms in the symmetric state and gray dots with less. In (c), the dashed orange line is the expected signal with a phase shift of π . Light blue crosses in (d) signalize mean values of the dark blue dots only.

With this order parameter, we can now map the excited-state quantum phase diagram. From every measurement as described above, we extract an averaged value of $|\sin(\varphi)|$ at the half period $T/2$ for a certain excited state $(q/|\Omega|, \eta^*)$. Depending on its value, ranging from 0 (BA') to 1 (P' and TF'), we can classify the excited state into the corresponding quantum phase. To systematically investigate the excited-state quantum phase diagram, we first keep the initial population and phase fixed and only vary $q/|\Omega|$ (Figure 6.11). The transition from TF' over BA' to P' becomes clearly visible with phase transitions close to the theoretical predictions of $q/|\Omega| = \pm 1$. Because the mixing angle is in principle already included in the order parameter (Equation 6.10), a post-selection onto a maximum number of non-symmetric atoms just slightly changes the measurement result, indicated by gray bars in Figure 6.11 d). Those gray bars present the measurement outcome for different post-selections on the minimum fraction of atoms in the symmetric state in all $|\pm 1\rangle$ atoms after the evolution. This fraction ranges from 0 – 100% and the colored dots present $N_g/N_{\pm 1} > 65\%$, i.e., all experimental runs with more than 65% of the $|\pm 1\rangle$ atoms being in the symmetric superposition $|g\rangle$ after the evolution.

The variation of $q/|\Omega|$ already crosses ESQPTs. However, it is also possible to keep the QZE control parameter constant and vary only the excitation energy η^* to drive such a transition. The first option to vary η^* is the initial population $n_0(0)$ (Figure 6.12 a,c). A clear transition between BA' and TF'

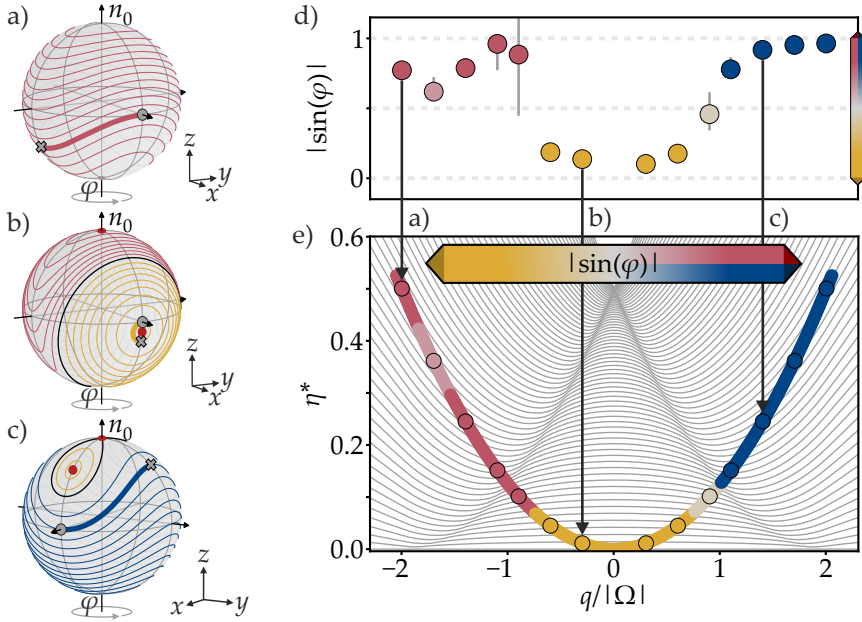


Figure 6.11: Order parameter measurement for a variation of the QZE. (a-c) Illustration of three exemplary trajectories on the Bloch sphere. They correspond to $q/|\Omega| = -2$, $q/|\Omega| = -0.3$ and $q/|\Omega| = 1.4$. Gray circles indicate the starting point and gray crosses the final point after one half period $T/2$. (d) For $n_0(0) = 0.5$ and $\varphi(0) = 0$ the order parameter $|\sin(\varphi)|$ is measured at $T/2$ for different values of $q/|\Omega|$. The color of every data point is associated with the value of $|\sin(\varphi)|$ according to the color bar. Gray lines indicate different minimum fractions of atoms in the symmetric superposition and the actual dots correspond to a minimum fraction of 65%. The three states from (a-c) are highlighted. (e) Phase diagram with the measurement from (d) included. The gray lines are every 500th eigenvalue for $N = 70\,000$ atoms. Phase transitions are located at regions of high density of states. Every data point from (d) corresponds to a circle in this diagram and the colored line is a guide to the eye.

is visible in this case, where the change in initial population distribution changes the evolution of the state drastically at some point. For the data points with low initial $n_0(0)$, problems occur because the relative population after the evolution is very small with $n_0(T/2) < 0.1$. This results in unreliable estimation of atom numbers in above equations and therefore data that cannot be evaluated for the determination of excited-state quantum phases. In the discussion of this chapter, a method is presented to circumvent this problem. The instability can also be seen in the large gray bars for those values that present the post-selection on different minimum fraction in the symmetric superposition. We therefore exclude those data points in the phase diagram as our measurement method is inconclusive there.

The excitation energy can also be changed by the initial phase $\varphi(0)$. Our order parameter, however, is not applicable in the presented form because it relies on starting with a fixed $\varphi(0) = 0$. Just preparing a state with fixed $q/|\Omega|$ and $n_0(0)$ and varying $\varphi(0)$ could of course also end in a phase transition, but we could not determine it with a phase measurement after half an oscillation period. This does not alter the universality of our parameter, as

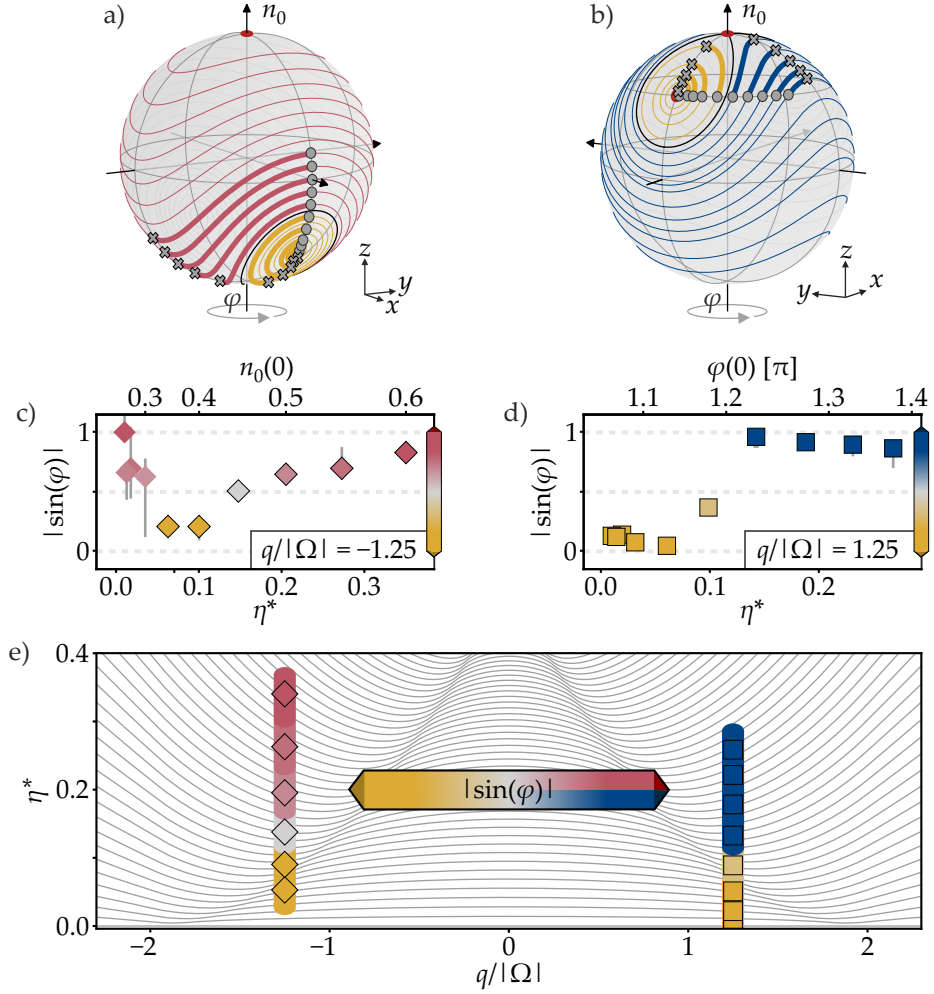


Figure 6.12: Order parameter measurement for a variation of the excitation energy. (a-b) Bloch spheres for $q/|\Omega| = -1.25$ (a) and $q/|\Omega| = 1.25$ (b). Trajectories that are measured in (c-d) are highlighted as thick lines with initial (circles) and final (crosses) points of the evolution. (c-d) Measurement of the interferometric order parameter for a variation of η^* in terms of $n_0(0)$ (c) and $\varphi(0)$ (d). Gray lines are deviations of $|\sin(\varphi)|$ with respect to the minimum number of atoms in the symmetric superposition $|g\rangle$. (e) Phase diagram with measurements (c-d) included as diamonds and squares, respectively. Colored lines are a guide to the eye. Inconclusive data points for $\eta^* < 0.05$ in (c) are excluded from the phase diagram.

every trajectory and therefore any point in the phase diagram can be reached with $\varphi(0) = 0$.

We can approximate the order parameter by a slightly different method to be applicable for a variation of the phase $\varphi(0)$ (Figure 6.12 b,d). For this method, we need to vary the phase at a population $n_0(0)$ that corresponds to the non-trivial stationary point of the sphere. Choosing this value for $n_0(0)$, a variation of $\varphi(0)$ occurs mostly orthogonal to the trajectories, at least close to the phase transition. For a chosen value of $\varphi(0)$, we then measure the final phase $\varphi(T/4)$ after one quarter of an oscillation period. After this evolution time, all the states in the BA' phase will end with a phase of $\varphi(T/4) = 0$, i.e. $|\sin(\varphi)| = 0$. States in the P' and TF' phases will, on the other hand, evolve

to $\varphi(T/4) = \pi/2$ and therefore $|\sin(\varphi)| = 1$. For trajectories further away from the phase transition in the P' and TF' phases, the phase value $\varphi(T/4)$ will be larger than $\pi/2$ and therefore $|\sin(\varphi)|$ will decrease again at some point. Nevertheless, the transition can be pinpointed by this approximated order parameter. This method only gives conclusive results for a variation of $\varphi(0)$ across the separatrix where both trajectories run in the same direction, i.e., in the positive phase direction for P' and the negative direction for TF', respectively. One could also scan both directions and the point where $|\sin(\varphi)|$ jumps from 0 to 1 gives the transition, including the information whether it is the P' or the TF' phase.

Combining the variations of $q/|\Omega|$, $n_0(0)$ and $\varphi(0)$, we achieve the phase diagram presented in Figure 6.13. In this diagram, we mapped seven different paths. Five of those result from a variation of $q/|\Omega|$ (which is also an indirect variation of η^*) and two from a direct variation of η^* , where one of them varies $n_0(0)$ and one $\varphi(0)$. We furthermore include obtained values from the iterative measurements. The phase diagram clearly reflects the three expected excited-state quantum phases with the TF', BA' and P' phases from left to right. Iterative measurements contribute clear phase mapping at several chosen points in the diagram, while the determination of phase transitions can be obtained from the measurements with separated symmetric

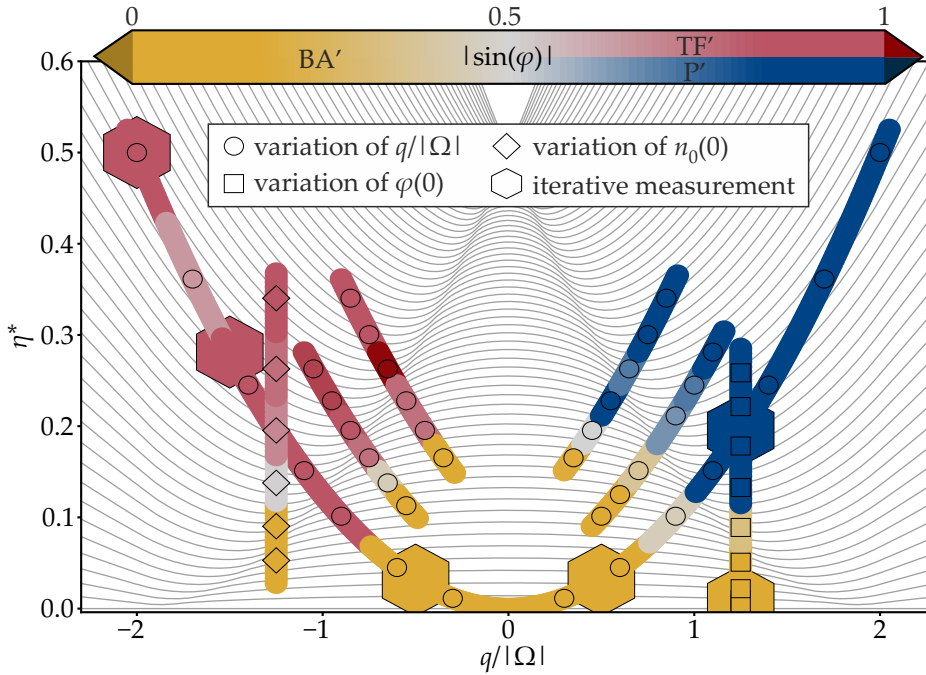


Figure 6.13: Conclusive excited-state quantum phase diagram. In the background, every 500th eigenvalue is plotted for $N = 70\,000$ atoms. Symbols represent measurement data and colored lines are meant for illustration purposes of the measurement paths. Color corresponds to the value of an interferometric order parameter from red (TF') over yellow (BA') to blue (P'). Large hexagons are extracted from iterative measurements, as presented in Section 6.4.1. Variations of $q/|\Omega|$ (circles), $n_0(0)$ (diamonds) and $\varphi(0)$ (squares), as presented in this chapter, are indicated by smaller symbols.

contribution presented in this section. We observe phase transitions for every measurement path, in particular also for those that vary the excitation energy η^* only.

Compared to the theoretical values for the phase transition lines, we observe small differences. Our experimentally determined transition points are mainly shifted inwards. We assume two reasons responsible for this. First of all, we do not measure the actual atom number N , but only estimate it. The evaluation of $|\sin(\varphi)|$ can therefore fluctuate for different experimental realizations, also above 1, but never below 0. Taking the average thus preferably increases the value of $|\sin(\varphi)|$ and therefore the BA' phase seems smaller.

The second argument has a fundamental reason. We assume that the atomic cloud can be entirely described within the single-mode approximation. If we, however, assume the BEC to have a Thomas-Fermi profile, its density is smaller at the borders. Because the spin dynamics interaction strength Ω depends on the density via $\Omega \propto N^{2/5}$ (Equation 4.5), it is not constant over the spatial extent of the cloud, but at least decreases rapidly at the borders. A vanishing $|\Omega|$ corresponds to $|q/\Omega| \gg 2$, such that there is a small contribution to the P' or TF' phase, even if the main part of the cloud corresponds to BA'. A thorough analysis without assuming the single-mode approximation indeed results in small inward shifts of the phase boundaries [60].

The determination of $|\sin(\varphi)|$ was possible for a large range of QZE values. Measurements for $q/|\Omega| > 0$, however, seemed to give cleaner results than for $q/|\Omega| < 0$ (Figure 6.11 d). On the one hand, this can be attributed to an imperfect calibration of the QZE. Considering the initial rf π pulse when calibrating $q/|\Omega| = -1$, magnetic field fluctuations or incomplete rf transfer lead to remaining atoms in $|0\rangle$ that act as a seed for the dynamics. This makes the Gaussian for $q/|\Omega| = -1$ non-symmetric, leading to shifted values for the correct detuning. Moreover, the preparation of excited states is done in the same way for positive and negative QZE, i.e., starting with the state $|0\rangle$. However, for $q/|\Omega| < 0$ this results in highest excited states that are then reduced in energy by the adjustment of η^* . In this case, a better option for future investigations might be to start with all atoms in $|g\rangle$ using an initial rf π pulse and then start the preparation with an adjustment of $q/|\Omega|$. This ensures that the state is initially close to the ground state.

6.5 DISCUSSION

In the previous chapter, we have thoroughly investigated excited-state quantum phases. Using our preparation method, we can explore any point in the phase diagram. While the population oscillations resemble the expected trajectories very well, the phase signal shows fluctuations that are attributed to shot-to-shot deviations of the magnetic field. Nevertheless, we presented three methods to measure ESQPTs. An iterative method employs the signal that is still visible for very short evolution times, thanks to our low magnetic field fluctuations and large spin dynamics interaction strength. The second method utilizes the boundaries of the fluctuations to determine the

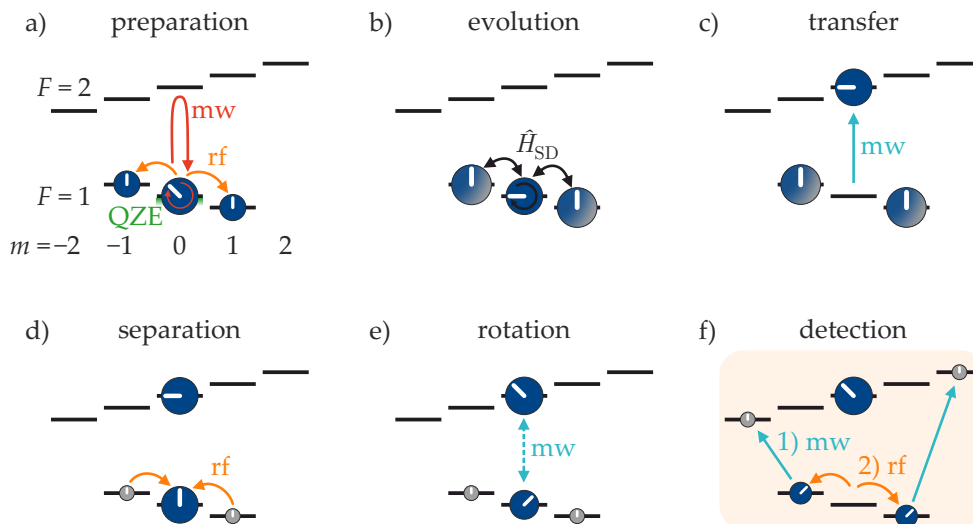


Figure 6.14: Sequence to extract the order parameter using state-selective rf transfer. Symbols and arrows as in Figure 6.8. Steps (d) and (f) differ from the original scheme due to a state-selective rf transfer in both steps. In the last step, atoms in $|1, \pm 1\rangle$ are transferred to $|2, \pm 2\rangle$ and then $|1, 0\rangle$ is transferred to $|1, \pm 1\rangle$ by a state-selective rf π pulse. Now both $F = 1$ and $F = 2$ are detected, because every $|m|$ state is only occupied in one of the manifolds.

phase transition, but is not in general capable of distinguishing excited-state quantum phases. Finally, a scheme that separates the desired symmetric superposition states from others facilitates a detailed investigation of quantum phases and transitions of excited states.

Quantitative deviations of the mean-field phase diagram and our experimental results can be explained by technical and fundamental arguments. On the technical side, improvements to our experimental apparatus could circumvent problems. One improvement is the state-selective rf transfer that has now already been implemented (Section 5.3). This technique would make the rf calibration (Figure 6.9) unnecessary because the intended rf π pulse would only transfer the symmetric portion of $|1, \pm 1\rangle$ to $|1, 0\rangle$ and leave atoms in $|2, 0\rangle$ untouched. A proposed scheme is presented in Figure 6.14. After the mw $\pi/2$ pulse in step (e), the atoms in $|1, \pm 1\rangle$ could be transferred to $|2, \pm 2\rangle$ by resonant mw radiation and a state-selective rf pulse could transfer $|1, 0\rangle$ to $|1, \pm 1\rangle$. In this way, every state with quantum number $\pm m$ is only occupied in either $F = 2$ or $F = 1$, such that both manifolds can be detected simultaneously. An estimation of the total atom number N by an independent measurement of $n_0(T/2)$ (Equation 6.4) would not be necessary then because all occupied states are detected. This might improve the problem due to very low $n_0(T/2)$ after the evolution because N would not rely on this any more.

Another improvement could be an independent detection of $F = 2$ and $F = 1$. This would reduce the number of required pulses because detection could already happen after step (e). Such a detection requires to take another camera picture. For a better detection noise, it might be beneficial to take three additional pictures for individual determination of beam and back-

ground counts. Although well suited for the presented experiments, this technique probably causes more detection noise than a single imaging step.

Independent detection of the two hyperfine manifolds furthermore opens up the possibility of simultaneously detecting conjugate observables [154]. For this technique, half of the atoms are transferred to $F = 2$ after the evolution. States in $F = 2$ are then coupled by a $\pi/2$ rf pulse to read out the phase $\varphi(t)$ and states in $F = 1$ are just read out for the population value $n_0(t)$. This would make the simultaneous detection of n_0 and φ possible in the same experimental realization. Of course, the selection of atoms in the symmetric superposition is not possible with this technique because population cannot be transferred any more between the hyperfine manifolds. However, it might still be a helpful tool, e.g., for the iterative measurements.

Deviations in the phase diagram might also occur because of effects beyond the single-mode approximation. This is very interesting because in the ground state no such effects are expected [59]. Excited states might thus be employed for investigations of effects beyond this approximation. Further thoughts on this can be found in the following outlook of this thesis.

OUTLOOK

Over the last years, research concerning quantum phase transitions in a multitude of experimental systems has gained increasing interest. Phase transitions of excited states have been investigated from a theoretical perspective [36, 47–51, 155] and they became apparent in some experimental systems [38–41, 105]. However, a thorough mapping of an excited-state quantum phase diagram by an appropriate order parameter was not achieved so far.

In this work, we have investigated the quantum dynamics of excited states in a spin-1 BEC. From theoretical predictions, three phases with different dynamical features are expected. While population oscillations have been clearly visible, the phase signal, however, was fluctuating due to a varying detuning between magnetic field and rf signals from shot to shot. Nevertheless, three experimental schemes were presented that enable the measurement of excited state quantum phases and their transitions. Employing an interferometric order parameter in a scheme selective to vanishing magnetic field fluctuations, ESQPTs were observed for a variation of two control parameters, the QZE $q/|\Omega|$ and the excitation energy η^* . The crossing of a phase transition by a variation of the energy only is a unique feature of ESQPTs that was presented in this work for the first time. Finally, this method resulted in the up to now elusive mapping of a conclusive excited-state quantum phase diagram.

On a technical side, a new mw and rf system was presented. Besides very low noise features that allow for Heisenberg-limited metrology, this system facilitates advanced techniques to engineer pulses. Amplitude-shaped pulses reduce transfer to off-resonant transitions and composite sequences might cancel the effect of drifts in the detuning or amplitude. Finally, state-selective rf transfer has been implemented that further enhances the control of the atomic spin states.

Our findings are now extended into two directions. On the one hand, the knowledge and technical improvements can be employed for the generation of entangled states for quantum-enhanced metrology. To this end, it is described how the generation of entanglement can be understood in the picture of excited coherent states. It is furthermore presented how the technique of state-selective rf transfer facilitates the creation of spin-squeezed states in magnetically insensitive modes. On the fundamental side, fascinating features have been explored in this work that deserve further investigation. In particular, it might be interesting to leave the single-mode approximation on purpose and look at spatial features of excited states. A rough idea is presented to map the excited-state quantum phase diagram from internal states into a spatial distribution.

7.1 QUANTUM DYNAMICS UTILIZED FOR METROLOGY

An interesting non-classical feature that can be explored at ultra-low temperatures is entanglement. BECs are for example studied for intriguing many-body quantum effects like spatially separated entanglement [58, 156, 157], Einstein-Podolsky-Rosen steering [158, 159] or Bell correlations [160]. For a detailed description, consultation of Fadel [161] is recommended.

Entanglement also presents a valuable resource that has the potential to enhance quantum metrology, e.g., mw and optical clocks or inertial sensors [162]. In spin-1 BECs, entanglement can be generated by spin-changing collisions. Starting with all atoms in $|0\rangle$, short evolution and adequate level shifts result in the two-mode squeezed vacuum state [89, 158, 163, 164] that has already been employed to improve an atomic mw clock [89]. Longer evolution times lead to a large population in $|\pm 1\rangle$ that can be understood as a superposition of twin-Fock states [65]. The generation of twin-Fock states is also possible via an adiabatic passage that transfers a large fraction of the atoms into the $|\pm 1\rangle$ states [99] and also for such states, metrological gain was reported [100, 165].

These states are created by quantum dynamics that is beyond the mean-field approximation. Nevertheless, it can be understood in the framework of mean-field trajectories on the Bloch sphere that was introduced in this thesis. Recently, Muñoz-Arias, Deutsch, and Poggi [166] proposed a framework to predict the generation of metrologically useful quantum states using a semiclassical phase space description similar to the one employed in this thesis. In the following, the mean-field description on the Bloch sphere is advertised as a tool to describe the generation of entangled states.

As an example, the generation of a spin-squeezed state is presented in Figure 7.1. Non-classical dynamics occurs in particular at the phase transitions, i.e., close to the separatrix in the Bloch sphere picture. An initial coherent state in $|0\rangle$ is located on the north pole, i.e., directly on the separatrix for $q/|\Omega| = 1$. For short evolution times, the squeezing generation can be depicted on a plane orthogonal to the mean spin direction. The evolution of the initial state is now described by quadrature squeezing with strength Ωt and a squeezing angle of $\varphi = \pi/4$ for the symmetric quadrature [64]. This dynamics results in a two-mode squeezed vacuum state with reduced fluctuations in one direction at the cost of larger fluctuations in the orthogonal direction. The squeezing is often characterized as the variance reduction compared to a coherent spin state with $\text{var}(S_z^{\text{CSS}}) = N/4$ [167, 168],

$$\zeta^2 = \frac{4 \text{var}(S_z)}{N}, \tag{7.1}$$

that indicates a spin squeezed state for $\zeta^2 < 1$. Note that the symmetric subspace is assumed here because we deal with indistinguishable bosons. This means that all states have maximum spin and are therefore located on the surface of the Bloch sphere.

The squeezing generation may leave the population in $|0\rangle$ nearly untouched and only transfers a small amount of less than 10 atoms to the

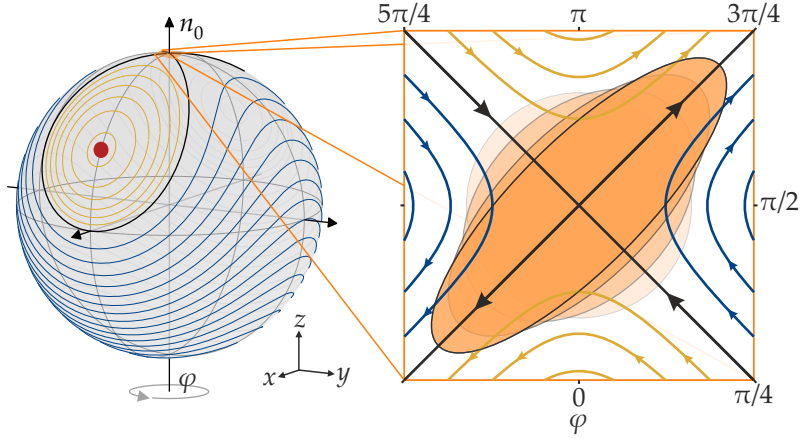


Figure 7.1: Generation of squeezed states. The left side shows a Bloch sphere with $q/|\Omega| = 1$ and the right side a local approximation of the north pole as a plane orthogonal to the z axis. An initial coherent state (light orange in the background) is deformed by the action of the Hamiltonian, represented by arrows. During the evolution time the state is squeezed, as indicated from light to dark orange color. The area of the ellipses corresponds to the respective quantum fluctuations. Maximum fluctuations occur along an angle of $3\pi/4$, such that a rotation about an axis with this angle rotates the minimum fluctuations onto the equator.

side modes. For longer evolution times beyond the undepleted pump approximation, more atoms can nevertheless be transferred to ± 1 along the separatrix. Such a procedure is employed to generate twin-Fock states via quench dynamics. This illustration also provides an intuitive understanding why a small seed, i.e., some atoms initially in the $|\pm 1\rangle$ states, leads to faster dynamics [169]. At the separatrix (the phase transition), the dynamics is slowest (Section 6.2). Being slightly off the separatrix using a small initial rf transfer therefore reduces the necessary evolution time. However, this may come at the cost of diminished variance reduction.

The generation of twin-Fock states by an adiabatic ramping through quantum phase transitions starts in the polar ground state with $n_0 = 1$. Subsequently, the QZE $q/|\Omega|$ is carefully decreased, such that the state always follows the stationary point on the Bloch sphere, which presents the ground state of the system. It reaches the TF' phase, where the ground state is the highly entangled twin-Fock state. This directly resembles the order parameter of ground-state quantum phases (Section 3.2).

Finally, also advanced schemes for entanglement generation, such as stationary spin squeezing via a double-quench method [170, 171] can be understood and reconstructed using this representation.

All those generated states, however, have the problem that they suffer from sensitivity to magnetic field fluctuations because they are partially created in modes $|1, \pm 1\rangle$. For the application in quantum-enhanced metrology, it would be desirable to generate entanglement in the clock states $|1, 0\rangle$ and $|2, 0\rangle$. Figure 7.2 presents a scheme that employs a state-selective rf transfer to create a spin-squeezed state in magnetically insensitive states. The atoms are initially prepared in $|1, 0\rangle$, where spin dynamics is activated for a short amount of

OUTLOOK

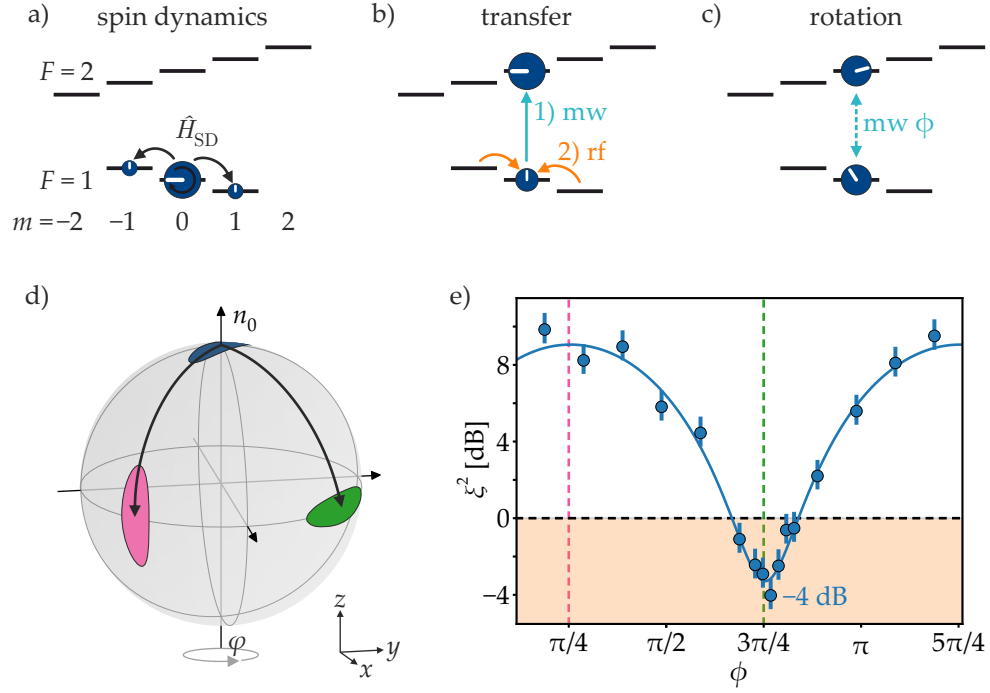


Figure 7.2: Tomography of a spin-squeezed state. (a) Initial spin dynamics is applied for 55 ms at $q/|\Omega| = 1$. (b) The first transfer pulse brings the atoms from $|1, 0\rangle$ to $|2, 0\rangle$ by resonant mw radiation. Secondly, a state-selective rf π pulse transfers the two-mode squeezed state into $|1, 0\rangle$. (c) An mw $\pi/2$ pulse rotates the state onto the equator. Depending on the adjusted phase ϕ , the state rotates about different axes. In the end, another state-selective rf pulse is employed (not shown) to transfer atoms from $|1, 0\rangle$ to the side modes because $|1, 0\rangle$ and $|2, 0\rangle$ cannot be distinguished in the detection. (d) Representation of the final rotation on the Bloch sphere. For an mw phase of $\phi = 0$, the state rotates about the x axis ($\phi = 0$). When the rotation axis has an angle of $\phi = \pi/4$ (pink), the state ends in upright position with maximum fluctuations for a projection onto the z axis. For $\phi = 3\pi/4$ (green), the resulting state has minimum fluctuations for a measurement of n_0 . (e) Measurement of reduced fluctuations in the fraction n_0 depending on the phase of the mw rotation pulse. Dots indicate the measured squeezing parameter ξ^2 and error bars are given as $\sqrt{2/(k-1)} \xi^2$ with the number of samples k [164]. The blue line is a sinusoidal fit for the minimum and the horizontal dashed black line the theoretical standard quantum limit. The orange area indicates the region of spin-squeezed states. Vertical dashed pink and green lines correspond to the rotation angles presented in (d). For the x axis, a phase of 0.312π has been subtracted because the state evolved for 2.4 ms at a detuning of 65 Hz (QZE) before the rotation pulse. Measurement results were kindly provided by Christophe Cassens.

time by mw dressing set to resonance $q = |\Omega|$ (Section 2.1.3). Subsequently, atoms from $|1, 0\rangle$ are transferred to $|2, 0\rangle$ by mw radiation. A state-selective rf pulse then brings one mode of the two-mode squeezed state into the $|1, 0\rangle$ mode. This can be understood by a basis change from $|\pm 1\rangle$ (two-mode squeezed state) to the symmetric and antisymmetric combinations that reflect two single-mode squeezed states, from which the symmetric combination is transferred by the rf pulse. So-called spin noise tomography [64] of this state is done by applying an mw $\pi/2$ pulse resonant to the clock transition

with variable phase ϕ . On the Bloch sphere, this corresponds to 90° rotations about different axes depending on ϕ . Experimentally, a 4 dB reduction in variance is obtained compared to a coherent spin state for $\phi = 0.77 \pi$. The generated entanglement in magnetically insensitive states can now be implemented, e.g., in an atomic mw clock or even in inertial sensing using Raman transitions to transfer momentum.

Zhou et al. [172] proposes a determination of ESQPTs using the quantum Fisher information in form of a time-reversal protocol. Such protocols are known from quantum enhanced sensing [173–175]. As this scheme is very sensitive to variations in $q/|\Omega|$, it could in principle also be employed for sensing. However, for such experimental realizations, the remaining parameters like the dressing frequency or the antenna position have to be well-controlled. This scheme nevertheless further combines the realm of ESQPTs and quantum sensing and in this way shows potential research directions in this field.

7.2 SPATIAL EXCITED-STATE QUANTUM PHASE TRANSITIONS

A different research direction extends the concept of ESQPTs beyond a single spatial mode. As we have seen, the assignment to a quantum phase depends on the QZE $q/|\Omega|$ and the excitation energy η^* . In our work, the mapping of a phase diagram was achieved in a single spatial mode with a single pair of values $(q/|\Omega|, \eta^*)$ in every measurement. If we could, however, add a dependency of $q/|\Omega|$ on the spatial position, the quantum phases would be mapped into space.

To observe spatially varying dynamics, a large expansion of the BEC in the camera plane would be necessary. There are several options to generate elongated atomic clouds. Using a standard crossed-beam optical dipole trap as in our setup, adjustment of beam powers and waists can result in longitudinal extension of $100 \mu\text{m}$ [77]. When just a single trapping beam traps the atoms, this can be further extended to 250 to $400 \mu\text{m}$ [77, 176]. An advanced technique would be the implementation of time-averaged optical potentials that can be created using acousto-optical modulators or deflectors and enable the creation of user-defined trapping potentials. [177, 178]. To create box potentials, there also exist experiments using blue detuned-laser beams as light sheets that repel atoms in a waveguide [179, 180].

The experimental scheme for a measurement of spatial ESQPTs could follow the one in Figure 6.14. After the preparation of an excited state by adjusting $q/|\Omega|$, $n_0(0)$ and $\varphi(0)$, the state would evolve and finally, $n_0(t)$ or $\varphi(t)$ is detected. The only, but very important difference would be that a variation of $q/|\Omega|$ over the extent of the cloud causes distinct dynamics for different parts of the BEC. Detecting the state thus results in a spatially dependent distribution of spin states.

For the single-mode case, the QZE was adjusted by the mw dressing field and the spin dynamics interaction strength was kept constant. For a spatially varying $q/|\Omega|$, there are now two options. The first option is a dependency of q on the position using a magnetic field gradient (Figure 7.3 a), e.g.,

OUTLOOK

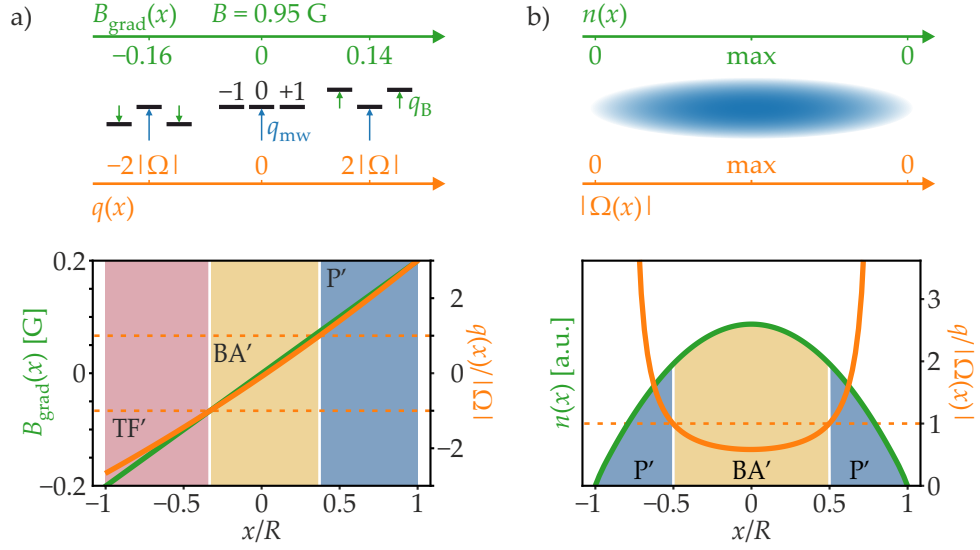


Figure 7.3: ESQPTs with spatial dependence. (a) Exploration of ESQPTs using a magnetic field gradient. In addition to a static homogeneous field of $B = 0.95 \text{ G}$, a gradient dB/dx is applied that locally changes the magnetic field by $B_{\text{grad}}(x)$. This results in a spatial variation of the magnetic-field contribution to the QZE q_B and, with a constant mw dressing q_{mw} , to a dependency of q on the position. The graph at the bottom shows expected quantum phases depending on the position (scaled with the Thomas-Fermi radius R) for an initial relative population of $n_0(0) = 0.5$. (b) Spatial ESQPTs utilizing the position-dependency of the density. The density of a BEC is smaller away from the center, in particular visible for elongated clouds. Because Ω directly depends on the density, it also varies with the position in the BEC. Expected phases are illustrated in the figure at the bottom for $n_0(0) = 0.5$. The density (green) resembles an inverted parabola with cloud radius R . Hence, $q/|\Omega|$ follows a curve with $1/(R^2 - x^2)$. At the edges of the cloud, when $|\Omega(x)|$ becomes smaller than q , the P' phase is visible. By adjustment of $q < 0$, the transition from TF' to BA' can also be observed.

generated by an additional pair of coils in anti-Helmholtz configuration. Such a gradient field dB/dx shifts the Zeeman states according to the spatial position and therefore changes q_B . The adjustment of q_{mw} could then shift the center of the cloud to $q = q_B + q_{\text{mw}} = 0$ and therefore the left and right side to $q < 0$ and $q > 0$, respectively. For $100 \mu\text{m}$ spatial extension of the cloud, a magnetic field gradient of $dB/dx = 40 \text{ G/cm}$ would shift the energy levels to $q/|\Omega| = -2.5$ and $q/|\Omega| = +3$ at the borders of the cloud. This value for dB/dx seems experimentally feasible and can be relaxed for larger clouds or if only one side of the phase diagram is explored.

Of course, this proposal has some challenges. First, the sensor-based magnetic field stabilization cannot work when the gradient is applied. This should not make this idea impossible because an independent stabilization of the current through the coils can be employed. Such a stabilization is not as good as the one using a magnetic field sensor, but should be sufficient. This is in particular the case for the presented scheme that is post-selecting realizations with negligible magnetic field fluctuations. A further solution to this problem would be a magnetic field shielding [181], but this requires

major work on the experiment. Another issue would be the linear Zeeman effect that is now also spatially dependent. Hence, mw and rf pulses would not be resonant on the entire cloud. When the gradient is just turned on for the evolution time, however, this is also not necessary. After the evolution, a scheme similar to Figure 6.14 could be applied.

A second option relies on the inhomogeneous density of the BEC due to the harmonic confinement. Because Ω is density-dependent, the ratio $q/|\Omega|$ varies in space for a large atomic cloud (Figure 7.3 b). For adequate adjustment of q and $n_0(0)$, there exist regions in the BEC that belong to different quantum phases due to the variation of $\Omega(x)$. In the center, there will always be the largest density, therefore maximum $\Omega(x)$ and minimum $q/|\Omega(x)|$. When different phases are visible, the inner phase is thus always BA'. The outer regions belong to the same phase because q does not change sign over the extent of the cloud. The P' and TF' phases can anyhow both be measured by adjusting q to positive and negative values, respectively. Simulations still have to be done to find regimes where the regions at the border of the cloud are not too small. The simulations would also reveal other important information, e.g., how large the visibility will be at the border, how sharp phase transitions will be and whether further effects beyond the single-mode approximation are expected.

Nevertheless, this approach is very interesting. In contrast to the variation of $q/|\Omega|$ by a magnetic field gradient, q would still be an adjustable control parameter in this case. Moreover, it does also not require additional magnetic fields that shift transition frequencies or prohibit the sensor stabilization. A fascinating particularity is the fact that the varying density is a spatial property of the many-body system itself, in contrast to an artificially applied magnetic field gradient that changes single atomic states. This research direction would therefore explore intrinsic dynamical properties of BECs in terms of excited-state quantum phases beyond the single-mode approximation.

APPENDIX

A.1 CALCULATION OF THE EIGENENERGIES

ESQPTs can be defined by a diverging density of states, or in other words, by a vanishing energy gap between neighboring excited states. To locate such vanishing energy gaps, energy eigenvalues of the underlying Hamiltonian are calculated as described in this section.

The Hamiltonian is given as in Equation 2.25 by

$$\begin{aligned} \hat{H}_{\text{SD}} = & q (\hat{N}_1 + \hat{N}_{-1}) \\ & + \frac{\Omega}{N} \left[\hat{a}_0^\dagger \hat{a}_0^\dagger \hat{a}_1 \hat{a}_{-1} + \hat{a}_1^\dagger \hat{a}_{-1}^\dagger \hat{a}_0 \hat{a}_0 + \left(\hat{N}_0 - \frac{1}{2} \right) (\hat{N}_1 + \hat{N}_{-1}) \right]. \end{aligned} \quad (\text{A.1})$$

To calculate the eigenvalues, we describe the system in the effective two-mode basis $|k, N - 2k, k\rangle = |k\rangle_{-1} \otimes |N - 2k\rangle_0 \otimes |k\rangle_1$ which has dimensionality $N/2 + 1$. This yields

$$\begin{aligned} \hat{N}_0 |k, N - 2k, k\rangle &= (N - 2k) |k, N - 2k, k\rangle \\ \hat{N}_{\pm 1} |k, N - 2k, k\rangle &= k |k, N - 2k, k\rangle \\ \hat{a}_0^\dagger \hat{a}_0^\dagger \hat{a}_1 \hat{a}_{-1} |k, N - 2k, k\rangle &= k \sqrt{(N - 2k + 1)(N - 2k + 2)} \\ & |k - 1, N - 2(k - 1), k - 1\rangle \\ \hat{a}_1^\dagger \hat{a}_{-1}^\dagger \hat{a}_0 \hat{a}_0 |k, N - 2k, k\rangle &= (k + 1) \sqrt{(N - 2k)(N - 2k - 1)} \\ & |k + 1, N - 2(k + 1), k + 1\rangle. \end{aligned} \quad (\text{A.2})$$

We rewrite the Hamiltonian as an energy density and scale it by the spin dynamics rate $|\Omega|$ to directly achieve values for the energy density η (Equation 3.6),

$$\hat{h} = \frac{\hat{H}_{\text{SD}}}{|\Omega| N}. \quad (\text{A.3})$$

This results in a tridiagonal matrix with elements $h_{i,k}$ given by

$$\begin{aligned} h_{i,k} = & \frac{1}{N^2} \left[\delta_{i,k} 2k \left(N \frac{q}{|\Omega|} - \left(N - 2k - \frac{1}{2} \right) \right) \right. \\ & - \delta_{i,k+1} (k + 1) \sqrt{(N - 2k)(N - 2k - 1)} \\ & \left. - \delta_{i,k-1} k \sqrt{(N - 2k + 1)(N - 2k + 2)} \right]. \end{aligned} \quad (\text{A.4})$$

Computationally, this can be solved in a fast way using the LAPACK function *ssterf* (available in *Python* via *scipy.linalg.lapack.ssterf*) that works for symmetric tridiagonal matrices.

A.2 DERIVATION OF THE FLUCTUATION BOUNDARIES

This section derives the boundaries for the measured fluctuations due to deviations in the magnetic field as observed, e.g., in Figure 6.4 and Section 6.4.2.

The ideal signal of such a measurement, i.e., a $\pi/2$ pulse after the evolution and therefore a projection onto the y axis, is given by

$$n_{0,y}(t) = \frac{1}{2} + \sqrt{n_0(t)(1-n_0(t))} \sin(\varphi(t)). \quad (\text{A.5})$$

As described in Feldmann [76], a deviation of the magnetic field alters the state before the closing $\pi/2$ pulse according to

$$|\psi\rangle \rightarrow e^{-i\beta\hat{D}/\hbar} |\psi\rangle \quad (\text{A.6})$$

with the mixing angle $\beta = -b_p \int_0^{T_{\text{ev}}} dt \Delta B(t)$, linear Zeeman coefficient $b_p = -702 \text{ kHz/G}$, evolution time T_{ev} , magnetic field fluctuations $\Delta B(t)$ and the magnetization \hat{D} . This results in the affected signal

$$n_{0,y}(t) = \frac{1}{2} \cos^2(\beta) + \frac{1}{2} n_0(t) \sin^2(\beta) + \sqrt{n_0(t)(1-n_0(t))} \sin(\varphi(t)) \cos(\beta), \quad (\text{A.7})$$

for which the minimum and maximum values should be calculated. With $x = \cos(\beta)$, one minimum is obtained for

$$\tilde{x} = -\sqrt{\frac{n_0(t)}{1-n_0(t)}} \sin(\varphi(t)) \quad (\text{A.8})$$

with value

$$n_{0,y}(t) = \frac{1}{2} n_0(t) \cos^2(\varphi(t)). \quad (\text{A.9})$$

The value \tilde{x} is mathematically not restricted to $|\tilde{x}| < 1$. Values at the borders $x = \pm 1$ are

$$n_{0,y}(t) = \begin{cases} \frac{1}{2} + \sqrt{n_0(t)(1-n_0(t))} \sin(\varphi(t)) & \text{for } x = 1, \\ \frac{1}{2} - \sqrt{n_0(t)(1-n_0(t))} \sin(\varphi(t)) & \text{for } x = -1. \end{cases} \quad (\text{A.10})$$

The global maxima and minima for $|x| \leq 1$ are therefore

$$n_{0,y}^{\text{max}}(t) = \frac{1}{2} + \sqrt{n_0(t)(1-n_0(t))} |\sin(\varphi(t))|, \\ n_{0,y}^{\text{min}}(t) = \begin{cases} \frac{1}{2} n_0(t) \cos^2(\varphi(t)) & \text{if } |\tilde{x}| < 1, \\ \frac{1}{2} - \sqrt{n_0(t)(1-n_0(t))} |\sin(\varphi(t))| & \text{else,} \end{cases} \quad (\text{A.11})$$

as presented in Equation 6.2.

A.3 SIGNAL IN THE FLUCTUATIONS FOR A VARIATION OF $q/|\Omega|$

In Section 6.4.2, the strong fluctuations in the phase signal have been utilized to observe a phase transition between the BA' and P' phases. As presented, this was done by a variation of the initial relative population $n_0(0)$ and in this way of the excitation energy η^* .

It is also possible to drive a phase transition by a variation of the QZE $q/|\Omega|$. In Figure A.1, such a measurement is presented with an initial population $n_0(0) = 0.4$ and initial phase $\varphi(0) = 0$.

The expected phase transition at $q/|\Omega| = 0.8$ is indeed observed in this measurement by vanishing fluctuations. However, the transition is not very exposed. It can be seen that the fluctuation for $q/|\Omega| \geq 0.8$ in (d) do not cover the entire allowed range. This could be the case because the accumulated

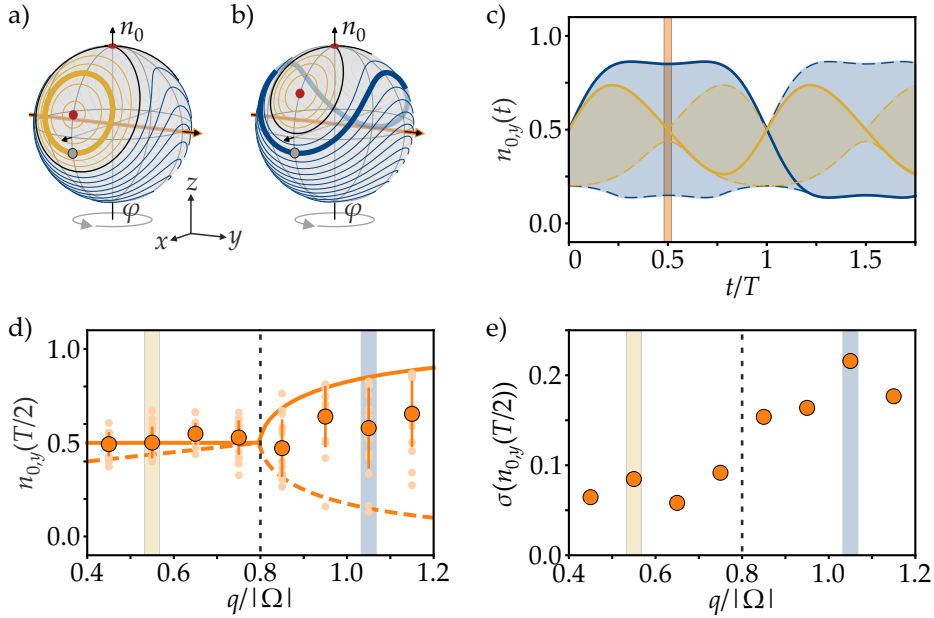


Figure A.1: Signal of a phase transition in the fluctuations for a variation of $q/|\Omega|$. (a-b) Bloch spheres for $q/|\Omega| = 0.55$ (a) and $q/|\Omega| = 1.05$ (b). Trajectories with $n_0(0) = 0.4$ are highlighted, each with $\varphi(0) = 0$. Starting points are indicated by gray circles. The measurements are performed as a projection onto the orange axis. (c) Theoretical simulations for $n_0(0) = 0.4$ and $|\Omega|/h = 11.5$ Hz. The blue (larger) curves belong to $q/|\Omega| = 1.05$ and the yellow (smaller) ones to $q/|\Omega| = 0.55$. Solid lines indicate the signal without magnetic field detuning, dashed lines and shading depict the boundaries including deviations in the magnetic field. At the orange shaded bar, the half period is reached. (d) At the calculated half period $T/2$, the population along the y axis is measured for different values of the QZE $q/|\Omega|$. Light orange dots indicate individual measurements, dark orange dots mean values and orange error bars the standard deviations. The blue and yellow shaded bars correspond to the curves in (c) and the trajectories in (a-b). Orange lines indicate the boundaries n_{\min} and n_{\max} . The dashed black line indicates the theoretically expected value for a phase transition at $q/|\Omega| = 0.8$. (e) Standard deviation of the measurement data in (d), depicted as orange dots, plotted against the QZE. Vertical lines as in (d).

phase due to magnetic field deviations is not yet large enough at $T/2$. It would therefore be a possibility to measure the fluctuations at $3T/2$, where the phase could be accumulated for a longer time and therefore the discrimination of the phases could be easier. This measurement shows the difficulty to obtain the critical value of the phase transition because a sharp discontinuity is not even expected in theory. Instead, a single point with zero fluctuations is expected, which is experimentally impracticable to measure.

BIBLIOGRAPHY

- [1] A. Einstein. "Quantentheorie des einatomigen idealen Gases." In: *Königliche Preussische Akademie der Wissenschaften. Sitzungsberichte* (1924), pp. 261–267.
- [2] A. Einstein. "Quantentheorie des einatomigen idealen Gases. Zweite Abhandlung." In: *Sitzungsberichte der Preussischen Akademie der Wissenschaften (Berlin). Physikalisch-mathematische Klasse* (1925), pp. 3–14.
- [3] S. N. Bose. "Plancks Gesetz und Lichtquantenhypothese." In: *Z. Physik* 26.1 (Dec. 1924), pp. 178–181. DOI: [10.1007/BF01327326](https://doi.org/10.1007/BF01327326).
- [4] K. B. Davis, M. O. Mewes, M. R. Andrews, N. J. van Druten, D. S. Durfee, D. M. Kurn, and W. Ketterle. "Bose-Einstein Condensation in a Gas of Sodium Atoms." In: *Phys. Rev. Lett.* 75.22 (Nov. 1995), pp. 3969–3973. DOI: [10.1103/PhysRevLett.75.3969](https://doi.org/10.1103/PhysRevLett.75.3969).
- [5] M. H. Anderson, J. R. Ensher, M. R. Matthews, C. E. Wieman, and E. A. Cornell. "Observation of Bose-Einstein Condensation in a Dilute Atomic Vapor." In: *Science* 269.5221 (July 1995), pp. 198–201. DOI: [10.1126/science.269.5221.198](https://doi.org/10.1126/science.269.5221.198).
- [6] R. Grimm, M. Weidemüller, and Y. B. Ovchinnikov. "Optical Dipole Traps for Neutral Atoms." In: *Advances In Atomic, Molecular, and Optical Physics*. Ed. by B. Bederson and H. Walther. Vol. 42. Jan. 2000, pp. 95–170. DOI: [10.1016/S1049-250X\(08\)60186-X](https://doi.org/10.1016/S1049-250X(08)60186-X).
- [7] D. M. Stamper-Kurn, M. R. Andrews, A. P. Chikkatur, S. Inouye, H.-J. Miesner, J. Stenger, and W. Ketterle. "Optical Confinement of a Bose-Einstein Condensate." In: *Phys. Rev. Lett.* 80.10 (Mar. 1998), pp. 2027–2030. DOI: [10.1103/PhysRevLett.80.2027](https://doi.org/10.1103/PhysRevLett.80.2027).
- [8] J. Stenger, S. Inouye, D. M. Stamper-Kurn, H.-J. Miesner, A. P. Chikkatur, and W. Ketterle. "Spin Domains in Ground-State Bose-Einstein Condensates." In: *Nature* 396.6709 (Nov. 1998), pp. 345–348. DOI: [10.1038/24567](https://doi.org/10.1038/24567).
- [9] C. C. Bradley, C. A. Sackett, J. J. Tollett, and R. G. Hulet. "Evidence of Bose-Einstein Condensation in an Atomic Gas with Attractive Interactions." In: *Phys. Rev. Lett.* 75.9 (Aug. 1995), pp. 1687–1690. DOI: [10.1103/PhysRevLett.75.1687](https://doi.org/10.1103/PhysRevLett.75.1687).
- [10] D. G. Fried, T. C. Killian, L. Willmann, D. Landhuis, S. C. Moss, D. Kleppner, and T. J. Greytak. "Bose-Einstein Condensation of Atomic Hydrogen." In: *Phys. Rev. Lett.* 81.18 (Nov. 1998), pp. 3811–3814. DOI: [10.1103/PhysRevLett.81.3811](https://doi.org/10.1103/PhysRevLett.81.3811).
- [11] S. L. Cornish, N. R. Claussen, J. L. Roberts, E. A. Cornell, and C. E. Wieman. "Stable Rb-85 Bose-Einstein Condensates with Widely Tunable Interactions." In: *Phys. Rev. Lett.* 85.9 (Aug. 2000), pp. 1795–1798. DOI: [10.1103/PhysRevLett.85.1795](https://doi.org/10.1103/PhysRevLett.85.1795).

- [12] F. Pereira Dos Santos, J. Léonard, J. Wang, C. J. Barrelet, F. Perales, E. Rasel, C. S. Unnikrishnan, M. Leduc, and C. Cohen-Tannoudji. "Bose-Einstein Condensation of Metastable Helium." In: *Phys. Rev. Lett.* 86.16 (Apr. 2001), pp. 3459–3462. DOI: [10.1103/PhysRevLett.86.3459](https://doi.org/10.1103/PhysRevLett.86.3459).
- [13] A. Robert, O. Sirjean, A. Browaeys, J. Poupard, S. Nowak, D. Boiron, C. I. Westbrook, and A. Aspect. "A Bose-Einstein Condensate of Metastable Atoms." In: *Science* 292.5516 (Apr. 2001), pp. 461–464. DOI: [10.1126/science.1060622](https://doi.org/10.1126/science.1060622).
- [14] G. Modugno, G. Ferrari, G. Roati, R. J. Brecha, A. Simoni, and M. Inguscio. "Bose-Einstein Condensation of Potassium Atoms by Sympathetic Cooling." In: *Science* 294.5545 (Nov. 2001), pp. 1320–1322. DOI: [10.1126/science.1066687](https://doi.org/10.1126/science.1066687).
- [15] T. Weber, J. Herbig, M. Mark, H.-C. Nägerl, and R. Grimm. "Bose-Einstein Condensation of Cesium." In: *Science* 299.5604 (Jan. 2003), pp. 232–235. DOI: [10.1126/science.1079699](https://doi.org/10.1126/science.1079699).
- [16] Y. Takasu, K. Maki, K. Komori, T. Takano, K. Honda, M. Kumakura, T. Yabuzaki, and Y. Takahashi. "Spin-Singlet Bose-Einstein Condensation of Two-Electron Atoms." In: *Phys. Rev. Lett.* 91.4 (July 2003), p. 040404. DOI: [10.1103/PhysRevLett.91.040404](https://doi.org/10.1103/PhysRevLett.91.040404).
- [17] A. Griesmaier, J. Werner, S. Hensler, J. Stuhler, and T. Pfau. "Bose-Einstein Condensation of Chromium." In: *Phys. Rev. Lett.* 94.16 (Apr. 2005), p. 160401. DOI: [10.1103/PhysRevLett.94.160401](https://doi.org/10.1103/PhysRevLett.94.160401).
- [18] T. Fukuhara, S. Sugawa, and Y. Takahashi. "Bose-Einstein Condensation of an Ytterbium Isotope." In: *Phys. Rev. A* 76.5 (Nov. 2007), p. 051604. DOI: [10.1103/PhysRevA.76.051604](https://doi.org/10.1103/PhysRevA.76.051604).
- [19] S. Stellmer, M. K. Tey, B. Huang, R. Grimm, and F. Schreck. "Bose-Einstein Condensation of Strontium." In: *Phys. Rev. Lett.* 103.20 (Nov. 2009), p. 200401. DOI: [10.1103/PhysRevLett.103.200401](https://doi.org/10.1103/PhysRevLett.103.200401).
- [20] S. Kraft, F. Vogt, O. Appel, F. Riehle, and U. Sterr. "Bose-Einstein Condensation of Alkaline Earth Atoms: Ca-40." In: *Phys. Rev. Lett.* 103.13 (Sept. 2009), p. 130401. DOI: [10.1103/PhysRevLett.103.130401](https://doi.org/10.1103/PhysRevLett.103.130401).
- [21] M. Lu, N. Q. Burdick, S. H. Youn, and B. L. Lev. "Strongly Dipolar Bose-Einstein Condensate of Dysprosium." In: *Phys. Rev. Lett.* 107.19 (Oct. 2011), p. 190401. DOI: [10.1103/PhysRevLett.107.190401](https://doi.org/10.1103/PhysRevLett.107.190401).
- [22] K. Aikawa, A. Frisch, M. Mark, S. Baier, A. Rietzler, R. Grimm, and F. Ferlaino. "Bose-Einstein Condensation of Erbium." In: *Phys. Rev. Lett.* 108.21 (May 2012), p. 210401. DOI: [10.1103/PhysRevLett.108.210401](https://doi.org/10.1103/PhysRevLett.108.210401).
- [23] S. Jochim, M. Bartenstein, A. Altmeyer, G. Hendl, S. Riedl, C. Chin, J. Hecker Denschlag, and R. Grimm. "Bose-Einstein Condensation of Molecules." In: *Science* 302.5653 (Dec. 2003), pp. 2101–2103. DOI: [10.1126/science.1093280](https://doi.org/10.1126/science.1093280).
- [24] M. Greiner, C. A. Regal, and D. S. Jin. "Emergence of a Molecular Bose-Einstein Condensate from a Fermi Gas." In: *Nature* 426.6966 (Dec. 2003), pp. 537–540. DOI: [10.1038/nature02199](https://doi.org/10.1038/nature02199).

- [25] M. W. Zwierlein, C. A. Stan, C. H. Schunck, S. M. F. Raupach, S. Gupta, Z. Hadzibabic, and W. Ketterle. "Observation of Bose-Einstein Condensation of Molecules." In: *Phys. Rev. Lett.* 91.25 (Dec. 2003), p. 250401. DOI: [10.1103/PhysRevLett.91.250401](https://doi.org/10.1103/PhysRevLett.91.250401).
- [26] M. R. Andrews, C. G. Townsend, H.-J. Miesner, D. S. Durfee, D. M. Kurn, and W. Ketterle. "Observation of Interference Between Two Bose Condensates." In: *Science* 275.5300 (Jan. 1997), pp. 637–641. DOI: [10.1126/science.275.5300.637](https://doi.org/10.1126/science.275.5300.637).
- [27] M.-O. Mewes, M. R. Andrews, D. M. Kurn, D. S. Durfee, C. G. Townsend, and W. Ketterle. "Output Coupler for Bose-Einstein Condensed Atoms." In: *Phys. Rev. Lett.* 78.4 (Jan. 1997), pp. 582–585. DOI: [10.1103/PhysRevLett.78.582](https://doi.org/10.1103/PhysRevLett.78.582).
- [28] M. Greiner, O. Mandel, T. Esslinger, T. W. Hänsch, and I. Bloch. "Quantum Phase Transition from a Superfluid to a Mott Insulator in a Gas of Ultracold Atoms." In: *Nature* 415.6867 (Jan. 2002), pp. 39–44. DOI: [10.1038/415039a](https://doi.org/10.1038/415039a).
- [29] S. Smale, P. He, B. A. Olsen, K. G. Jackson, H. Sharum, S. Trotzky, J. Marino, A. M. Rey, and J. H. Thywissen. "Observation of a Transition between Dynamical Phases in a Quantum Degenerate Fermi Gas." In: *Science Advances* 5.8 (Aug. 2019), eaax1568. DOI: [10.1126/sciadv.aax1568](https://doi.org/10.1126/sciadv.aax1568).
- [30] A. Chu, J. Will, J. Arlt, C. Klempt, and A. M. Rey. "Simulation of XXZ Spin Models Using Sideband Transitions in Trapped Bosonic Gases." In: *Phys. Rev. Lett.* 125.24 (Dec. 2020), p. 240504. DOI: [10.1103/PhysRevLett.125.240504](https://doi.org/10.1103/PhysRevLett.125.240504).
- [31] J. A. Muniz, D. Barberena, R. J. Lewis-Swan, D. J. Young, J. R. K. Cline, A. M. Rey, and J. K. Thompson. "Exploring Dynamical Phase Transitions with Cold Atoms in an Optical Cavity." In: *Nature* 580.7805 (Apr. 2020), pp. 602–607. DOI: [10.1038/s41586-020-2224-x](https://doi.org/10.1038/s41586-020-2224-x).
- [32] P. Jurcevic, H. Shen, P. Hauke, C. Maier, T. Brydges, C. Hempel, B. P. Lanyon, M. Heyl, R. Blatt, and C. F. Roos. "Direct Observation of Dynamical Quantum Phase Transitions in an Interacting Many-Body System." In: *Phys. Rev. Lett.* 119.8 (Aug. 2017), p. 080501. DOI: [10.1103/PhysRevLett.119.080501](https://doi.org/10.1103/PhysRevLett.119.080501).
- [33] N. Fläschner, D. Vogel, M. Tarnowski, B. S. Rem, D.-S. Lühmann, M. Heyl, J. C. Budich, L. Mathey, K. Sengstock, and C. Weitenberg. "Observation of Dynamical Vortices after Quenches in a System with Topology." In: *Nature Phys* 14.3 (Mar. 2018), pp. 265–268. DOI: [10.1038/s41567-017-0013-8](https://doi.org/10.1038/s41567-017-0013-8).
- [34] J. Zhang, P. W. Hess, A. Kyprianidis, P. Becker, A. Lee, J. Smith, G. Pagano, I.-D. Potirniche, A. C. Potter, A. Vishwanath, N. Y. Yao, and C. Monroe. "Observation of a Discrete Time Crystal." In: *Nature* 543.7644 (Mar. 2017), pp. 217–220. DOI: [10.1038/nature21413](https://doi.org/10.1038/nature21413).

- [35] S. Choi, J. Choi, R. Landig, G. Kucsko, H. Zhou, J. Isoya, F. Jelezko, S. Onoda, H. Sumiya, V. Khemani, C. von Keyserlingk, N. Y. Yao, E. Demler, and M. D. Lukin. "Observation of Discrete Time-Crystalline Order in a Disordered Dipolar Many-Body System." In: *Nature* 543.7644 (Mar. 2017), pp. 221–225. DOI: [10.1038/nature21426](https://doi.org/10.1038/nature21426).
- [36] P. Cejnar, P. Stránský, M. Macek, and M. Kloc. "Excited-State Quantum Phase Transitions." In: *J. Phys. A: Math. Theor.* 54.13 (Mar. 2021), p. 133001. DOI: [10.1088/1751-8121/abdf8](https://doi.org/10.1088/1751-8121/abdf8).
- [37] M. Child, T. Weston, and J. Tennyson. "Quantum Monodromy in the Spectrum of H₂O and Other Systems: New Insight into the Level Structure of Quasi-Linear Molecules." In: *Molecular Physics* 96.3 (1999), pp. 371–379. DOI: [10.1080/00268979909482971](https://doi.org/10.1080/00268979909482971).
- [38] B. P. Winnewisser, M. Winnewisser, I. R. Medvedev, M. Behnke, F. C. De Lucia, S. C. Ross, and J. Koput. "Experimental Confirmation of Quantum Monodromy: The Millimeter Wave Spectrum of Cyanogen Isothiocyanate NCNCS." In: *Phys. Rev. Lett.* 95.24 (Dec. 2005), p. 243002. DOI: [10.1103/PhysRevLett.95.243002](https://doi.org/10.1103/PhysRevLett.95.243002).
- [39] N. F. Zobov, S. V. Shirin, O. L. Polyansky, J. Tennyson, P.-F. Coheur, P. F. Bernath, M. Carleer, and R. Colin. "Monodromy in the Water Molecule." In: *Chemical Physics Letters* 414.1 (Oct. 2005), pp. 193–197. DOI: [10.1016/j.cplett.2005.08.028](https://doi.org/10.1016/j.cplett.2005.08.028).
- [40] D. Larese, F. Pérez-Bernal, and F. Iachello. "Signatures of Quantum Phase Transitions and Excited State Quantum Phase Transitions in the Vibrational Bending Dynamics of Triatomic Molecules." In: *Journal of Molecular Structure* 1051 (Nov. 2013), pp. 310–327. DOI: [10.1016/j.molstruc.2013.08.020](https://doi.org/10.1016/j.molstruc.2013.08.020).
- [41] J. Khalouf-Rivera, F. Pérez-Bernal, and M. Carvajal. "Excited State Quantum Phase Transitions in the Bending Spectra of Molecules." In: *Journal of Quantitative Spectroscopy and Radiative Transfer* 261 (Mar. 2021), p. 107436. DOI: [10.1016/j.jqsrt.2020.107436](https://doi.org/10.1016/j.jqsrt.2020.107436).
- [42] M. Albiez, R. Gati, J. Fölling, S. Hunsmann, M. Cristiani, and M. K. Oberthaler. "Direct Observation of Tunneling and Nonlinear Self-Trapping in a Single Bosonic Josephson Junction." In: *Phys. Rev. Lett.* 95.1 (June 2005), p. 010402. DOI: [10.1103/PhysRevLett.95.010402](https://doi.org/10.1103/PhysRevLett.95.010402).
- [43] T. Zibold, E. Nicklas, C. Gross, and M. K. Oberthaler. "Classical Bifurcation at the Transition from Rabi to Josephson Dynamics." In: *Phys. Rev. Lett.* 105.20 (Nov. 2010), p. 204101. DOI: [10.1103/PhysRevLett.105.204101](https://doi.org/10.1103/PhysRevLett.105.204101).
- [44] M.-S. Chang, Q. Qin, W. Zhang, L. You, and M. S. Chapman. "Coherent Spinor Dynamics in a Spin-1 Bose Condensate." In: *Nature Phys* 1.2 (Nov. 2005), pp. 111–116. DOI: [10.1038/nphys153](https://doi.org/10.1038/nphys153).
- [45] W. Zhang, D. L. Zhou, M.-S. Chang, M. S. Chapman, and L. You. "Coherent Spin Mixing Dynamics in a Spin-1 Atomic Condensate." In: *Phys. Rev. A* 72.1 (July 2005), p. 013602. DOI: [10.1103/PhysRevA.72.013602](https://doi.org/10.1103/PhysRevA.72.013602).

- [46] Y. Kawaguchi and M. Ueda. “Spinor Bose–Einstein Condensates.” In: *Physics Reports*. Spinor Bose–Einstein Condensates 520.5 (Nov. 2012), pp. 253–381. DOI: [10.1016/j.physrep.2012.07.005](https://doi.org/10.1016/j.physrep.2012.07.005).
- [47] P. Feldmann, C. Klempt, A. Smerzi, L. Santos, and M. Gessner. “Interferometric Order Parameter for Excited-State Quantum Phase Transitions in Bose-Einstein Condensates.” In: *Phys. Rev. Lett.* 126.23 (June 2021), p. 230602. DOI: [10.1103/PhysRevLett.126.230602](https://doi.org/10.1103/PhysRevLett.126.230602).
- [48] T. Brandes. “Excited-State Quantum Phase Transitions in Dicke Superradiance Models.” In: *Phys. Rev. E* 88.3 (Sept. 2013), p. 032133. DOI: [10.1103/PhysRevE.88.032133](https://doi.org/10.1103/PhysRevE.88.032133).
- [49] R. Puebla, A. Relaño, and J. Retamosa. “Excited-State Phase Transition Leading to Symmetry-Breaking Steady States in the Dicke Model.” In: *Phys. Rev. A* 87.2 (Feb. 2013), p. 023819. DOI: [10.1103/PhysRevA.87.023819](https://doi.org/10.1103/PhysRevA.87.023819).
- [50] R. Puebla and A. Relaño. “Non-Thermal Excited-State Quantum Phase Transitions.” In: *EPL* 104.5 (Jan. 2014), p. 50007. DOI: [10.1209/0295-5075/104/50007](https://doi.org/10.1209/0295-5075/104/50007).
- [51] J. Cabedo and A. Celi. “Excited-State Quantum Phase Transitions in Spin-Orbit-Coupled Bose Gases.” In: *Phys. Rev. Res.* 3.4 (Dec. 2021), p. 043215. DOI: [10.1103/PhysRevResearch.3.043215](https://doi.org/10.1103/PhysRevResearch.3.043215).
- [52] C. K. Law, H. Pu, and N. P. Bigelow. “Quantum Spins Mixing in Spinor Bose-Einstein Condensates.” In: *Phys. Rev. Lett.* 81.24 (Dec. 1998), pp. 5257–5261. DOI: [10.1103/PhysRevLett.81.5257](https://doi.org/10.1103/PhysRevLett.81.5257).
- [53] H. Pu, C. K. Law, S. Raghavan, J. H. Eberly, and N. P. Bigelow. “Spin-Mixing Dynamics of a Spinor Bose-Einstein Condensate.” In: *Phys. Rev. A* 60.2 (Aug. 1999), pp. 1463–1470. DOI: [10.1103/PhysRevA.60.1463](https://doi.org/10.1103/PhysRevA.60.1463).
- [54] J. Dalibard. “Collisional Dynamics of Ultra-Cold Atomic Gases.” In: *Proceedings of the International School of Physics - Enrico Fermi*. Ed. by M. Inguscio, S. Stringari, and C. E. Wieman. Vol. 140. 1999. ISBN: 978-1-61499-225-7.
- [55] T.-L. Ho. “Spinor Bose Condensates in Optical Traps.” In: *Phys. Rev. Lett.* 81.4 (July 1998), pp. 742–745. DOI: [10.1103/PhysRevLett.81.742](https://doi.org/10.1103/PhysRevLett.81.742).
- [56] T. Ohmi and K. Machida. “Bose-Einstein Condensation with Internal Degrees of Freedom in Alkali Atom Gases.” In: *J. Phys. Soc. Jpn.* 67.6 (June 1998), pp. 1822–1825. DOI: [10.1143/JPSJ.67.1822](https://doi.org/10.1143/JPSJ.67.1822).
- [57] E. G. M. van Kempen, S. J. J. M. F. Kokkelmans, D. J. Heinzen, and B. J. Verhaar. “Interisotope Determination of Ultracold Rubidium Interactions from Three High-Precision Experiments.” In: *Phys. Rev. Lett.* 88.9 (Feb. 2002), p. 093201. DOI: [10.1103/PhysRevLett.88.093201](https://doi.org/10.1103/PhysRevLett.88.093201).

- [58] K. Lange, J. Peise, B. Lücke, I. Kruse, G. Vitagliano, I. Apellaniz, M. Kleinmann, G. Tóth, and C. Klempt. “Entanglement between Two Spatially Separated Atomic Modes.” In: *Science* 360.6387 (Apr. 2018), pp. 416–418. DOI: [10.1126/science.aao2035](https://doi.org/10.1126/science.aao2035).
- [59] S. Yi, Ö. E. Müstecaplıoğlu, C. P. Sun, and L. You. “Single-Mode Approximation in a Spinor-1 Atomic Condensate.” In: *Phys. Rev. A* 66.1 (July 2002), p. 011601. DOI: [10.1103/PhysRevA.66.011601](https://doi.org/10.1103/PhysRevA.66.011601).
- [60] *Private communication: Calculations performed by Luis Santos.*
- [61] E. P. Gross. “Structure of a Quantized Vortex in Boson Systems.” In: *Nuovo Cim* 20.3 (May 1961), pp. 454–477. DOI: [10.1007/BF02731494](https://doi.org/10.1007/BF02731494).
- [62] L. P. Pitaevskii. “Vortex Lines in an Imperfect Bose Gas.” In: *J. Exptl. Theoret. Phys. (U.S.S.R.)* 13.2 (Aug. 1961), p. 451.
- [63] L. P. Pitaevskii and S. Stringari. *Bose-Einstein Condensation*. International Series of Monographs on Physics. Oxford, New York, Apr. 2003. ISBN: 978-0-19-850719-2.
- [64] L. Pezzè, A. Smerzi, M. K. Oberthaler, R. Schmied, and P. Treutlein. “Quantum Metrology with Nonclassical States of Atomic Ensembles.” In: *Rev. Mod. Phys.* 90.3 (Sept. 2018), p. 035005. DOI: [10.1103/RevModPhys.90.035005](https://doi.org/10.1103/RevModPhys.90.035005).
- [65] B. Lücke, M. Scherer, J. Kruse, L. Pezzè, F. Deuretzbacher, P. Hyllus, O. Topic, J. Peise, W. Ertmer, J. Arlt, L. Santos, A. Smerzi, and C. Klempt. “Twin Matter Waves for Interferometry Beyond the Classical Limit.” In: *Science* 334.6057 (Nov. 2011), pp. 773–776. DOI: [10.1126/science.1208798](https://doi.org/10.1126/science.1208798).
- [66] C. Klempt, O. Topic, G. Gebreyesus, M. Scherer, T. Henninger, P. Hyllus, W. Ertmer, L. Santos, and J. J. Arlt. “Parametric Amplification of Vacuum Fluctuations in a Spinor Condensate.” In: *Phys. Rev. Lett.* 104.19 (May 2010), p. 195303. DOI: [10.1103/PhysRevLett.104.195303](https://doi.org/10.1103/PhysRevLett.104.195303).
- [67] D. M. Stamper-Kurn and M. Ueda. “Spinor Bose Gases: Symmetries, Magnetism, and Quantum Dynamics.” In: *Rev. Mod. Phys.* 85.3 (July 2013), pp. 1191–1244. DOI: [10.1103/RevModPhys.85.1191](https://doi.org/10.1103/RevModPhys.85.1191).
- [68] M.-S. Chang, C. D. Hamley, M. D. Barrett, J. A. Sauer, K. M. Fortier, W. Zhang, L. You, and M. S. Chapman. “Observation of Spinor Dynamics in Optically Trapped Rb-87 Bose-Einstein Condensates.” In: *Phys. Rev. Lett.* 92.14 (Apr. 2004), p. 140403. DOI: [10.1103/PhysRevLett.92.140403](https://doi.org/10.1103/PhysRevLett.92.140403).
- [69] T. M. Hoang, H. M. Bharath, M. J. Boguslawski, M. Anquez, B. A. Robbins, and M. S. Chapman. “Adiabatic Quenches and Characterization of Amplitude Excitations in a Continuous Quantum Phase Transition.” In: *Proceedings of the National Academy of Sciences* 113.34 (Aug. 2016), pp. 9475–9479. DOI: [10.1073/pnas.1600267113](https://doi.org/10.1073/pnas.1600267113).
- [70] C. Gerry and P. Knight. *Introductory Quantum Optics*. Cambridge, 2004. ISBN: 978-0-521-52735-4. DOI: [10.1017/CB09780511791239](https://doi.org/10.1017/CB09780511791239).

- [71] J. S. Schwinger. *On Angular Momentum*. Jan. 1952.
- [72] R. H. Dicke. “Coherence in Spontaneous Radiation Processes.” In: *Phys. Rev.* 93.1 (Jan. 1954), pp. 99–110. DOI: [10.1103/PhysRev.93.99](https://doi.org/10.1103/PhysRev.93.99).
- [73] F. T. Arecchi, E. Courtens, R. Gilmore, and H. Thomas. “Atomic Coherent States in Quantum Optics.” In: *Phys. Rev. A* 6.6 (Dec. 1972), pp. 2211–2237. DOI: [10.1103/PhysRevA.6.2211](https://doi.org/10.1103/PhysRevA.6.2211).
- [74] J. M. Radcliffe. “Some Properties of Coherent Spin States.” In: *J. Phys. A: Gen. Phys.* 4.3 (May 1971), p. 313. DOI: [10.1088/0305-4470/4/3/009](https://doi.org/10.1088/0305-4470/4/3/009).
- [75] H. Strobel. “Fisher Information and Entanglement of Non-Gaussian Spin States.” PhD Thesis. Universität Heidelberg, 2016. DOI: [10.11588/heidok.00020251](https://doi.org/10.11588/heidok.00020251).
- [76] P. Feldmann. “Generalized Quantum Phase Transitions for Quantum-State Engineering in Spinor Bose-Einstein Condensates.” PhD Thesis. Leibniz Universität Hannover, 2021. DOI: [10.15488/10772](https://doi.org/10.15488/10772).
- [77] P. Kunkel. “Splitting a Bose-Einstein Condensate Enables EPR Steering and Simultaneous Readout of Noncommuting Observables.” PhD Thesis. Universität Heidelberg, 2019. DOI: [10.11588/heidok.00027462](https://doi.org/10.11588/heidok.00027462).
- [78] D. A. Steck. *Rubidium 87 D Line Data*. July 2021. URL: <https://steck.us/alkalidata/>.
- [79] Y. B. Ovchinnikov, K. Szymaniec, and S. Edris. “Measurement of Rubidium Ground-State Hyperfine Transition Frequency Using Atomic Fountains.” In: *Metrologia* 52.4 (Aug. 2015), p. 595. DOI: [10.1088/0026-1394/52/4/595](https://doi.org/10.1088/0026-1394/52/4/595).
- [80] G. Breit and I. I. Rabi. “Measurement of Nuclear Spin.” In: *Phys. Rev.* 38.11 (Dec. 1931), pp. 2082–2083. DOI: [10.1103/PhysRev.38.2082.2](https://doi.org/10.1103/PhysRev.38.2082.2).
- [81] E. Arimondo, M. Inguscio, and P. Violino. “Experimental Determinations of the Hyperfine Structure in the Alkali Atoms.” In: *Rev. Mod. Phys.* 49.1 (Jan. 1977), pp. 31–75. DOI: [10.1103/RevModPhys.49.31](https://doi.org/10.1103/RevModPhys.49.31).
- [82] J. Stark. “Beobachtungen über den Effekt des elektrischen Feldes auf Spektrallinien. I. Quereffekt.” In: *Annalen der Physik* 348.7 (1914), pp. 965–982. DOI: [10.1002/andp.19143480702](https://doi.org/10.1002/andp.19143480702).
- [83] P. Zeeman. “The Effect of Magnetisation on the Nature of Light Emitted by a Substance.” In: *Nature* 55.1424 (Feb. 1897), pp. 347–347. DOI: [10.1038/055347a0](https://doi.org/10.1038/055347a0).
- [84] E. Tiesinga, P. J. Mohr, D. B. Newell, and B. N. Taylor. “CODATA Recommended Values of the Fundamental Physical Constants: 2018.” In: *Rev. Mod. Phys.* 93.2 (June 2021), p. 025010. DOI: [10.1103/RevModPhys.93.025010](https://doi.org/10.1103/RevModPhys.93.025010).
- [85] T. Mayer-Kuckuk. *Atomphysik*. Wiesbaden, 1994. ISBN: 978-3-519-33042-4 978-3-322-91793-5. DOI: [10.1007/978-3-322-91793-5](https://doi.org/10.1007/978-3-322-91793-5).

BIBLIOGRAPHY

- [86] I. I. Rabi, S. Millman, P. Kusch, and J. R. Zacharias. “The Molecular Beam Resonance Method for Measuring Nuclear Magnetic Moments. The Magnetic Moments of ${}^3\text{Li}$, ${}^7\text{Li}$ and ${}^{19}\text{F}$.” In: *Phys. Rev.* 55.6 (Mar. 1939), pp. 526–535. DOI: [10.1103/PhysRev.55.526](https://doi.org/10.1103/PhysRev.55.526).
- [87] M. Boguslawski. “All-Microwave Control of Hyperfine States in Ultracold Spin-1 Rubidium.” PhD Thesis. Georgia Institute of Technology, Oct. 2019. URL: <http://hdl.handle.net/1853/62298>.
- [88] B. Meyer. “Versatile, Low-Phase-Noise Microwave Source for Cold ${}^{87}\text{Rb}$ Experiments.” Master’s Thesis. Leibniz Universität Hannover, 2020.
- [89] I. Kruse, K. Lange, J. Peise, B. Lücke, L. Pezzè, J. Arlt, W. Ertmer, C. Lisdat, L. Santos, A. Smerzi, and C. Klempt. “Improvement of an Atomic Clock Using Squeezed Vacuum.” In: *Phys. Rev. Lett.* 117.14 (Sept. 2016), p. 143004. DOI: [10.1103/PhysRevLett.117.143004](https://doi.org/10.1103/PhysRevLett.117.143004).
- [90] R. J. Glauber. “Coherent and Incoherent States of the Radiation Field.” In: *Phys. Rev.* 131.6 (Sept. 1963), pp. 2766–2788. DOI: [10.1103/PhysRev.131.2766](https://doi.org/10.1103/PhysRev.131.2766).
- [91] P. Ehrenfest. “Phasenumwandlungen im üblichen und erweiterten Sinn, classifiziert nach den entsprechenden Singularitäten des thermodynamischen Potentials.” In: *Proceedings Koninklijke Akademie van Wetenschappen* 36 (1933), pp. 153–157.
- [92] Z. Zhang and L.-M. Duan. “Generation of Massive Entanglement through an Adiabatic Quantum Phase Transition in a Spinor Condensate.” In: *Phys. Rev. Lett.* 111.18 (Oct. 2013), p. 180401. DOI: [10.1103/PhysRevLett.111.180401](https://doi.org/10.1103/PhysRevLett.111.180401).
- [93] S. Sachdev. *Quantum Phase Transitions*. 2nd ed. Cambridge, 2011. ISBN: 978-0-521-51468-2. DOI: [10.1017/CB09780511973765](https://doi.org/10.1017/CB09780511973765).
- [94] K. Murata, H. Saito, and M. Ueda. “Broken-Axisymmetry Phase of a Spin-1 Ferromagnetic Bose-Einstein Condensate.” In: *Phys. Rev. A* 75.1 (Jan. 2007), p. 013607. DOI: [10.1103/PhysRevA.75.013607](https://doi.org/10.1103/PhysRevA.75.013607).
- [95] P. Feldmann, M. Gessner, M. Gabbrielli, C. Klempt, L. Santos, L. Pezzè, and A. Smerzi. “Interferometric Sensitivity and Entanglement by Scanning through Quantum Phase Transitions in Spinor Bose-Einstein Condensates.” In: *Phys. Rev. A* 97.3 (Mar. 2018), p. 032339. DOI: [10.1103/PhysRevA.97.032339](https://doi.org/10.1103/PhysRevA.97.032339).
- [96] L. Pezzè, M. Gessner, P. Feldmann, C. Klempt, L. Santos, and A. Smerzi. “Heralded Generation of Macroscopic Superposition States in a Spinor Bose-Einstein Condensate.” In: *Phys. Rev. Lett.* 123.26 (Dec. 2019), p. 260403. DOI: [10.1103/PhysRevLett.123.260403](https://doi.org/10.1103/PhysRevLett.123.260403).
- [97] M. Born and V. Fock. “Beweis des Adiabatsatzes.” In: *Z. Physik* 51.3 (Mar. 1928), pp. 165–180. DOI: [10.1007/BF01343193](https://doi.org/10.1007/BF01343193).
- [98] D. J. Griffiths and D. F. Schroeter. *Introduction to Quantum Mechanics*. Third edition. Cambridge ; New York, NY, 2018. ISBN: 978-1-107-18963-8.

- [99] X.-Y. Luo, Y.-Q. Zou, L.-N. Wu, Q. Liu, M.-F. Han, M. K. Tey, and L. You. “Deterministic Entanglement Generation from Driving through Quantum Phase Transitions.” In: *Science* 355.6325 (Feb. 2017), pp. 620–623. DOI: [10.1126/science.aag1106](https://doi.org/10.1126/science.aag1106).
- [100] F. Anders et al. “Momentum Entanglement for Atom Interferometry.” In: *Phys. Rev. Lett.* 127.14 (Sept. 2021), p. 140402. DOI: [10.1103/PhysRevLett.127.140402](https://doi.org/10.1103/PhysRevLett.127.140402).
- [101] L.-N. Wu and L. You. “Using the Ground State of an Antiferromagnetic Spin-1 Atomic Condensate for Heisenberg-limited Metrology.” In: *Phys. Rev. A* 93.3 (Mar. 2016), p. 033608. DOI: [10.1103/PhysRevA.93.033608](https://doi.org/10.1103/PhysRevA.93.033608).
- [102] D. Kajtoch, K. Pawłowski, and E. Witkowska. “Metrologically Useful States of Spin-1 Bose Condensates with Macroscopic Magnetization.” In: *Phys. Rev. A* 97.2 (Feb. 2018), p. 023616. DOI: [10.1103/PhysRevA.97.023616](https://doi.org/10.1103/PhysRevA.97.023616).
- [103] M. A. Caprio, P. Cejnar, and F. Iachello. “Excited State Quantum Phase Transitions in Many-Body Systems.” In: *Annals of Physics* 323.5 (May 2008), pp. 1106–1135. DOI: [10.1016/j.aop.2007.06.011](https://doi.org/10.1016/j.aop.2007.06.011).
- [104] C. B. Dağ, S.-T. Wang, and L.-M. Duan. “Classification of Quench-Dynamical Behaviors in Spinor Condensates.” In: *Phys. Rev. A* 97.2 (Feb. 2018), p. 023603. DOI: [10.1103/PhysRevA.97.023603](https://doi.org/10.1103/PhysRevA.97.023603).
- [105] B. Dietz, F. Iachello, M. Miski-Oglu, N. Pietralla, A. Richter, L. von Smekal, and J. Wambach. “Lifshitz and Excited-State Quantum Phase Transitions in Microwave Dirac Billiards.” In: *Phys. Rev. B* 88.10 (Sept. 2013), p. 104101. DOI: [10.1103/PhysRevB.88.104101](https://doi.org/10.1103/PhysRevB.88.104101).
- [106] L. Zhao, J. Jiang, T. Tang, M. Webb, and Y. Liu. “Dynamics in Spinor Condensates Tuned by a Microwave Dressing Field.” In: *Phys. Rev. A* 89.2 (Feb. 2014), p. 023608. DOI: [10.1103/PhysRevA.89.023608](https://doi.org/10.1103/PhysRevA.89.023608).
- [107] A. Smerzi, S. Fantoni, S. Giovanazzi, and S. R. Shenoy. “Quantum Coherent Atomic Tunneling between Two Trapped Bose-Einstein Condensates.” In: *Phys. Rev. Lett.* 79.25 (Dec. 1997), pp. 4950–4953. DOI: [10.1103/PhysRevLett.79.4950](https://doi.org/10.1103/PhysRevLett.79.4950).
- [108] G. J. Milburn, J. Corney, E. M. Wright, and D. F. Walls. “Quantum Dynamics of an Atomic Bose-Einstein Condensate in a Double-Well Potential.” In: *Phys. Rev. A* 55.6 (June 1997), pp. 4318–4324. DOI: [10.1103/PhysRevA.55.4318](https://doi.org/10.1103/PhysRevA.55.4318).
- [109] C. S. Gerving, T. M. Hoang, B. J. Land, M. Anquez, C. D. Hamley, and M. S. Chapman. “Non-Equilibrium Dynamics of an Unstable Quantum Pendulum Explored in a Spin-1 Bose-Einstein Condensate.” In: *Nat Commun* 3.1 (Nov. 2012), p. 1169. DOI: [10.1038/ncomms2179](https://doi.org/10.1038/ncomms2179).

BIBLIOGRAPHY

- [110] T. Tian, H.-X. Yang, L.-Y. Qiu, H.-Y. Liang, Y.-B. Yang, Y. Xu, and L.-M. Duan. "Observation of Dynamical Quantum Phase Transitions with Correspondence in an Excited State Phase Diagram." In: *Phys. Rev. Lett.* 124.4 (Jan. 2020), p. 043001. DOI: [10.1103/PhysRevLett.124.043001](https://doi.org/10.1103/PhysRevLett.124.043001).
- [111] C. Klempt. "Wechselwirkung in Bose-Fermi-Quantengasen." PhD Thesis. Leibniz Universität Hannover, 2007. DOI: [10.15488/6906](https://doi.org/10.15488/6906).
- [112] C. Klempt, T. van Zoest, T. Henninger, O. Topic, E. Rasel, W. Ertmer, and J. Arlt. "Ultraviolet Light-Induced Atom Desorption for Large Rubidium and Potassium Magneto-Optical Traps." In: *Phys. Rev. A* 73.1 (Jan. 2006), p. 013410. DOI: [10.1103/PhysRevA.73.013410](https://doi.org/10.1103/PhysRevA.73.013410).
- [113] E. L. Raab, M. Prentiss, A. Cable, S. Chu, and D. E. Pritchard. "Trapping of Neutral Sodium Atoms with Radiation Pressure." In: *Phys. Rev. Lett.* 59.23 (Dec. 1987), pp. 2631–2634. DOI: [10.1103/PhysRevLett.59.2631](https://doi.org/10.1103/PhysRevLett.59.2631).
- [114] W. D. Phillips. "Nobel Lecture: Laser Cooling and Trapping of Neutral Atoms." In: *Rev. Mod. Phys.* 70.3 (July 1998), pp. 721–741. DOI: [10.1103/RevModPhys.70.721](https://doi.org/10.1103/RevModPhys.70.721).
- [115] J. Dalibard and C. Cohen-Tannoudji. "Laser Cooling below the Doppler Limit by Polarization Gradients: Simple Theoretical Models." In: *J. Opt. Soc. Am. B, JOSAB* 6.11 (Nov. 1989), pp. 2023–2045. DOI: [10.1364/JOSAB.6.002023](https://doi.org/10.1364/JOSAB.6.002023).
- [116] H. J. Lewandowski, D. M. Harber, D. L. Whitaker, and E. A. Cornell. "Simplified System for Creating a Bose-Einstein Condensate." In: *Journal of Low Temperature Physics* 132.5 (Sept. 2003), pp. 309–367. DOI: [10.1023/A:1024800600621](https://doi.org/10.1023/A:1024800600621).
- [117] W. Ketterle and N. J. V. Druten. "Evaporative Cooling of Trapped Atoms." In: *Advances In Atomic, Molecular, and Optical Physics*. Ed. by B. Bederson and H. Walther. Vol. 37. Jan. 1996, pp. 181–236. DOI: [10.1016/S1049-250X\(08\)60101-9](https://doi.org/10.1016/S1049-250X(08)60101-9).
- [118] C. S. Adams, H. J. Lee, N. Davidson, M. Kasevich, and S. Chu. "Evaporative Cooling in a Crossed Dipole Trap." In: *Phys. Rev. Lett.* 74.18 (May 1995), pp. 3577–3580. DOI: [10.1103/PhysRevLett.74.3577](https://doi.org/10.1103/PhysRevLett.74.3577).
- [119] M. Scherer. "Nichtklassische Zustände in Spinor-Bose-Einstein-Kondensaten." PhD Thesis. Leibniz Universität Hannover, 2011. DOI: [10.15488/7959](https://doi.org/10.15488/7959).
- [120] W. Gerlach and O. Stern. "Der experimentelle Nachweis der Richtungsquantelung im Magnetfeld." In: *Z. Physik* 9.1 (Dec. 1922), pp. 349–352. DOI: [10.1007/BF01326983](https://doi.org/10.1007/BF01326983).
- [121] B. Lücke. "Multi-Particle Entanglement in a Spinor Bose-Einstein Condensate for Quantum-Enhanced Interferometry." PhD Thesis. Leibniz Universität Hannover, 2014. DOI: [10.15488/8318](https://doi.org/10.15488/8318).

- [122] M. Quensen. “Fast Magnetic Field Stabilization Using the Anisotropic Magnetoresistive Effect.” Master’s Thesis. Leibniz Universität Hannover, 2020.
- [123] N. F. Ramsey. “A Molecular Beam Resonance Method with Separated Oscillating Fields.” In: *Phys. Rev.* 78.6 (June 1950), pp. 695–699. DOI: [10.1103/PhysRev.78.695](https://doi.org/10.1103/PhysRev.78.695).
- [124] F. Anders. “Entangled Momentum Modes for Atom Interferometry.” PhD Thesis. Leibniz Universität Hannover, 2022. DOI: [10.15488/12802](https://doi.org/10.15488/12802).
- [125] B. Meyer-Hoppe, M. Baron, C. Cassens, F. Anders, A. Idel, J. Peise, and C. Klempt. “Dynamical Low-Noise Microwave Source for Cold-Atom Experiments.” In: *Review of Scientific Instruments* 94.7 (July 2023), p. 074705. DOI: [10.1063/5.0160367](https://doi.org/10.1063/5.0160367).
- [126] P. Kulik, G. Kasprowicz, and M. Gaska. “Driver Module for Quantum Computer Experiments: Kasli.” In: *Photonics Applications in Astronomy, Communications, Industry, and High-Energy Physics Experiments 2018*. Vol. 10808. Oct. 2018, pp. 1255–1258. DOI: [10.1117/12.2501709](https://doi.org/10.1117/12.2501709).
- [127] S. Bourdeauducq, whitequark, R. Jördens, D. Nadlinger, Y. Sionneau, and F. Kermarrec. ARTIQ. Zenodo. Feb. 2021. DOI: [10.5281/zenodo.6619071](https://doi.org/10.5281/zenodo.6619071).
- [128] M. Baron. “Dynamic Radio-Frequency Sources for Atomic State Preparation.” Master’s Thesis. Leibniz Universität Hannover, 2022.
- [129] *GitLab: Arbitrary-Pulses-Spinor-BEC*. May 2023. URL: <https://gitlab.projekt.uni-hannover.de/iqo-artiq/artiq/public/arbitrary-pulses-spinor-bec>.
- [130] G. Kasprowicz, T. Harty, S. Bourdeauducq, R. Jördens, D. Allcock, D. Nadlinger, J. Britton, A. Sotirova, and D. Nowicka. “Urukul – Open-Source Frequency Synthesizer Module for Quantum Physics.” In: *International Journal of Electronics and Telecommunications* 68.1 (Feb. 2022), pp. 123–128. URL: <http://ijet.pl/index.php/ijet/article/view/10.24425-ijet.2022.139859>.
- [131] G. Kasprowicz et al. “ARTIQ and Sinara: Open Software and Hardware Stacks for Quantum Physics.” In: *OSA Quantum 2.0 Conference (2020), Paper QTu8B.14*. Sept. 2020, QTu8B.14. DOI: [10.1364/QUANTUM.2020.QTu8B.14](https://doi.org/10.1364/QUANTUM.2020.QTu8B.14).
- [132] *AD9910 Datasheet and Product Info | Analog Devices*. URL: <https://www.analog.com/en/products/ad9910.html#product-documentation>.
- [133] E. Rubiola. *Phase Noise and Frequency Stability in Oscillators*. The Cambridge RF and Microwave Engineering Series. Cambridge, 2008. ISBN: 978-0-521-15328-7. DOI: [10.1017/CB09780511812798](https://doi.org/10.1017/CB09780511812798).
- [134] “IEEE Standard Definitions of Physical Quantities for Fundamental Frequency and Time Metrology—Random Instabilities.” In: *IEEE Std Std 1139-2008* (Feb. 2009), pp. c1–35. DOI: [10.1109/IEEESTD.2008.4797525](https://doi.org/10.1109/IEEESTD.2008.4797525).

BIBLIOGRAPHY

- [135] R. Boudot, S. Guerandel, and E. de Clercq. "Simple-Design Low-Noise NLTL-Based Frequency Synthesizers for a CPT Cs Clock." In: *IEEE Transactions on Instrumentation and Measurement* 58.10 (Oct. 2009), pp. 3659–3665. DOI: [10.1109/TIM.2009.2019306](https://doi.org/10.1109/TIM.2009.2019306).
- [136] T. M. Fortier, C. W. Nelson, A. Hati, F. Quinlan, J. Taylor, H. Jiang, C. W. Chou, T. Rosenband, N. Lemke, A. Ludlow, D. Howe, C. W. Oates, and S. A. Diddams. "Sub-Femtosecond Absolute Timing Jitter with a 10 GHz Hybrid Photonic-Microwave Oscillator." In: *Applied Physics Letters* 100.23 (June 2012), p. 231111. DOI: [10.1063/1.4726122](https://doi.org/10.1063/1.4726122).
- [137] B. François, C. E. Calosso, M. Abdel Hafiz, S. Micalizio, and R. Boudot. "Simple-Design Ultra-Low Phase Noise Microwave Frequency Synthesizers for High-Performing Cs and Rb Vapor-Cell Atomic Clocks." In: *Review of Scientific Instruments* 86.9 (Sept. 2015), p. 094707. DOI: [10.1063/1.4929384](https://doi.org/10.1063/1.4929384).
- [138] M. Abdel Hafiz, G. Coget, P. Yun, S. Guérandel, E. de Clercq, and R. Boudot. "A High-Performance Raman-Ramsey Cs Vapor Cell Atomic Clock." In: *Journal of Applied Physics* 121.10 (Mar. 2017), p. 104903. DOI: [10.1063/1.4977955](https://doi.org/10.1063/1.4977955).
- [139] Z. Chen, J. G. Bohnet, J. M. Weiner, and J. K. Thompson. "A Low Phase Noise Microwave Source for Atomic Spin Squeezing Experiments in 87Rb ." In: *Review of Scientific Instruments* 83.4 (Apr. 2012), p. 044701. DOI: [10.1063/1.3700247](https://doi.org/10.1063/1.3700247).
- [140] I. Morgenstern, S. Zhong, Q. Zhang, L. Baker, J. Norris, B. Tran, and A. Schwettmann. "A Versatile Microwave Source for Cold Atom Experiments Controlled by a Field Programmable Gate Array." In: *Review of Scientific Instruments* 91.2 (Feb. 2020), p. 023202. DOI: [10.1063/1.5127880](https://doi.org/10.1063/1.5127880).
- [141] B. Meyer-Hoppe. *Component List for the Microwave Source Described in "Dynamical Low-Noise Microwave Source for Cold-Atom Experiments"*. Mar. 2023. DOI: [10.25835/n3198dkt](https://doi.org/10.25835/n3198dkt).
- [142] Z. Chen, J. G. Bohnet, J. M. Weiner, and J. K. Thompson. "General Formalism for Evaluating the Impact of Phase Noise on Bloch Vector Rotations." In: *Phys. Rev. A* 86.3 (Sept. 2012), p. 032313. DOI: [10.1103/PhysRevA.86.032313](https://doi.org/10.1103/PhysRevA.86.032313).
- [143] B. Barrett, P.-A. Gominet, E. Cantin, L. Antoni-Micollier, A. Bertoldi, B. Battelier, P. Bouyer, J. Lautier, and A. Landragin. "Mobile and Remote Inertial Sensing with Atom Interferometers." In: *ENFI 188. Atom Interferometry* (2014), pp. 493–555. DOI: [10.3254/978-1-61499-448-0-493](https://doi.org/10.3254/978-1-61499-448-0-493).
- [144] R. B. Blackman and J. W. Tukey. "The Measurement of Power Spectra from the Point of View of Communications Engineering — Part I." In: *The Bell System Technical Journal* 37.1 (Jan. 1958), pp. 185–282. DOI: [10.1002/j.1538-7305.1958.tb03874.x](https://doi.org/10.1002/j.1538-7305.1958.tb03874.x).

- [145] R. B. Blackman and J. W. Tukey. "The Measurement of Power Spectra from the Point of View of Communications Engineering — Part II." In: *The Bell System Technical Journal* 37.2 (Mar. 1958), pp. 485–569. DOI: [10.1002/j.1538-7305.1958.tb01530.x](https://doi.org/10.1002/j.1538-7305.1958.tb01530.x).
- [146] W. S. Warren. "Effects of Pulse Shaping in Laser Spectroscopy and Nuclear Magnetic Resonance." In: *Science* 242.4880 (Nov. 1988), pp. 878–884. DOI: [10.1126/science.3055299](https://doi.org/10.1126/science.3055299).
- [147] B. Fang, N. Mielec, D. Savoie, M. Altorio, A. Landragin, and R. Geiger. "Improving the Phase Response of an Atom Interferometer by Means of Temporal Pulse Shaping." In: *New J. Phys.* 20.2 (Feb. 2018), p. 023020. DOI: [10.1088/1367-2630/aaa37c](https://doi.org/10.1088/1367-2630/aaa37c).
- [148] C. Zener and R. H. Fowler. "Non-Adiabatic Crossing of Energy Levels." In: *Proceedings of the Royal Society of London. Series A, Containing Papers of a Mathematical and Physical Character* 137.833 (June 1932), pp. 696–702. DOI: [10.1098/rspa.1932.0165](https://doi.org/10.1098/rspa.1932.0165).
- [149] A. Dunning, R. Gregory, J. Bateman, N. Cooper, M. Himsworth, J. A. Jones, and T. Freegarde. "Composite Pulses for Interferometry in a Thermal Cold Atom Cloud." In: *Phys. Rev. A* 90.3 (Sept. 2014), p. 033608. DOI: [10.1103/PhysRevA.90.033608](https://doi.org/10.1103/PhysRevA.90.033608).
- [150] S. Wimperis. "Broadband, Narrowband, and Passband Composite Pulses for Use in Advanced NMR Experiments." In: *Journal of Magnetic Resonance, Series A* 109.2 (Aug. 1994), pp. 221–231. DOI: [10.1006/jmra.1994.1159](https://doi.org/10.1006/jmra.1994.1159).
- [151] C. A. Ryan, J. S. Hodges, and D. G. Cory. "Robust Decoupling Techniques to Extend Quantum Coherence in Diamond." In: *Phys. Rev. Lett.* 105.20 (Nov. 2010), p. 200402. DOI: [10.1103/PhysRevLett.105.200402](https://doi.org/10.1103/PhysRevLett.105.200402).
- [152] B. Meyer-Hoppe, F. Anders, P. Feldmann, L. Santos, and C. Klempt. *Excited-State Phase Diagram of a Ferromagnetic Quantum Gas*. Mar. 2023. DOI: [10.48550/arXiv.2301.10655](https://doi.org/10.48550/arXiv.2301.10655).
- [153] R. Mathew and E. Tiesinga. "Phase-Space Mixing in Dynamically Unstable, Integrable Few-Mode Quantum Systems." In: *Phys. Rev. A* 96.1 (July 2017), p. 013604. DOI: [10.1103/PhysRevA.96.013604](https://doi.org/10.1103/PhysRevA.96.013604).
- [154] P. Kunkel, M. Prüfer, S. Lannig, R. Rosa-Medina, A. Bonnin, M. Gärtner, H. Strobel, and M. K. Oberthaler. "Simultaneous Readout of Noncommuting Collective Spin Observables beyond the Standard Quantum Limit." In: *Phys. Rev. Lett.* 123.6 (Aug. 2019), p. 063603. DOI: [10.1103/PhysRevLett.123.063603](https://doi.org/10.1103/PhysRevLett.123.063603).
- [155] P. Cejnar, M. Macek, S. Heinze, J. Jolie, and J. Dobeš. "Monodromy and Excited-State Quantum Phase Transitions in Integrable Systems: Collective Vibrations of Nuclei." In: *J. Phys. A: Math. Gen.* 39.31 (July 2006), p. L515. DOI: [10.1088/0305-4470/39/31/L01](https://doi.org/10.1088/0305-4470/39/31/L01).

BIBLIOGRAPHY

- [156] P. Kunkel, M. Prüfer, H. Strobel, D. Linnemann, A. Frölian, T. Gasenzer, M. Gärttner, and M. K. Oberthaler. “Spatially Distributed Multipartite Entanglement Enables EPR Steering of Atomic Clouds.” In: *Science* 360.6387 (Apr. 2018), pp. 413–416. DOI: [10.1126/science.aao2254](https://doi.org/10.1126/science.aao2254).
- [157] M. Fadel, T. Zibold, B. Décamps, and P. Treutlein. “Spatial Entanglement Patterns and Einstein-Podolsky-Rosen Steering in Bose-Einstein Condensates.” In: *Science* 360.6387 (Apr. 2018), pp. 409–413. DOI: [10.1126/science.aao1850](https://doi.org/10.1126/science.aao1850).
- [158] J. Peise, I. Kruse, K. Lange, B. Lücke, L. Pezzè, J. Arlt, W. Ertmer, K. Hammerer, L. Santos, A. Smerzi, and C. Klempt. “Satisfying the Einstein–Podolsky–Rosen Criterion with Massive Particles.” In: *Nat Commun* 6.1 (Nov. 2015), p. 8984. DOI: [10.1038/ncomms9984](https://doi.org/10.1038/ncomms9984).
- [159] P. Colciaghi, Y. Li, P. Treutlein, and T. Zibold. “Einstein-Podolsky-Rosen Experiment with Two Bose-Einstein Condensates.” In: *Phys. Rev. X* 13.2 (May 2023), p. 021031. DOI: [10.1103/PhysRevX.13.021031](https://doi.org/10.1103/PhysRevX.13.021031).
- [160] R. Schmied, J.-D. Bancal, B. Allard, M. Fadel, V. Scarani, P. Treutlein, and N. Sangouard. “Bell Correlations in a Bose-Einstein Condensate.” In: *Science* 352.6284 (Apr. 2016), pp. 441–444. DOI: [10.1126/science.aad8665](https://doi.org/10.1126/science.aad8665).
- [161] M. Fadel. *Many-Particle Entanglement, Einstein-Podolsky-Rosen Steering and Bell Correlations in Bose-Einstein Condensates*. Quantum Science and Technology. 2021. ISBN: 978-3-030-85471-3 978-3-030-85472-0. DOI: [10.1007/978-3-030-85472-0](https://doi.org/10.1007/978-3-030-85472-0).
- [162] S. S. Szigeti, O. Hosten, and S. A. Haine. “Improving Cold-Atom Sensors with Quantum Entanglement: Prospects and Challenges.” In: *Appl. Phys. Lett.* 118.14 (Apr. 2021), p. 140501. DOI: [10.1063/5.0050235](https://doi.org/10.1063/5.0050235).
- [163] C. Gross, H. Strobel, E. Nicklas, T. Zibold, N. Bar-Gill, G. Kurizki, and M. K. Oberthaler. “Atomic Homodyne Detection of Continuous-Variable Entangled Twin-Atom States.” In: *Nature* 480.7376 (Dec. 2011), pp. 219–223. DOI: [10.1038/nature10654](https://doi.org/10.1038/nature10654).
- [164] C. Hamley. “Spin-Nematic Squeezing in a Spin-1 Bose-Einstein Condensate.” PhD Thesis. Georgia Institute of Technology, 2012. URL: <http://hdl.handle.net/1853/47523>.
- [165] Y.-Q. Zou, L.-N. Wu, Q. Liu, X.-Y. Luo, S.-F. Guo, J.-H. Cao, M. K. Tey, and L. You. “Beating the Classical Precision Limit with Spin-1 Dicke States of More than 10,000 Atoms.” In: *PNAS* 115.25 (June 2018), pp. 6381–6385. DOI: [10.1073/pnas.1715105115](https://doi.org/10.1073/pnas.1715105115).
- [166] M. H. Muñoz-Arias, I. H. Deutsch, and P. M. Poggi. “Phase-Space Geometry and Optimal State Preparation in Quantum Metrology with Collective Spins.” In: *PRX Quantum* 4.2 (Apr. 2023), p. 020314. DOI: [10.1103/PRXQuantum.4.020314](https://doi.org/10.1103/PRXQuantum.4.020314).

- [167] D. J. Wineland, J. J. Bollinger, W. M. Itano, F. L. Moore, and D. J. Heinzen. “Spin Squeezing and Reduced Quantum Noise in Spectroscopy.” In: *Phys. Rev. A* 46.11 (Dec. 1992), R6797–R6800. DOI: [10.1103/PhysRevA.46.R6797](https://doi.org/10.1103/PhysRevA.46.R6797).
- [168] A. Sørensen, L.-M. Duan, J. I. Cirac, and P. Zoller. “Many-Particle Entanglement with Bose–Einstein Condensates.” In: *Nature* 409.6816 (Jan. 2001), pp. 63–66. DOI: [10.1038/35051038](https://doi.org/10.1038/35051038).
- [169] Q. Guan, G. W. Biedermann, A. Schwettmann, and R. J. Lewis-Swan. “Tailored Generation of Quantum States in an Entangled Spinor Interferometer to Overcome Detection Noise.” In: *Phys. Rev. A* 104.4 (Oct. 2021), p. 042415. DOI: [10.1103/PhysRevA.104.042415](https://doi.org/10.1103/PhysRevA.104.042415).
- [170] L. Xin, M. Barrios, J. T. Cohen, and M. S. Chapman. *Squeezed Ground States in a Spin-1 Bose-Einstein Condensate*. Feb. 2022. DOI: [10.48550/arXiv.2202.12338](https://doi.org/10.48550/arXiv.2202.12338).
- [171] L. Xin, M. Chapman, and T. Kennedy. “Fast Generation of Time-Stationary Spin-1 Squeezed States by Nonadiabatic Control.” In: *PRX Quantum* 3.1 (Feb. 2022), p. 010328. DOI: [10.1103/PRXQuantum.3.010328](https://doi.org/10.1103/PRXQuantum.3.010328).
- [172] L. Zhou, J. Kong, Z. Lan, and W. Zhang. *Dynamical Quantum Phase Transitions in a Spinor Bose-Einstein Condensate and Criticality Enhanced Quantum Sensing*. Sept. 2022. DOI: [10.48550/arXiv.2209.11415](https://doi.org/10.48550/arXiv.2209.11415).
- [173] F. Anders, L. Pezzè, A. Smerzi, and C. Klempt. “Phase Magnification by Two-Axis Countertwisting for Detection-Noise Robust Interferometry.” In: *Phys. Rev. A* 97.4 (Apr. 2018), p. 043813. DOI: [10.1103/PhysRevA.97.043813](https://doi.org/10.1103/PhysRevA.97.043813).
- [174] S. Colombo, E. Pedrozo-Peñafiel, A. F. Adiyatullin, Z. Li, E. Mendez, C. Shu, and V. Vuletić. “Time-Reversal-Based Quantum Metrology with Many-Body Entangled States.” In: *Nat. Phys.* 18.8 (Aug. 2022), pp. 925–930. DOI: [10.1038/s41567-022-01653-5](https://doi.org/10.1038/s41567-022-01653-5).
- [175] Z. Li, S. Colombo, C. Shu, G. Velez, S. Pilatowsky-Cameo, R. Schmied, S. Choi, M. Lukin, E. Pedrozo-Peñafiel, and V. Vuletić. “Improving Metrology with Quantum Scrambling.” In: *Science* 380.6652 (June 2023), pp. 1381–1384. DOI: [10.1126/science.adg9500](https://doi.org/10.1126/science.adg9500).
- [176] E. Nicklas. “A New Tool for Miscibility Control: Linear Coupling.” PhD Thesis. Universität Heidelberg, 2013. DOI: [10.11588/heidok.00015303](https://doi.org/10.11588/heidok.00015303).
- [177] M. Hetzel. “Dynamical Two-Dimensional Potentials for Ultracold Atoms.” Master’s Thesis. Leibniz Universität Hannover, 2018.
- [178] H. Albers, R. Corgier, A. Herbst, A. Rajagopalan, C. Schubert, C. Vogt, M. Woltmann, C. Lämmerzahl, S. Herrmann, E. Charron, W. Ertmer, E. M. Rasel, N. Gaaloul, and D. Schlippert. “All-Optical Matter-Wave Lens Using Time-Averaged Potentials.” In: *Commun Phys* 5.1 (Mar. 2022), pp. 1–7. DOI: [10.1038/s42005-022-00825-2](https://doi.org/10.1038/s42005-022-00825-2).

BIBLIOGRAPHY

- [179] P. Kunkel, M. Prüfer, S. Lannig, R. Strohmaier, M. Gärttner, H. Strobel, and M. K. Oberthaler. “Detecting Entanglement Structure in Continuous Many-Body Quantum Systems.” In: *Phys. Rev. Lett.* 128.2 (Jan. 2022), p. 020402. DOI: [10.1103/PhysRevLett.128.020402](https://doi.org/10.1103/PhysRevLett.128.020402).
- [180] S. Lannig. “Vector Solitons and Different Scenarios of Universal Dynamics in a Spin-1 Bose-Einstein Condensate.” PhD Thesis. Universität Heidelberg, 2022. DOI: [10.11588/heidok.00032047](https://doi.org/10.11588/heidok.00032047).
- [181] A. Farolfi, D. Trypogeorgos, G. Colzi, E. Fava, G. Lamporesi, and G. Ferrari. “Design and Characterization of a Compact Magnetic Shield for Ultracold Atomic Gas Experiments.” In: *Review of Scientific Instruments* 90.11 (Nov. 2019), p. 115114. DOI: [10.1063/1.5119915](https://doi.org/10.1063/1.5119915).

PUBLICATIONS

- **Bernd Meyer**: “Versatile, Low-Phase-Noise Microwave Source for Cold Rb-87 Experiments”. Master Thesis (2020).
- Fabian Anders, Alexander Idel, Polina Feldmann, Dmytro Bondarenko, Sina Loriani, Karsten Lange, Jan Peise, Matthias Gersemann, **Bernd Meyer-Hoppe**, Sven Abend, Naceur Gaaloul, Christian Schubert, Dennis Schlippert, Luis Santos, Ernst M. Rasel, and Carsten Klempt: “Momentum Entanglement for Atom Interferometry”. In: *Physical Review Letters* 127 (2021), p. 140402. DOI: [10.1103/PhysRevLett.127.140402](https://doi.org/10.1103/PhysRevLett.127.140402).
- **Bernd Meyer-Hoppe**, Fabian Anders, Polina Feldmann, Luis Santos, and Carsten Klempt: “Excited-state Phase Diagram of a Ferromagnetic Quantum Gas”. In: *Physical Review Letters (accepted)* (2023). DOI: [10.48550/arXiv.2301.10655](https://doi.org/10.48550/arXiv.2301.10655).
- **Bernd Meyer-Hoppe**, Maximilian Baron, Christophe Cassens, Fabian Anders, Alexander Idel, Jan Peise, and Carsten Klempt: “Dynamical Low-Noise Microwave Source for Cold-Atom Experiments”. In: *Review of Scientific Instruments* 94 (2023), p. 074705. DOI: [10.1063/5.0160367](https://doi.org/10.1063/5.0160367).

ACADEMIC CURRICULUM VITAE

PERSONAL INFORMATION

Name	Bernd Meyer-Hoppe, née Meyer
Date and place of birth	14.12.1994 Cloppenburg (Germany)

EDUCATION

2020-2023	Doctoral Studies Physics Institute of Quantum Optics and QUEST Leibniz Research School, Leibniz Universität, Hannover (Germany)
2019	Erasmus+ Study Program Physics Universidade de Lisboa, Lisbon (Portugal)
2017-2020	Master of Science Physics Leibniz Universität, Hannover (Germany)
2017-2020	Master of Education Master's Teacher Training Course for Grammar Schools Mathematics and Physics Leibniz Universität, Hannover (Germany)
2014-2017	Bachelor of Science Interdisciplinary Bachelor's Degree Programme Mathematics and Physics Leibniz Universität, Hannover (Germany)
2005-2013	Abitur Gymnasium Liebfrauenschule, Cloppenburg (Germany)

ACKNOWLEDGMENTS

Mein erster großer Dank geht an Carsten Klempt. Seine Vorlesungen haben überhaupt erst dazu beigetragen, dass ich den Master in Physik begonnen habe. Er war somit derjenige, der mich in die Welt der Quantenoptik mit Atomen geführt hat. Während meiner Promotion haben der offene Umgang miteinander und das entgegengebrachte Vertrauen eine wunderbare Arbeitsatmosphäre geschaffen, für die ich mich herzlich bedanken möchte.

Vielen Dank auch an Luis Santos, der unsere Arbeitsgruppe seit vielen Jahren unterstützt und zu meiner Freude das Korreferat übernommen hat. In den Diskussionen mit ihm habe ich immer sehr viel neues Wissen erlangen können. Ich danke außerdem Jan Arlt für die Begutachtung meiner Arbeit und Michèle Heurs für die Übernahme des Prüfungsvorsitzes.

Mit meinem ehemaligen Mitstreiter Fabian Anders habe ich in manchen Wochen mehr Zeit verbracht als mit allen anderen Menschen. Vielen Dank für diese unglaublich schöne und produktive Zeit! Danke auch für das von Beginn an entgegengebrachte Vertrauen, für die vielfältigen Diskussionen, die Erweiterung meines musikalischen Horizonts und das gemeinsame Edelbräu. Es war mir eine Freude.

Danke auch an Polina Feldmann, die sich immer wieder bereitwillig mit uns getroffen und über ESQPTs diskutiert hat, selbst trotz enormer Zeitverschiebung an die kanadische Westküste.

Christophe Cassens hat unser Labor inzwischen übernommen und ich habe keine Zweifel daran, dass er tolle Resultate erzielen wird. Danke für die gemeinsame Zeit am Experiment und das Korrekturlesen meiner Arbeit. Mögen die Schweinegeister dir und dem Experiment wohlgesonnen sein.

I would also like to thank Théo Sanchez for his contributions to our apparatus, in particular his help with the state-selective radio frequency transfer. Ein weiteres Dankeschön geht nach Dänemark an Maximilian Baron, ohne den meine Mikrowellenkette nicht so gut in das Experiment eingebunden wäre, wie sie es nun ist. Danke auch an Lion Günster, der jede noch so lästige HiWi-Aufgabe in Angriff genommen und dabei manchmal gegen Windmühlen gekämpft hat.

Vielen Dank an Mareike Hetzel und Martin Quensen von unserem Schwestereperiment QAI, bei denen ich immer wieder für „nur mal kurz eine Frage“ ins Büro gekommen bin. Insbesondere möchte ich mich bei Martin für die unzähligen Elektronikfragen entschuldigen und mich für deren ausführliche Beantwortung und die damit verbundene Hilfe bedanken.

Über das Schloss hinaus besteht die Arbeitsgruppe von Carsten Klempt aus vielen tollen und hilfsbereiten Menschen, die mich auf meinem Weg begleitet haben. Vielen Dank an alle Mitglieder unserer Arbeitsgruppe für die schöne Zeit und die tollen Gruppentreffen. Ein besonderer Dank geht an Julian Pick, Simon Haase und Janina Hamann, die mich immer wieder im HITec-Büro aufgenommen haben.

ACKNOWLEDGMENTS

Vielen Dank auch an alle Personen, die vor mir am altehrwürdigen KRB-Experiment gewerkelt haben, insbesondere an Alexander Idel und Jan Peise, mit denen ich zu Beginn meiner Zeit in der Arbeitsgruppe zusammenarbeiten durfte.

Ein großer Dank geht an das gesamte Institut für die tolle Atmosphäre. Neben Ansprechpartner*innen für so ziemlich jedes Problem bietet das IQO auch Hilfe anderer Art: Danke an Henning Albers für die Schokoquelle, an Jonas Böhm für den unzähligen Kaffee und das Balkonzimmerteam für den wunderbar neugestalteten Raum. Danke auch an Mouine Abidi für das Wiederbeleben des Pizza-Beer-Problems-Seminars.

Unser Institut würde ohne die Mitarbeitenden im Hintergrund niemals so gut funktionieren. Insbesondere geht ein lieber Dank an Birgit Ohlendorf, Madeleine Miltsch und Stephanie Kaisik, die uns planlosen Physiker*innen stets den Rücken freihalten. Danke auch an Kai-Martin Knaak, der mir in der elektronischen und mechanischen Werkstatt unzählige Dinge und den Spaß am Werkeln beigebracht hat.

Ich hatte das Glück, meine Promotion in wunderbaren Strukturen durchführen zu dürfen, insbesondere dem Sonderforschungsbereich DQ-mat und dem Exzellenzcluster QuantumFrontiers. Vielen Dank allen Beteiligten und denjenigen, die das ermöglicht haben. Für die kommenden Anträge wünsche ich viel Erfolg.

Die letzten Jahre waren unglaublich schön und äußerst intensiv. Vielen Dank an meine Freund*innen und Familie, die mich durch diese Zeit begleitet und mich hin und wieder abgelenkt haben. Auch wenn ich mich nur schwer von der Arbeit lösen konnte, habe ich die Zeit mit ihnen sehr genossen. Ich bin froh, diese wunderbaren Menschen an meiner Seite zu haben.

Mein größter Dank geht an Lisa Hoppe. Ihr müsste ich wahrscheinlich ein ganzes Kapitel widmen, bei all dem, was sie in dieser Zeit mit mir durchgestanden und erlebt hat. Die letzten Jahre waren unglaublich spannend und schön, aber auch anstengend und kräftezehrend. Jetzt haben wir beide uns etwas Ruhe verdient. Ich danke ihr von ganzem Herzen für ihre Aufmunterung, die gemeinsame Zeit und dass sie mich immer wieder antreibt. ♡

"Was steht an erster Stelle deiner Not-To-Do Liste?" rufe ich.
Das Känguru blickt hoch.
"Aufgeben", sagt es.

Marc-Uwe Kling,
Das Känguru-Manifest

